The Pennsylvania State University

The Graduate School

College of Earth and Mineral Sciences

COMPARISON OF THE TORNADIC AND NONTORNADIC SUPERCELLS INTERCEPTED BY VORTEX2 ON 10 JUNE 2010

A Thesis in

Meteorology

by

Alicia M. Klees

Submitted in Partial Fulfillment
of the Requirements
for the Degree of

Master of Science

August 2014

The thesis of Alicia M. Klees was reviewed and approved* by the following:

Yvette Richardson
Associate Professor of Meteorology
Thesis Advisor

Paul Markowski
Professor of Meteorology

Johannes Verlinde
Professor of Meteorology
Associate Head, Graduate Program in Meteorology

*Signatures are on file in the Graduate School

ABSTRACT

On the evening of 10 June 2010, VORTEX2 collected a rare set of observations of nontornadic (2345–0040 UTC) and tornadic supercells (0100–0230 UTC) evolving in close proximity to each other in northeastern Colorado. To analyze these supercells, we use single- and dual-Doppler radar, mobile mesonet, StickNet, and mobile sounding data. We strive to understand why one supercell produced no tornadoes and the other at least two, by comparing the storms' environments, outflow temperatures, storm kinematics, and interactions with other convection. Additionally, for the tornadic supercell, we study the evolution of the two tornadoes and the following periods of cyclic mesocyclogenesis.

The storms developed in environments with a low likelihood of significant tornadoes but within climatology for weak tornadoes. The only environmental parameter showing a significant difference between the two storm environments was low-level storm-relative helicity, which was larger in the environment of the tornadic supercell and may have made tornadogenesis more favorable. Virtual potential temperature deficits in the outflow were qualitatively similar for the two storms, both within the normal range for a weakly tornadic supercell. After a few hours, new convection developed along the outflow between the two storms. The nontornadic supercell experienced a merger with one of these new cells, and this merger led to the supercell's demise. Had the merger not occurred, the nontornadic supercell might have had the opportunity to produce a tornado, given the similarities in environment and outflow characteristics to the tornadic supercell. Outflow from the new convection impinged on the northern flank of the tornadic storm and may have made tornadogenesis more likely by enhancing convergence or baroclinity

in this storm. In the future, we plan to further evaluate the impacts of the merger on both supercells through model simulations using EnKF data assimilation techniques.

Additional analyses of the tornadic supercell found that the same mesocyclone produced both tornadoes, rather than cycling prior to the production of the second tornado. The subsequent cyclic mesocyclogenesis stages involved multiple cyclonic circulations that evolved in the rear flank of the storm and moved rearward aloft due to strong storm-relative winds. Meanwhile, a strong, deep, and relatively steady anticyclonic vortex also was apparent in the rear flank.

TABLE OF CONTENTS

LIST OF FIGURES

LIST OF TABLES

ACKNOWLEDGMENTS

I would first like to thank my advisor, Dr. Yvette Richardson, for all her help, support, and encouragement. She is an amazing mentor and role model to me, both personally and professionally. I am also very grateful to my committee members Drs. Paul Markowski and Johannes Verlinde for insightful discussion throughout this project, as well as great support and advice during my undergraduate years.

I thank the members of my research group, especially Jim Marquis, for their terrific help and encouragement during the past two years. I also thank my friends and family for always listening, making me laugh, and loving me, no matter how stressed I may be. I especially thank my parents, Scott, and Alyssa, and I dedicate this thesis to the four of them. Their unwavering support and love for me during my educational pursuits—and always—means the world to me.

Ultimately, I thank God for the wonderful opportunity I have been afforded to pursue my passions in graduate school. To Him be the glory!

Funding for this research was provided by the National Science Foundation through AGS-1157646.

Chapter 1

Introduction

1.1 Motivation

Tornadoes are dangerous, potentially highly destructive phenomena. The tornado outbreak of 25–28 April 2011 alone killed 321 people and caused billions of dollars in damage (NOAA 2011). Currently, forecasters can predict well hours to days in advance if such tornado outbreaks will occur. However, determining in real-time which *particular* supercell thunderstorm will generate tornadoes is a serious challenge; both nontornadic and tornadic supercells alike can have significant low-level rotation on the mesocyclone scale (e.g., Markowski et al. 2011), and the majority of supercells never produce tornadoes.

Necessary to the successful development of a tornado in a supercell is the intensification of near-surface vertical vorticity. For numerous potential reasons, this process can fail. For example, the outflow may be too cold, inhibiting crucial vorticity stretching below the updraft (Markowski et al. 2003). The low-level shear in the environment may be too weak, resulting in weak low-level updrafts that cannot sufficiently stretch the vorticity (Markowski and Richardson 2014). Consequently, tornadic supercells tend to form in environments with warmer outflows (Markowski et al. 2002) and stronger low-level shear (e.g., Markowski et al. 1998) than do nontornadic supercells.

Gaining a more thorough understanding of differences in processes occurring in and characteristics of nontornadic and tornadic supercells is crucial. Such an increased

understanding could lead to more accurate forecasting of tornadogenesis, increased warning accuracy, and a decreased number of false alarms, potentially saving lives and property.

1.2 Overview of VORTEX2

The second Verification of the Origins of Rotation in Tornadoes Experiment (VORTEX2) was designed to help understand these distinguishing characteristics and processes by collecting wind and thermodynamic observations within nontornadic and tornadic supercells (Wurman et al. 2012). The VORTEX2 armada included multiple radars to collect dual-Doppler radar observations at both the storm scale and mesoscale, and high-resolution single-Doppler radar observations at the tornado scale. In situ data were collected by mobile mesonets (Straka et al. 1996), StickNets (Weiss and Schroeder 2008), and mobile sounding units.

Given that synoptic-scale forcing can vary substantially from case to case, it can be difficult to compare tornadic and nontornadic supercells across different days. The optimal observational approach to do so, therefore, may be to examine observations of a pair of supercells, one tornadic and one nontornadic, evolving in spatial and temporal proximity to one another. The VORTEX2 armada collected one such dataset on 10 June 2010, when it deployed on two supercells in northeastern CO.

1.3 10 June 2010

On this day, an approaching upper-level shortwave trough induced lee cyclogenesis in southeastern CO. The associated strengthened southeasterly low-level flow transported moisture from the Gulf of Mexico up into northeastern CO and formed a

well-defined dryline from southeastern CO through the Texas and Oklahoma panhandles (Fig. 1.1). The synoptic-scale features on 10 June, combined with the terrain, generated an environment in northeastern CO that was favorable for the development of severe weather (Figs.1.2, 1.3). By 2230 UTC (hereafter, all times are in UTC), a pair of supercells initiated approximately 50 km apart from each other, just to the east of the foothills of the Rocky Mountains in northeastern CO (Fig. 1.4a). Both storms developed on the western edge of a moisture boundary, in a region with dewpoints in the low 50s (Fig. 1.1). An hour later, both storms had intensified and established outflows (Fig. 1.4b).

At 2340, the National Weather Service issued a tornado warning on the northern of these two supercells. VORTEX2 first intercepted this storm near Hoyt, CO, beginning at 2345. However, it became evident by 0040 that this supercell was unlikely to produce a tornado, and the decision was made to instead deploy upon the intensifying supercell to its south, which was tornado-warned at 0037. Coordinated data collection on the southern supercell occurred from 0100 to 0230. This southern storm generated two tornadoes from 0109 to 0115 and 0122 to 0126, respectively. Official reports from the Storm Prediction Center indicate that this supercell later produced two additional weak tornadoes, one at 0148 and the other at 0327, but these tornadoes were unconfirmed by the VORTEX2 armada.

This case provides rare, detailed observations of nontornadic and tornadic supercells occurring in close proximity. We examine differences in the two supercells' environments, outflow characteristics, storm kinematics, and interactions with other convective features in order to develop a hypothesis for why tornadogenesis failed in the

first supercell and succeeded twice in the second supercell. Additionally, for the second supercell, we analyze the evolution of the two tornadoes, as well as the later cyclic mesocyclogenesis, to better understand the dynamic characteristics of this tornado-producing storm.

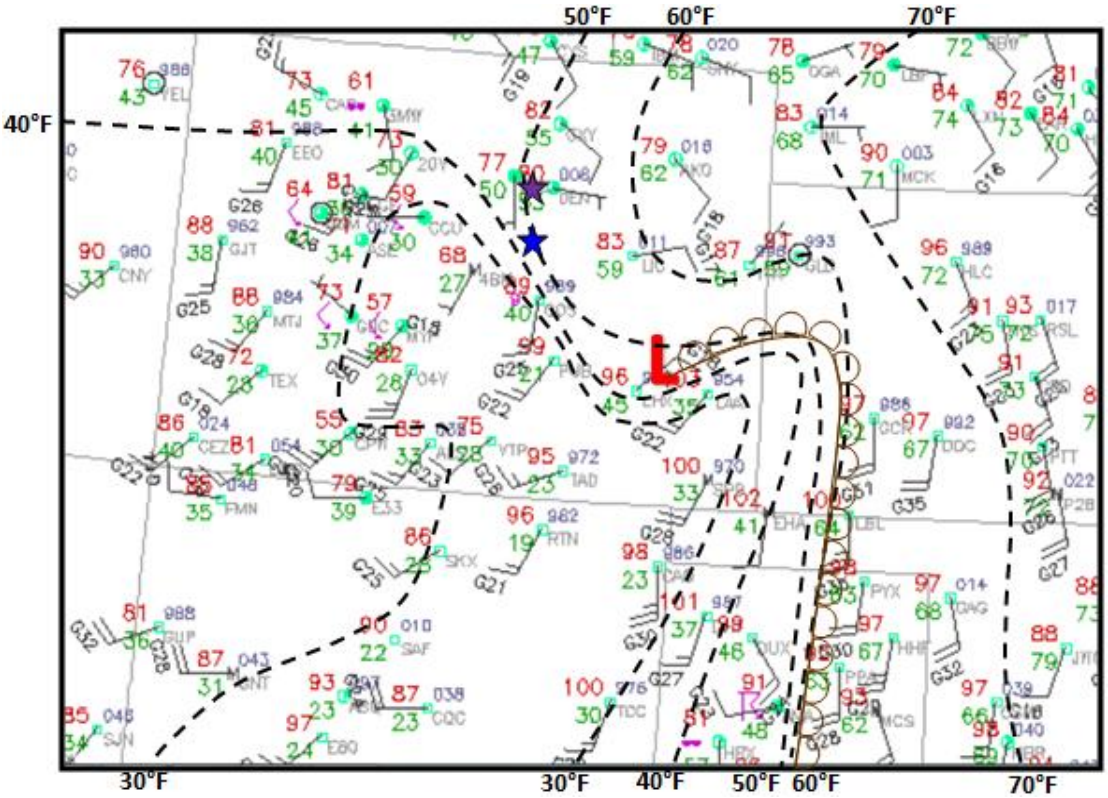

FIG. 1.1. GTS surface station plot from 2200 UTC on 10 June 2010, courtesy of NOAA. Station models show the temperature, dewpoint (both, °F), wind speed and direction, and cloud cover at particular locations. Dashed black lines are subjectively analyzed isodrosotherms. Brown scalloped line denotes the approximate location of the dryline. Stars show the location of the initiation of the nontornadic supercell (purple) and tornadic supercell (blue).

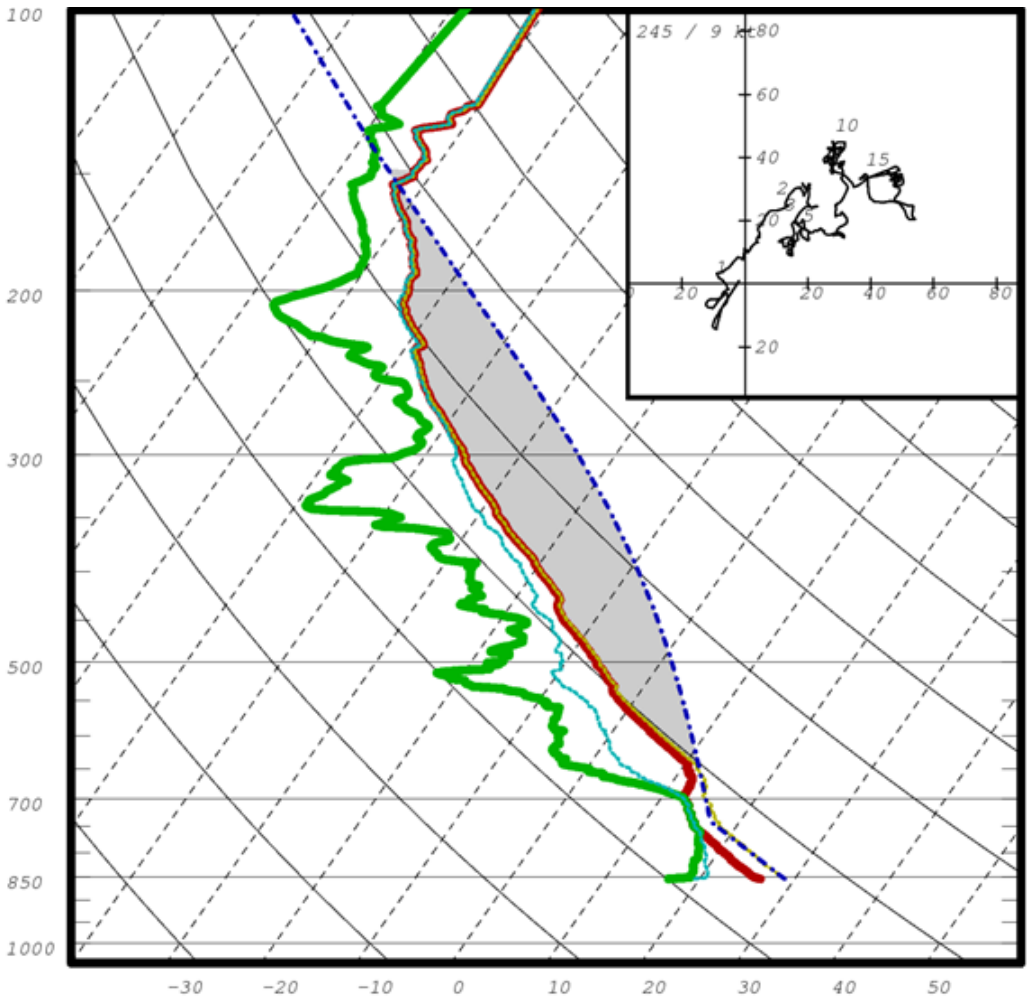

FIG. 1.2. Mobile sounding launched in the inflow of the nontornadic supercell at 2342 UTC. The red line is the temperature at each level, the green line the dewpoint, the light blue line the wet-bulb temperature, the yellow dashed line the virtual temperature, and the dark blue dashed line the lifted parcel profile. The grey shading indicates the surface-based CAPE in the sounding. The hodograph shows ground-relative winds in knots. Courtesy of NCAR.

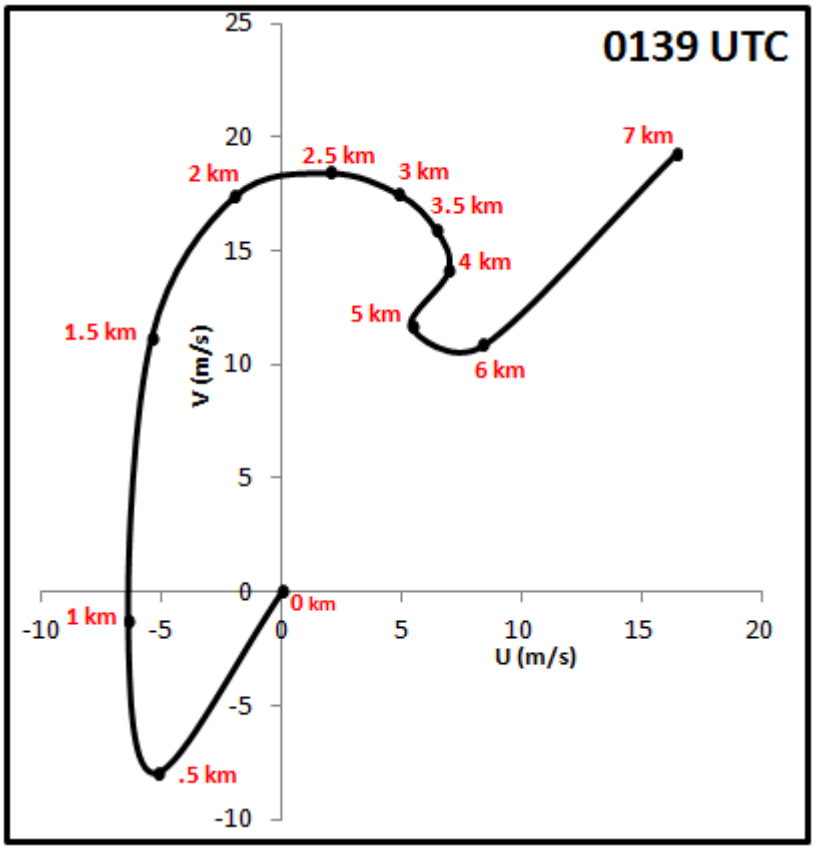

FIG. 1.3. Hodograph from the mobile sounding launched in the inflow of the tornadic supercell at 0139 UTC. Ground-relative winds are plotted in m s^{-1} every 0.5 or 1 km.

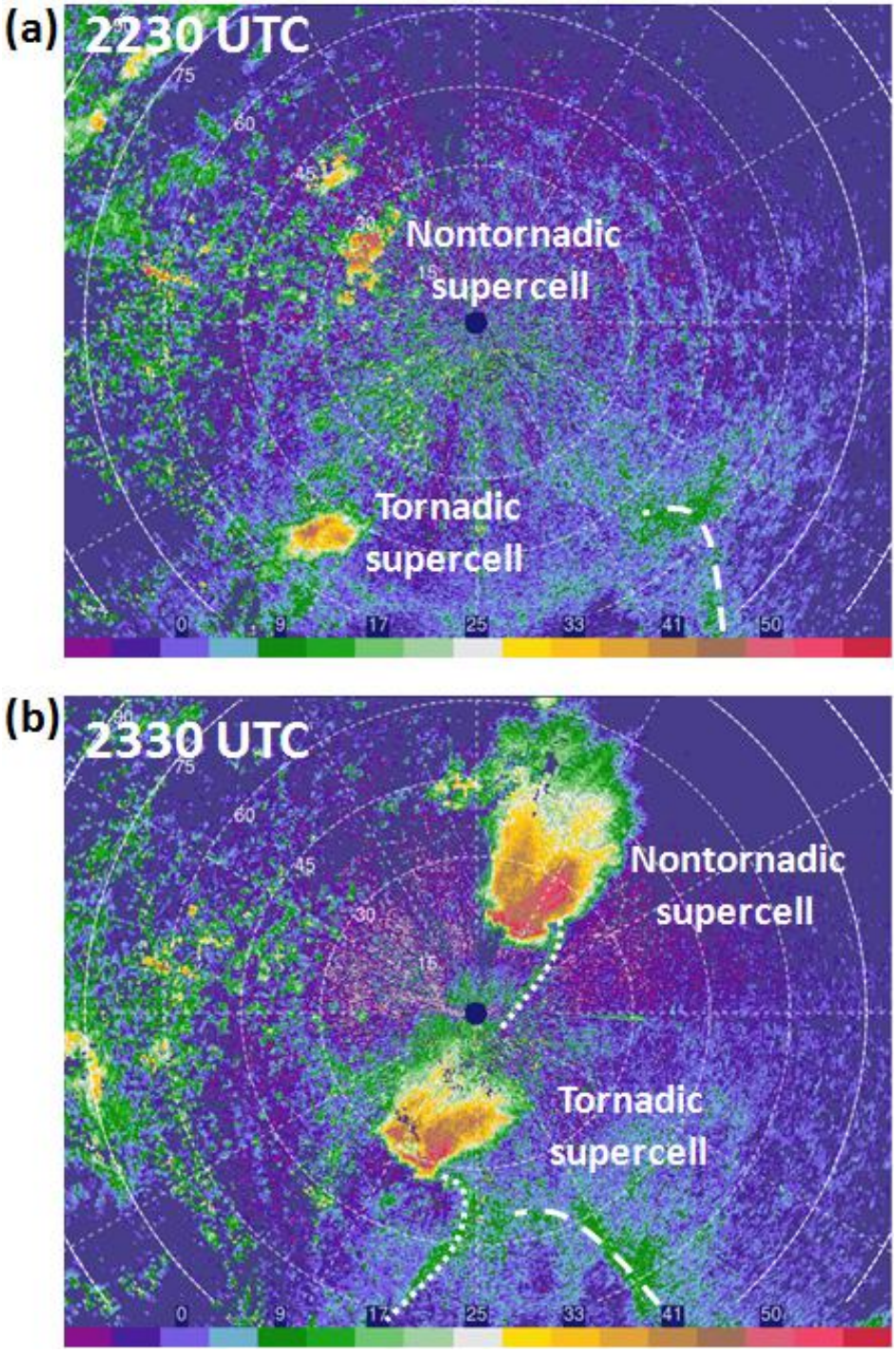

FIG. 1.4. KFTG-88D radar logarithmic equivalent reflectivity factor (dBZ) at 0.5° at (a) 2230 UTC and (b) 2330 UTC. White dotted lines in (b) denote the storms' gust fronts, based on the fine-line in the reflectivity data. White dashed line in (a) and (b) show a local (perhaps moisture) boundary.

Chapter 2

Background

2.1 Supercell structure

Supercell thunderstorms are distinct from ordinary thunderstorms due to the deep and persistent (existing for at least 20 minutes) mesocyclone present in the updraft (Doswell and Burgess 1993). A mesocyclone is a region of vertical vorticity several kilometers wide with a minimum strength of 10^{-2} s^{-1}. The mesocyclone is evident in radar radial velocity data as a couplet of inbound and outbound velocity, with the interface oriented primarily along the radial. The updraft is apparent in radar reflectivity data at midlevels as a local reflectivity minimum, known as the bounded weak echo region (BWER), owing to the lack of precipitation within the strongest part of the updraft. The downward extension of the rear side of the echo overhang capping the BWER creates the signature "hook echo" that is commonly seen in low-level radar reflectivity data of supercells (Markowski 2002).

Though the persistent and rotating updraft defines a supercell, the downdrafts also play critical roles in the overall dynamics and evolution of a supercell. A supercell contains two main downdrafts, which are located on the forward and rear flanks of the storm (Fig. 2.1). The forward-flank downdraft is generated by the cooling associated with the evaporation of rain and the melting and sublimation of ice in the precipitation zone on the forward flank of the updraft. The rear-flank downdraft develops due to the combination of (1) evaporative cooling and negative buoyancy as midlevel dry air interacts with the back of the updraft and (2) downward-directed vertical pressure

gradient forces on the upshear flank of the supercell. Increasing low-level rotation in the storm leads to a downward-directed dynamic vertical pressure gradient force that locally intensifies a region of the rear-flank downdraft, known as an 'occlusion downdraft' (Klemp and Rotunno 1983). The leading edges of the forward-flank and rear-flank outflow are defined by the forward-flank and rear-flank gust fronts, respectively.

2.2 Supercell dynamics

2.2.1 Origin of midlevel rotation

The midlevel mesocyclone initially develops owing to the tilting and stretching of horizontal vorticity associated with the mean vertical wind shear in the environment (Rotunno 1981; Davies-Jones 1984). The updraft tilts the horizontal vorticity into the vertical plane. Tilting alone creates a couplet of vorticity, with, from a perspective looking downshear, the vorticity maximum (hereafter, cyclonic vortex) on the right flank of the updraft and the vorticity minimum (anticyclonic vortex) on the left flank (Davies-Jones 1984).

However, tilting alone does not determine the final location of the vorticity couplet relative to the updraft, because advection occurs as soon as the vorticity is tilted, provided storm-relative winds are present. Thus, the location of the vorticity couplet relative to the updraft, and therefore the correlation between vertical velocity and vertical vorticity (Davies-Jones 1984), depends on the relative magnitude of the streamwise and crosswise components of the vorticity, as well as the strength of the storm-relative winds.

Streamwise (crosswise) vorticity is present when the horizontal vorticity vector is parallel (perpendicular) to the horizontal storm-relative winds, such that there is positive (zero) vorticity advection of the tilted couplet at the updraft center. If the initial

horizontal vorticity is purely crosswise, then the vortex couplet straddles the updraft and the updraft does not have net rotation (Davies-Jones 1984). On the other extreme, if this vorticity is purely streamwise, the updraft and cyclonic vortex become approximately collocated, and a cyclonic midlevel mesocyclone develops. When the horizontal vorticity has both streamwise and crosswise components, as is usually the case, there is at least some offset between the vertical vorticity and vertical velocity maxima.

The height of the base of the mesocyclone produced by such tilting appears to be linked to the strength of the low-level storm-relative helicity (Markowski and Richardson 2014). Storm-relative helicity is the vertical integral of the scalar product of the storm-relative winds and the horizontal vorticity over the lowest 1 or 3 km in the storm; in other words, a measure of streamwise vorticity (Davies-Jones 1990). High low-level storm-relative helicity suggests the development of a strong mesocyclone with a lower base. This is associated with stronger dynamical perturbation pressure gradients that enhance the strength of the updraft, allowing for increased vorticity stretching.

2.2.2 Origin of near-surface rotation

Although the development of the midlevel mesocyclone is associated with the environmental vertical wind shear, a different mechanism, baroclinically generated vorticity in the outflow, has been implicated in the development of rotation next to the surface (Klemp and Rotunno 1983; Rotunno and Klemp 1985; Davies-Jones and Brooks 1993). As it takes time for outflow to become established, near-surface rotation typically evolves later in the lifecycle of the supercell than the midlevel mesocyclone.

Downdrafts are believed to play a crucial role in the development of the near-surface mesocyclone through a combination of tilting, advection, and baroclinic

generation of vorticity. Near-surface vertical vorticity cannot be generated solely by tilting within an updraft, given that the updraft advects vertical vorticity generated via tilting away from the ground as it is produced (Fig. 2.2a–c). However, if a downdraft is also present, the downdraft simultaneously tilts horizontal vorticity and advects the resulting vertical vorticity towards the surface (Fig. 2.2d–e). In a purely barotropic process, streamwise vorticity at the starting point of the downdraft would become anticyclonic as the parcel descends and then return to a horizontal orientation at the bottom of the downdraft, given that vortex lines are constrained to follow the flow in a barotropic process. However, a combination of tilting and baroclinic vorticity generation during continued descent in the downdraft allows for separation between vortex lines and trajectories, making it possible to have positive vertical vorticity at the nadir of the downdraft trajectories (Davies-Jones and Brooks 1993).

Numerous other numerical simulations and observations have supported the hypothesized importance of the downdraft in tornadogenesis (e.g., Rotunno and Klemp 1985; Adlerman et al. 1999; Straka et al. 2007; Markowski et al. 2008). For example, the arching of vortex lines across the rear-flank downdraft in simulations (Straka et al. 2007; Markowski et al. 2008) suggests the importance of baroclinic vorticity generation in the downdraft in the production of near-ground vertical vorticity. In particular, as these vortex lines point in the direction opposite that of the environmental (barotropic) vortex lines, they indicate vortex lines of a baroclinic origin that are subsequently lifted by the updraft. Trajectory analyses done for observed supercells, as well as those in numerical simulations, suggest that some of the air feeding into the tornado first travels through the rear-flank downdraft (e.g., Brandes 1978; Wicker and Wilhelmson 1995; Xue 2004).

Additionally, in observations, tornadoes are typically seen to occur near the rear-flank downdraft and hook echo features of the supercell, in the gradient between updraft and downdraft where the two gust fronts are occluding.

An additional potential source of baroclinically generated vorticity for the near-surface rotation is within the forward-flank outflow (Klemp and Rotunno 1983; Rotunno and Klemp 1985). Given the orthogonality of the streamlines and buoyancy gradients in the forward-flank outflow, this baroclinically generated vorticity is typically streamwise. Even if it is not perfectly streamwise, the "river bend effect" as the trajectories curve around the mesocyclone tends to convert crosswise vorticity into streamwise vorticity (Adlerman et al. 1999, Davies-Jones et al. 2001, Markowski and Richardson 2014).

2.3 Tornadogenesis

2.3.1 Tornado dynamics

The near-surface vertical vorticity, baroclinically generated in the outflow and brought to the surface by downdraft, may be advected to below the updraft. If this updraft is strong, near-surface convergence beneath it may significantly contract the near-surface vorticity horizontally (i.e., the process of vortex stretching), resulting in a stronger vortex, potentially of tornado strength. Surface friction is believed to play a crucial role in this process; the presence of surface friction causes a break in cyclostrophic balance, allowing for a much stronger vortex to evolve than would otherwise be possible (Davies-Jones 2008). If surface friction was not present, cyclostrophic balance would eventually inhibit further contraction of the vortex, thus severely limiting the maximum wind speed attainable by the vortex.

While great strides have been made in the theoretical understanding of how

tornadoes develop, determining why only relatively few supercells produce tornadoes is a continuing challenge. In other words, why is low-level rotation able to contract (be stretched) to tornadic strength in some cases and not in others? Some of the answer may lie in the thermodynamic characteristics of the outflow.

2.3.2 Importance of the strength of the baroclinicity

It has been hypothesized that weaker baroclinicity (i.e., weaker temperature gradients) in the outflow favors tornadogenesis because a warmer outflow allows vortex stretching (contraction of vorticity) underneath the updraft to occur more easily (Markowski et al. 2002; Markowski et al. 2003). That outflows with weaker baroclinicity—and thus a decreased ability to generate baroclinic vorticity—would favor tornadogenesis seems counterintuitive in light of the perceived importance of baroclinic vorticity generation in the outflow in the production of near-surface vertical vorticity. Likely, there is a fine line between sufficient baroclinic vorticity generation and too much baroclinic vorticity generation, the latter of which is associated with excessive negative buoyancy, which inhibits the crucial process of vorticity stretching.

The hypothesis of warmer outflows —i.e., outflows with weaker baroclinicity—favoring tornadogenesis is rooted in the significant differences in temperature deficits measured across the RFD/FFD outflows in nontornadic and tornadic supercells (Markowski et al. 2002; Shabbott and Markowski 2006). Markowski et al. (2002) found that RFDs in "weakly" tornadic (producing EF0 or EF1 tornadoes lasting less than 5 minutes) and nontornadic supercells had maximum virtual potential temperature deficits ($|\theta_v'|$) of 4–7°C, compared to $|\theta_v'|$ of less than 2°C in significantly tornadic supercells (producing EF2 or greater tornadoes, or tornadoes of any strength lasting greater than 5

minutes) (Fig. 2.3). Markowski et al. (2002) also found equivalent potential temperature deficits ($|\theta_e'|$) in nontornadic supercells of 10–12°C, compared to $|\theta_e'|$ of less than 4°C in significantly tornadic supercells. Similarly, Shabbott and Markowski (2006) found that the FFD outflows of nontornadic supercells were more negatively buoyant than those of tornadic supercells, and $|\theta_e'|$ values were greater in FFD outflows of nontornadic supercells than those of tornadic supercells.

In both studies, tornadic supercells had weaker baroclinicity in the outflow (i.e., the RFD and FFD regions) than did nontornadic supercells. In Markowski et al. (2002), as RFD near-surface buoyancy and surface-based convective available potential energy increased and $|\theta_e'|$ and convective inhibition decreased, the likelihood, strength, and lifetime of a tornado all increased.

Weaker baroclinicity in the outflow (warmer outflows) can be attributed in part to higher low-level relative humidity, which is associated with less evaporative cooling in the outflow (Rasmussen and Blanchard 1998), assuming air in the downdraft originates in the high relative humidity layer. It is unsurprising, then, that lifting condensation levels (LCLs)— measures of low-level relative humidity—tend to be lower in the environments supportive of tornadic supercells than in environments only supportive of nontornadic supercells (Rasmussen and Blanchard 1998).

We will compare the baroclinicity in the FFD and RFD outflows of the nontornadic and tornadic supercells on 10 June 2010, to evaluate if differences in this thermodynamic characteristic are found—namely, stronger baroclinicity in the nontornadic supercell—which may have inhibited tornadogenesis in the nontornadic supercell.

2.3.3 Importance of the RFD internal surges

In addition to baroclinicity across the RFD and/or FFD as a whole, a localized kinematic and thermodynamic gradient in the RFD known as a RFD internal surge (RFDIS) may also play an important role in tornadogenesis. Lee et al. (2012) found that RFDISs in the Bowdle, South Dakota tornadic supercell seemed to impact the evolution, strength, and demise of the tornadoes. When the RFD, as modified by RFDISs, was kinematically strong and had large potential buoyancy and weak negative buoyancy, significant tornadoes were generated by the supercell. This contrasted sharply with the case of a less buoyant RFD, altered by a cooler RFDIS, during the times that tornadoes were decaying.

Additionally, Marquis et al. (2012) found that low-level convergence along a RFDIS (or, in their words, a 'secondary RFD') seemed to impact the evolution of tornadoes. Vortex line analyses for the Crowell, Texas supercell indicated that the RFDIS near the tornado tilted baroclinically generated horizontal vorticity that likely impacted the tornado's evolution. Across different cases, RFDISs were found to have varying levels of interaction with the tornado, and a RFDIS was not present in all cases.

2.4 Tornado forecasting

Even with the current understanding of storm and tornado dynamics, predicting which supercells will produce tornadoes is a continuing challenge. To address this challenge, forecasters carefully examine the synoptic and mesoscale setup to see where the environments contain an overlap of the primary precursors: strong deep-layer shear, strong low-level storm-relative helicity, sufficient CAPE, and low LCLs. Certain sounding parameters, which combine these kinematic and thermodynamic characteristics

of the environment, have been shown to discriminate between environments supportive of tornadic supercells and those only supportive of nontornadic supercells. One combination of these parameters, the Significant Tornado Parameter (STP), has particularly good skill in differentiating between nontornadic and significantly tornadic (producing tornadoes of strength EF2 or higher) environments for supercell storms (Fig. 2.4) (Thompson et al. 2002; Thompson et al. 2003; Thompson et al. 2012). The STP combines Convective Available Potential Energy (CAPE), 0–1 km storm-relative helicity (SRH1), 0–6 km vertical wind shear (6BWD), and Lifting Condensation Level (LCL), according to

$$STP = \left(\frac{ML\ CAPE}{1000\ Jkg^{-1}}\right)\left(\frac{2000-ML\ LCL}{1500\ m}\right)\left(\frac{SRH1}{100\ m^2s^{-2}}\right)\left(\frac{6BWD}{20\ m^2s^{-1}}\right).$$

The CAPE and 6BWD parameters are included in STP mainly because they help discriminate between those environments that can support supercells (to which the high majority of strong tornadoes are attributed) from those that cannot (Thompson et al. 2002), assuming a population of isolated cells rather than a continuous squall line. Typically, the supercell-supporting environment is characterized by at least moderate CAPE and at least 30–40 knots 6BWD (Rasmussen and Blanchard 1998). However, these parameters do not strongly discriminate between the environments of tornadic and nontornadic supercells, which are the focus of this research.

The two remaining parameters in the STP, LCL and SRH1, have significant discrimination ability between tornadic and nontornadic supercell environments (see 2.3.2 and 2.2.1 for physical explanations) (Thompson et al. 2003). Tornadic environments typically have lower LCLs than nontornadic environments, with significant

tornadoes typically occurring in environments characterized by LCLs below 1200 m AGL (Craven and Brooks 2004). Tornadic supercell environments also tend to be characterized by higher SRH1 (Rasmussen 2003), with environments supportive of significant tornadoes tending to have SRH1 above 200 m^2s^{-2} (Thompson et al. 2012).

We will analyze the environments of the two supercells on 10 June 2010, which evolved in close proximity to each other, for any differences that could help explain the lack of tornadoes in the first supercell; e.g., perhaps the low-level relative humidity and potential for updraft rotation were too low (high LCL and low SRH1) in the environment of the nontornadic supercell.

Having discussed supercell and tornado dynamics, important differences in the thermodynamic characteristics of tornadic and nontornadic supercells, and tornado forecasting techniques, we now examine two additional processes most relevant to the ensuing case study, cyclic mesocyclogenesis and storm interactions, that can occur in both tornadic and nontornadic supercells.

2.5 Cyclic mesocyclogenesis/tornadogenesis

Cyclic mesocyclogenesis is the process by which a new mesocyclone is generated, generally downstream (with respect to the storm-motion vector) of the original mesocyclone (Lemon and Doswell 1979; Burgess et al. 1982). Cyclic mesocyclogenesis is an important process to study; the mesocyclone often cycles prior to the production of any tornadoes subsequent to the first (Burgess et al. 1982). The general conceptual model for cyclic mesocyclogenesis as determined from numerical simulations (Adlerman et al. 1999) is as follows (Fig. 2.5).

The first steps in Fig. 2.5 have been described previously, as they lead to the

initial rotation. In particular, the supercell's rear-flank downdraft intensifies and wraps around the low-level circulation, while the updraft aloft takes on a two-celled structure. A downward dynamic vertical pressure gradient force generates an occlusion downdraft (locally intensified region of the RFD) that facilitates the rapid intensification of the mesocyclone through enhancement of convergence on its leading edge and transport of vertical vorticity to the updraft. Eventually, the occlusion downdraft and main RFD encircle the mesocyclone and sever the near-surface updraft from its inflow. This leaves the near-surface mesocyclone, and its associated updraft, in a region of rain, and both weaken from evaporative cooling and other detrimental precipitation impacts such as hydrometeor loading.

As the rear-flank gust front continues progressing eastward, the new updraft continues to intensify and eventually splits from the weakening original updraft. Near-surface mesocyclogenesis occurs with the new updraft and the gust front. This iteration of mesocyclogenesis, and any subsequent, tends to occur more efficiently than the original development of the mesocyclone, given the preferential orientation of near-surface baroclinicity (Adlerman et al. 1999). A cycle of mesocyclogenesis takes an average of 40 minutes in observed events (Burgess et al. 1982) and around an hour in model simulations (Adlerman et al. 1999).

Dowell and Bluestein (2002 a,b) used dual-Doppler observations to study cyclic tornadogenesis in the McLean, Texas tornadic supercell and discovered that new circulations developed along a bulge in the rear-flank gust front and weakened when they traveled toward the rear of the parent storm, away from the supporting lift of the main updraft. The strength of the low-level storm-relative winds in the outflow played a

crucial role in determining whether or not such vortices would make this rearward travel with respect to the storm-scale updraft and dissipate. Additionally, Dowell and Bluestein (2002a,b) hypothesized that if a supercell has weak outflow, such that the gust front does not race ahead of the updraft (aloft), cycling of the storm-scale updraft may not need to occur before the production of a new tornado, since the original updraft has not been significantly weakened. Similarly, French et al. (2008) found that storm-scale vortices travel rearward if they are not in sufficiently strong storm-relative outflow winds to maintain their position near the main updraft.

Few other observational studies have been completed on cyclic mesocyclogenesis/tornadogenesis. *The tornadic supercell on 10 June 2010 underwent multiple cycles of mesocyclogenesis during its long nontornadic phase, offering a rare opportunity to examine this process using both single- and dual-Doppler data.*

2.6 Storm interactions

Initiation of storms often occurs only along linear air mass boundaries; it is, therefore, often difficult for storms to remain isolated. At times, two storms may merge into a new storm, with important implications for the future of one or both storms. A merger between two storms is defined here to begin when the two storms no longer have separate reflectivity maxima, based on a threshold of 35 dBZ (Rogers 2012). The merging of a supercell with another storm in the environment can have varying impacts on both of the storms involved. One such observed impact is increased tornado production (Lee et al. 2006; Wurman et al. 2007).

Lee et al. (2006) found that during a tornado outbreak in central Illinois, 20 out of 37 tornadoes were generated by storms that experienced a merger event within 15

minutes prior to tornadogenesis. Wurman et al. (2007) discovered that a merger event preceded each of two tornadoes produced by a supercell near Kiefer, Oklahoma. Enhanced convergence zones resulting from the merger events may have helped stretch the pre-existing low-level vorticity.

On the other hand, a merger event can instead result in the demise of the original supercell. Based on numerical simulations, Hastings and Richardson (2014) presented the following conceptual model of such an event (Fig. 2.6). A cell approaches the inflow region of the supercell. The outflow from this cell, as it is negatively buoyant, cuts off the inflow to the updraft of the supercell. Consequently, the supercell weakens and, by one hour after the merger begins, completely dissipates. The other cell may survive the merger, intensify, and continue evolving as a classic supercell.

Few observational and numerical simulation studies have focused on supercell mergers other than the studies discussed above. *On 10 June 2010, rare observational data (mobile radar and mobile mesonet) were collected prior to and during a merger between a nontornadic supercell and a convective cell. This merger is of particular interest, given that it led to the demise of the supercell, which potentially could have otherwise produced a tornado.*

2.7 Context of this study

This study will examine the rare data collection of a tornadic and nontornadic supercell evolving in close proximity (relative to the scale of variations in the environment in which they existed) to each other. We first will compare environmental characteristics near the two storms and then examine their cold pool characteristics to provide further observational evidence to the current pool of observational studies.

Additionally, we will compare the dynamics of the two storms. We also will study a storm merger involving the nontornadic supercell and a cyclic mesocyclogenesis process in the tornadic supercell, to help fill the void of observational support for and verification of the conceptual models of these two processes. Additionally, we will analyze the evolution of the two tornadoes generated by the tornadic supercell and compare to the classic conceptual model.

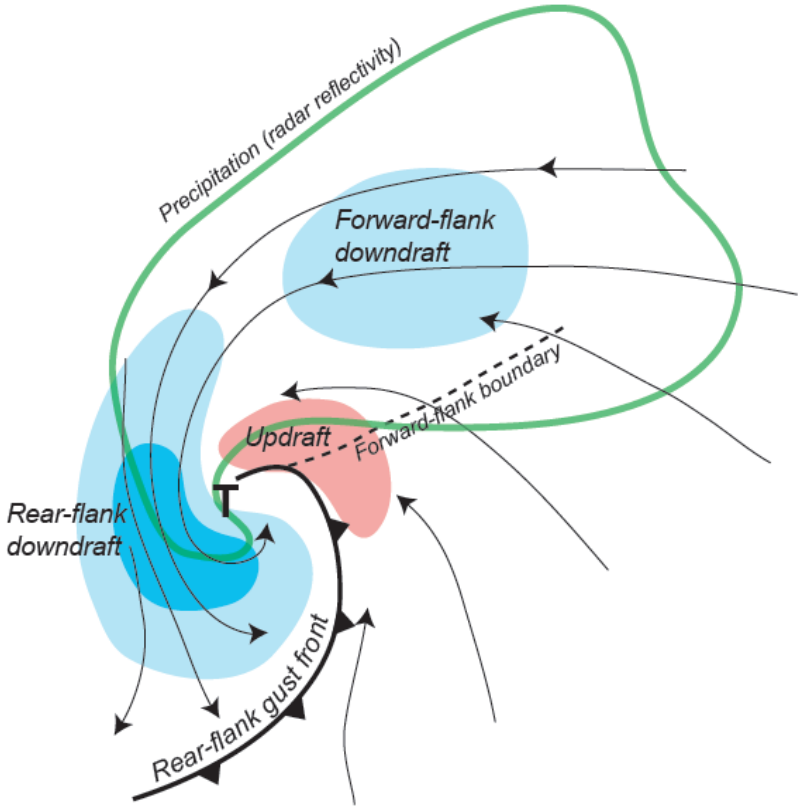

FIG. 2.1. Schematic of tornadic supercell structure. Shaded regions denote the RFD (rear-flank downdraft), UD (updraft), and FFD (forward-flank downdraft). Frontal symbols denote the gust front. Arrows are streamlines. Courtesy of Jim Marquis, modified from Lemon and Doswell (1979).

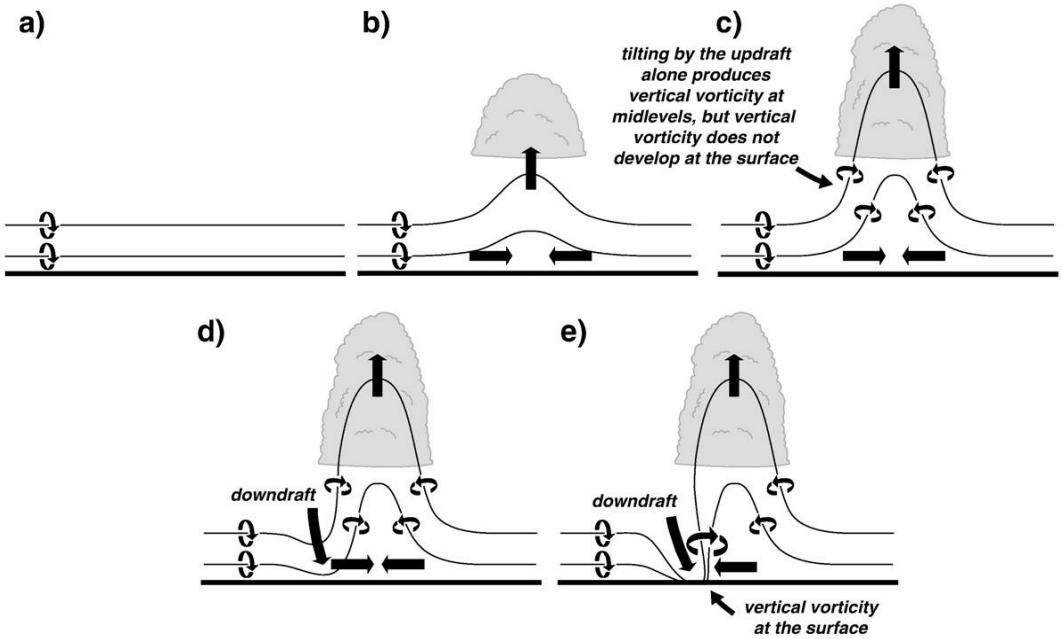

FIG. 2.2. Evolution of the vortex lines (contours) in a supercell if there is no preexisting vertical vorticity near the surface and: (a)-(c): only an updraft is present, or (d)-(e): an updraft and a downdraft are present. From Markowski and Richardson (2009).

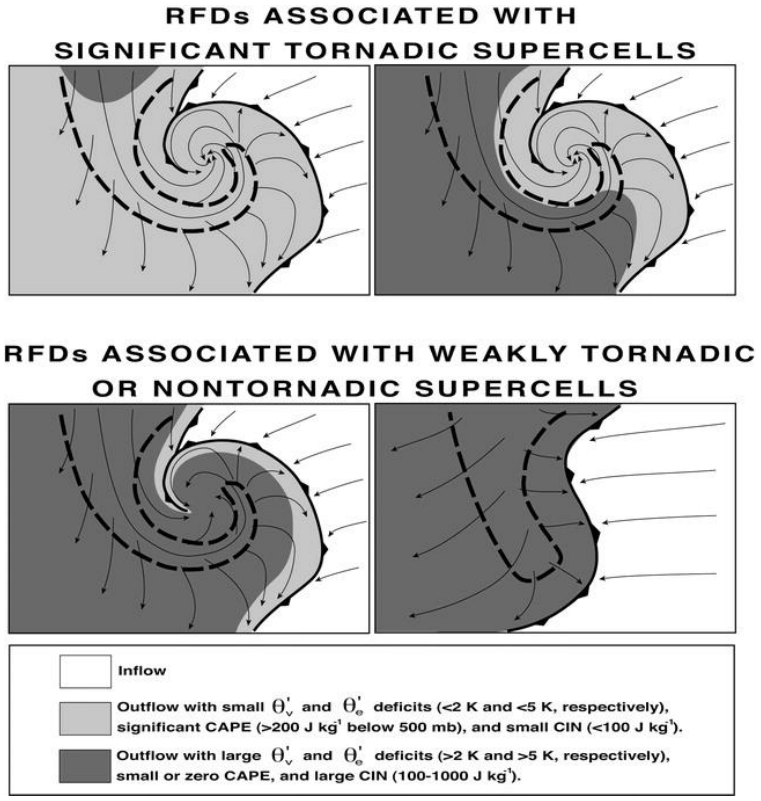

FIG. 2.3. Composite virtual potential temperature deficit magnitudes (shaded) for significantly tornadic (EF2 or stronger, or EF0 or EF1 lasting for more than 4 min) and weakly tornadic (weak, short-lived tornadoes) or nontornadic supercells. The thick dashed contour indicates the location of the hook echo, and the arrows show the streamlines. From Markowski et al. (2002).

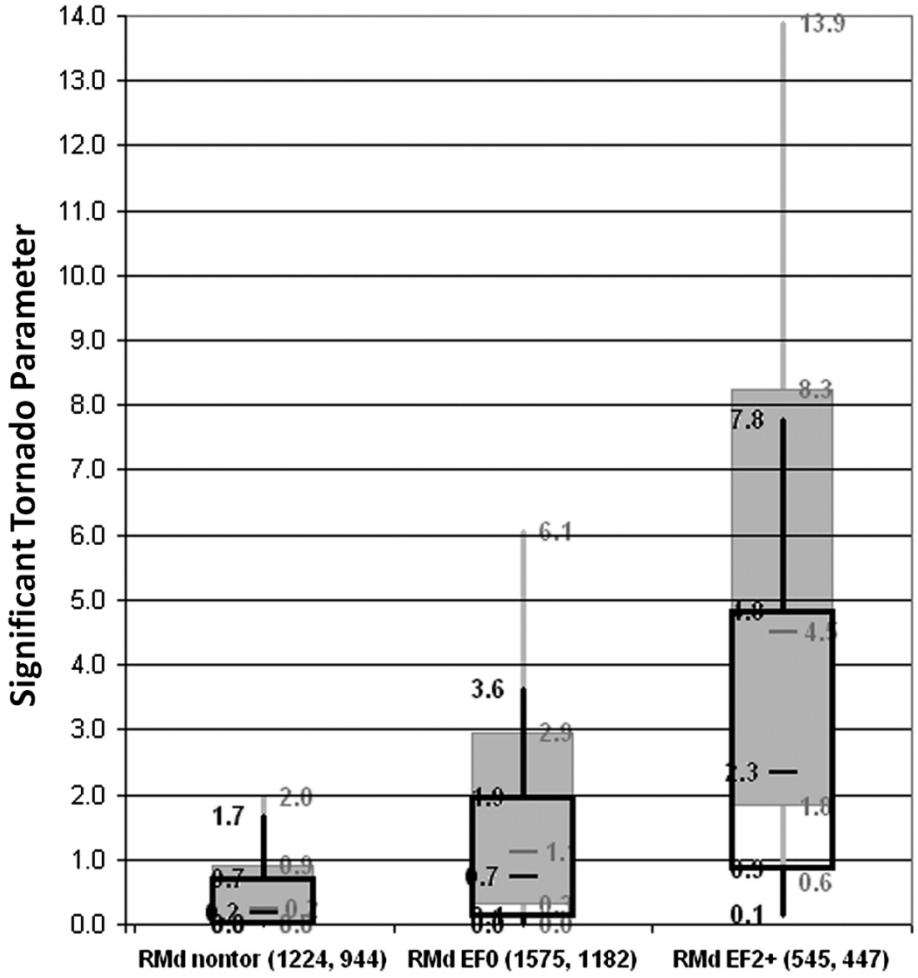

FIG. 2.4. Box and whisker plots of climatology of nontornadic ('RMd nontor'), weakly tornadic ('RMd EF0'), and significantly tornadic ('RMd EF2') storm environments represented by STP. Gray shaded boxes correspond to fixed-layer STP, and non-shaded boxes, effective-layer STP. Numbers are of the various quartiles of the climatological parameter data. From Thompson et al. 2012.

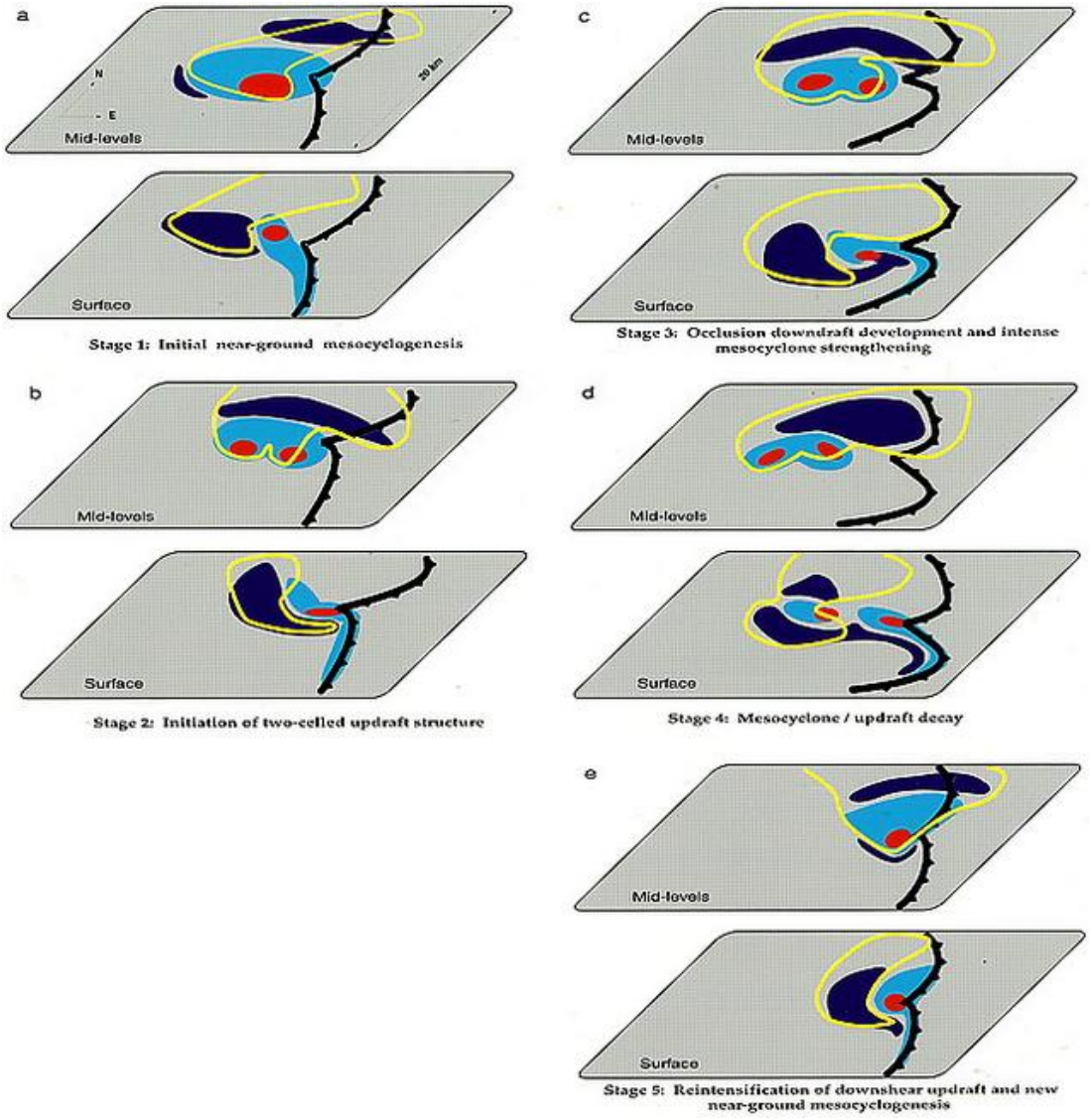

FIG. 2.5. Schematic diagram of the five-part conceptual model for a single occlusion cycle. Boundary of the cold pool at the surface is indicated by the black scalloped line. Areas of vorticity maxima are shaded in red, updrafts in light blue, and downdrafts in dark blue. Yellow contours show the boundary of the region of rain. From Adlerman et al. (1999).

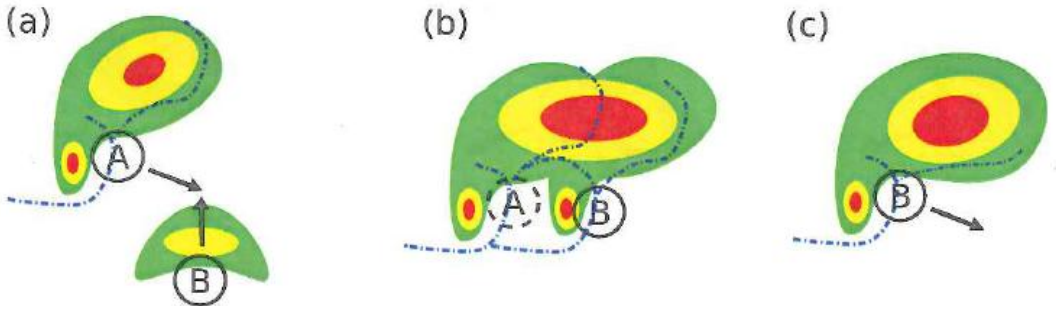

FIG. 2.6. Conceptual model of a merger between a supercell and another cell that eventually destroys the supercell. Circled 'A' indicates the updraft of the original supercell, and circled 'B' that of the approaching cell. Dashed blue lines indicate the gust fronts of each of the storms. From Hastings and Richardson (2014).

Chapter 3

Methods

3.1 General data summary

The VORTEX2 armada collected an extensive data set on 10 June 2010. For this case study, the focus will be on the two dual-Doppler deployments (one on each storm) of the SMART-Radars (SR1 and SR2), a multi-Doppler period adding NOXP to the SMART-Radars during the second storm, the single-Doppler observations of DOW7 for the second storm during the two tornadoes, and the mobile mesonet, StickNet, and sounding data during both storms (Figs. 3.1 and 3.2).

3.2 Radar data

3.2.1 Editing techniques

Radar data used in this study were collected by the SR1, SR2, NOXP, and DOW7 radars (Table 3.1). Radar data were edited using the National Center for Atmospheric Research (NCAR) Solo II radar data editing and visualization software (Oye et al. 1995). As standard procedure, ground clutter and noisy velocity data (the latter typically found in low-reflectivity regions) were removed. Generally, noisy velocity data were filtered for DOW7 data by threshholding on Normalized Coherent Power (NCP) of 0.3 and, for SR1, SR2, and NOXP data, by threshholding on a combination of Spectrum Width (SW) of 8 m s^{-1} and Returned Power (DM) of -85 dBM. Other noisy data were removed as needed.

In the raw SR1 data, there was strong evidence of an elevation angle error. High reflectivity associated with ground clutter was virtually unchanged over several

subsequent low-level scans, suggesting that the radar beam was pointing into/very close to the ground over these reported elevations (up to 1.6°). Additionally, we identified a specific reflectivity feature with a limited vertical extent that was not found at the same heights in the SR1 and SR2 data (Fig. 3.3). To fix the evident elevation angle error, we adjusted the elevation angles by -1.5°, the offset identified in SR1 data collected during the DYNAMO project, which occurred after VORTEX2 (Schumacher 2013, personal communication). After this correction, the heights of our chosen reflectivity feature matched those indicated by SR2 (Fig. 3.3). (The two are not an exact match because the scans from the two radars do not intersect exactly at the height of the feature.)

Additionally, SR1 and SR2 data had suspiciously high outbound velocities to the east of the mesocyclone at midlevels, as well as a suspicious radial divergence line along the rear flank of the storm. As both of these regions had low reflectivity and/or were near a strong reflectivity gradient, it is likely these returns were from side lobes rather than the main beam of the radar and were, therefore, appearing at the wrong elevation. Consequently, these features were removed.

3.2.2 Gridding techniques

Edited radar data were objectively analyzed to a Cartesian grid using the two-pass Barnes successive corrections method (Barnes 1964; Koch et al. 1983; Majcen et al. 2008). An isotropic Barnes weighting function was used within this method to retain scales appropriate for the data spacing (δ), approximated as $\delta = r\theta$, where r is the radial distance from the radar and θ is the beamwidth (Fig. 3.4). For the first pass, the smoothing parameter, κ, was set to $(1.33d)^2$, as recommended by Pauley and Wu (1990), where d is the largest value of δ within the analysis domain (Trapp and Doswell 2000).

For the second pass, κ was set to $0.3(1.33d)^2$ (Majcen et al. 2008). The cut-off radius used in gridding the data was $R_c = 3d$. No extrapolation was permitted in the gridding process.

The spacing of the Cartesian grid was set to $\Delta x = \Delta y = \Delta z \approx \frac{d}{3}$, per Koch et al. (1983). The altitude of the grid origin was approximately the average elevation of the ground passed over by the midlevel mesocyclone during each deployment. The horizontal grid origin was set to the location of the midlevel (2.25 km and 1.75 km for the first and second storms, respectively) mesocyclone at each time, as to minimize the movement of the storm relative to the grid. The mesocyclone was assumed to move at constant average velocity, which was calculated using KFTG WSR-88D data. The average mesocyclone velocity was also used to correct the position of data to a common reference time for each volume. This correction helped prevent the artificial tilt with height of features in the storm due to the temporal offset between data at the beginning of the volume and data at the end.

3.2.3 Dual-Doppler synthesis techniques

The three-dimensional wind field was synthesized from the radar data by applying an upward integration of the anelastic mass continuity equation, assuming vertical velocity (*w)* of zero at the surface. In this process, first, estimates of *u* and *v*, the two horizontal components of the wind, were obtained from the two radial velocities measured by the radars. Then, the upward integration was completed to estimate *w*. Iterative adjustments (Brandes 1977; Dowell and Shapiro 2003) were made to all three wind fields (*u, v,* and *w*) until $\Delta(\bar{\rho}w) < 0.01$ kg m^{-2} s^{-1} ($\bar{\rho}(z)$ being a particular

height's reference density) between iterations, i.e., until the solution converged. Then, the aforementioned process was repeated at each subsequent level. Although extrapolation is not allowed in the gridding stage, we did allow downward extrapolation of the *u* and *v* estimates to facilitate integration of mass continuity. After the final *u, v,* and *w* were obtained at all levels, winds were removed from the extrapolated levels so they were not used in analyses.

3.2.4 Dual-Doppler syntheses on 10 June 2010

For the first storm, a dual-Doppler synthesis was completed with SR1 (25 km to south of mesocyclone, 0006–0036 UTC) and SR2 (30 km to the southeast of the mesocyclone, 0006–0036 UTC) data (Table 3.2). For the second storm, a dual-Doppler synthesis was completed using SR1 (30 km to the west of the mesocyclone, 0200–0235 UTC) and SR2 (25 km to the southwest of the mesocyclone, 0200–0235 UTC) data (Table 3.2). For both SR1-SR2 dual-Doppler deployments, three-minute volumes over elevation angles 0.6°–14° were used. Specific elevation angles sometimes differed volume to volume, but generally included 0.8°, 2.0°, 2.8°, 3.8°, 4.8°, 5.7°, 6.6°, 7.6°, 9.3°, 11.5°, 13.4° (SR1) and 0.6°, 1.3°, 2.0°, 2.7°, 3.4°, 4.1°, 4.9°, 5.7°, 6.5°, 7.3°, 8.1°, 9.3°, 10.5°, 12.2° (SR2). A multi-Doppler synthesis, which also included NOXP (15 km to the south of the mesocyclone, 0200–0235 UTC) data, was completed for the second storm (Table 3.2). For the multi-Doppler synthesis, 90-second volumes of NOXP data over elevation angles of 1°–7° (in increments of 1°) were used.

3.3 Sounding data

3.3.1 Data overview

On 10 June 2010, four mobile GPS Advanced Upper-Air Sounding (MGAUS) systems were used by NSSL and NCAR teams to launch twenty-one radiosondes in northeastern CO, measuring pressure, temperature, relative humidity and wind velocity every second. Relative humidity and temperature data were used to calculate the dewpoint. The geopotential height was determined from the hydrostatic equation and, due to accuracy issues with GPS altitude measurements, was used for determining the altitude. Data were subject to rigorous quality control completed by scientists at NCAR's Earth Observing Laboratory (NCAR 2010).

Six radiosondes were launched prior to the storm to measure the existing environmental variability. Once the target storms were identified and the VORTEX2 armada deployed, fifteen mesoscale radiosondes were launched in groups of three to four at around 2354 UTC, 0045 UTC, 0140 UTC, and 0230 UTC. Within each group, one sounding was launched upshear of the target storm, and two to three soundings downshear of the target storm.

The radiosonde data were used to help characterize the thermodynamic and dynamic environments in which the supercells evolved. For each sounding, numerous thermodynamic and dynamic parameters, as well as composite indices, were calculated and analyzed, with focus on the soundings with the greatest spatial and temporal proximity to each of the storms.

3.3.2 Storm environment parameters and indices

The thermodynamic parameters of CAPE, CIN, LCL, etc. were calculated for each radiosonde sounding using the NSHARP program in GEMPAK. NSHARP uses the virtual temperature correction and defines the mixed-layer to be over a depth of 100 mb.

The 0–1 km storm-relative helicity (Davies-Jones 1990) was calculated using

$$SRH1 = \sum_{n=1}^{N-1}\left[(u_{n+1} - c_x)(v_n - c_y) - (u_n - c_x)(v_{n+1} - c_y)\right], \quad (1)$$

where c_x and c_y are the horizontal components of the estimated storm motion, u_n and v_n the horizontal components of the environmental winds at a specific level *n*, and N the total number of levels of winds between 0 and 1 km (Markowski and Richardson 2010).

The significant tornado parameter (STP) was calculated using the *fixed-layer* formulation (Thompson et al. 2002; Thompson et al. 2003),

$$STP = \left(\frac{MLCAPE}{1000\ Jkg^{-1}}\right)\left(\frac{2000-MLLCL}{1500\ m}\right)\left(\frac{SRH1}{100\ m^2s^{-2}}\right)\left(\frac{6BWD}{20\ m^2s^{-1}}\right), \quad (2)$$

where *MLCAPE* and *MLLCL* are CAPE and LCL, respectively, calculated using a parcel having properties averaged over the lowest 100 mb of a sounding; SRH1 is the 0-1 km storm-relative helicity; 6BWD is the 0–6 km vertical wind shear.

Fixed-layer STP was used instead of the more current effective-layer STP formulation. The latter has better discrimination ability (Thompson et al. 2012), but effective-layer STP could not be calculated for all soundings on 10 June 2010; some soundings were disabled prior to reaching the equilibrium level.

3.4 Mobile mesonet data

3.4.1 Data overview

On 10 June 2010, six Penn State-NSSL mobile mesonet vehicles with mounted instruments (Straka et al. 1996; Waugh and Fredrickson 2010) were deployed on both supercells. The first supercell was sampled from 2345–0040 UTC, with excellent spatial data coverage. The second supercell was sampled from 0110–0230 UTC. Extensive data collection during the two tornadoes was hindered by the lack of a good road network and the inability to redeploy crews in time, especially during the first tornado. Data sampling improved following the second tornado.

The mobile mesonet instrumentation collected GPS position, temperature, relative humidity, pressure, and wind velocity data every second. Because the "U-tube" temperature shield design was used, data collected from stationary mobile mesonet vehicles were retained. This was done in contrast to prior mobile mesonet deployments that used a "J-tube" design, because the "U-tube" shield allowed for better aspiration of the instruments than the "J-tube" shield (Waugh and Fredrickson 2010). For details on specifics of the mobile mesonet instruments, potential errors, and quality control procedures, please refer to Straka et al. (1996), Markowski et al. (2002), and Waugh and Fredrickson (2010).

3.4.2 Data processing

Two passes of a triangular weighting filter (with a ten-second filter radius) were applied to the mobile mesonet data to remove high-frequency noise, in effect smoothing the data. Six minutes of mobile mesonet data were used (i.e., the storm was assumed to maintain a steady-state over a six-minute period), with a time-to-space conversion done

to produce analyses valid at a given reference time as in Markowski et al. (2002), Shabbott and Markowski (2006), and Markowski et al. (2012).

For each analysis, virtual potential temperature and equivalent potential temperature were calculated and used to evaluate the thermodynamic fields within and near the supercells. Virtual potential temperature, θ_v, was calculated using

$$\theta_v = \theta(1 + 0.61r)\,, \tag{3}$$

where r is the water vapor mixing ratio, and θ the potential temperature. Note that the mobile mesonet instrumentation measured a 'fast-response' temperature and a 'slow-response' temperature, depending on the response time of the particular sensor making the measurement. The 'slow-response' temperature was measured by the temperature and relative humidity sensor that was protected by a membrane to keep the relative humidity probe clean from pollutants. This 'slow-response' temperature was used when converting relative humidity into other moisture variables such as *r*, and the 'fast-response' temperature was used in the calculation of θ.

Equivalent potential temperature, θ_e , was calculated using Bolton's formula (Bolton 1980),

$$\theta_e = Tp^{0.2854(1-0.28r)} exp^{r(1+0.81r)\left(\left(\frac{3376}{T^*}\right)-2.54\right)}, \tag{4}$$

$$\text{where} \quad T^* = 55 + \left(\frac{2840}{3.5log(T)-log(e)-4.805}\right) \tag{5}$$

and *T** is the temperature at the lifting condensation level, *p* is pressure, *T* is surface temperature, *r* is mixing ratio, and *e* is vapor pressure.

To estimate the potential path of parcels on a Skew-T (from which relevant quantities were calculated), a given temperature and dewpoint observation collected by

the mobile mesonet was used as a surface parcel in the inflow sounding, i.e., it became the lowest observation in the sounding, with all sounding observations collected at elevations below disregarded and all sounding observations above the mobile mesonet observation level left unchanged. Surface-based CAPE, CIN, LCL, etc. were then calculated.

3.5 StickNet data

StickNets are instruments mounted on tripods that are anchored into the ground (Weiss and Schroeder 2008). StickNets are deployed ahead of the storm in a network that is designed to optimally capture storm-scale baroclinicity as the storm passes over. Observations collected by StickNets include temperature, relative humidity, wind speed and direction, and pressure.

A spatially extensive StickNet dataset was collected during the second storm. From 0142–0154 UTC, seventeen StickNets captured data as the storm passed over. Only fifteen StickNets were used in analyses, since two platforms collected temperature and relative humidity data with suspiciously low values (when compared against values from nearby StickNets over the same time period).

Each StickNet analysis was made using six minutes of data. Refer to 3.4.2 for the data processing techniques used.

Radar	Type	Beamwidth (°)	Wavelength (cm)	Temporal resolution (sec)
SR1	C-band	1.5	5	180
SR2	C-band	1.5	5	180
DOW7	X-band	1.0	3	45
NOXP	X-band	0.9	3	90

TABLE 3.1. Radar specifications. Temporal resolution is specific to 10 June 2010.

Storm	Radars	Time Range (UTC)	Base-line (km)	Δx, Δz (km)	Grid Altitude (km)	κ (km^2)	d (km)	Storm Motion (u,v; m/s)
Nontornadic	SR1-SR2	0006-0036	33	.5	1.469	2.98	.3	9.68, 0.58
Tornadic	SR1-SR2	0200-0230	20	.5	1.478	2.98	.3	10.46, 4.94
Tornadic	SR1-SR2-NOXP	0200-0230	---------	.5	1.478	2.98	.3	10.46, 4.94

TABLE 3.2. Parameters used in dual- and multi-Doppler syntheses.

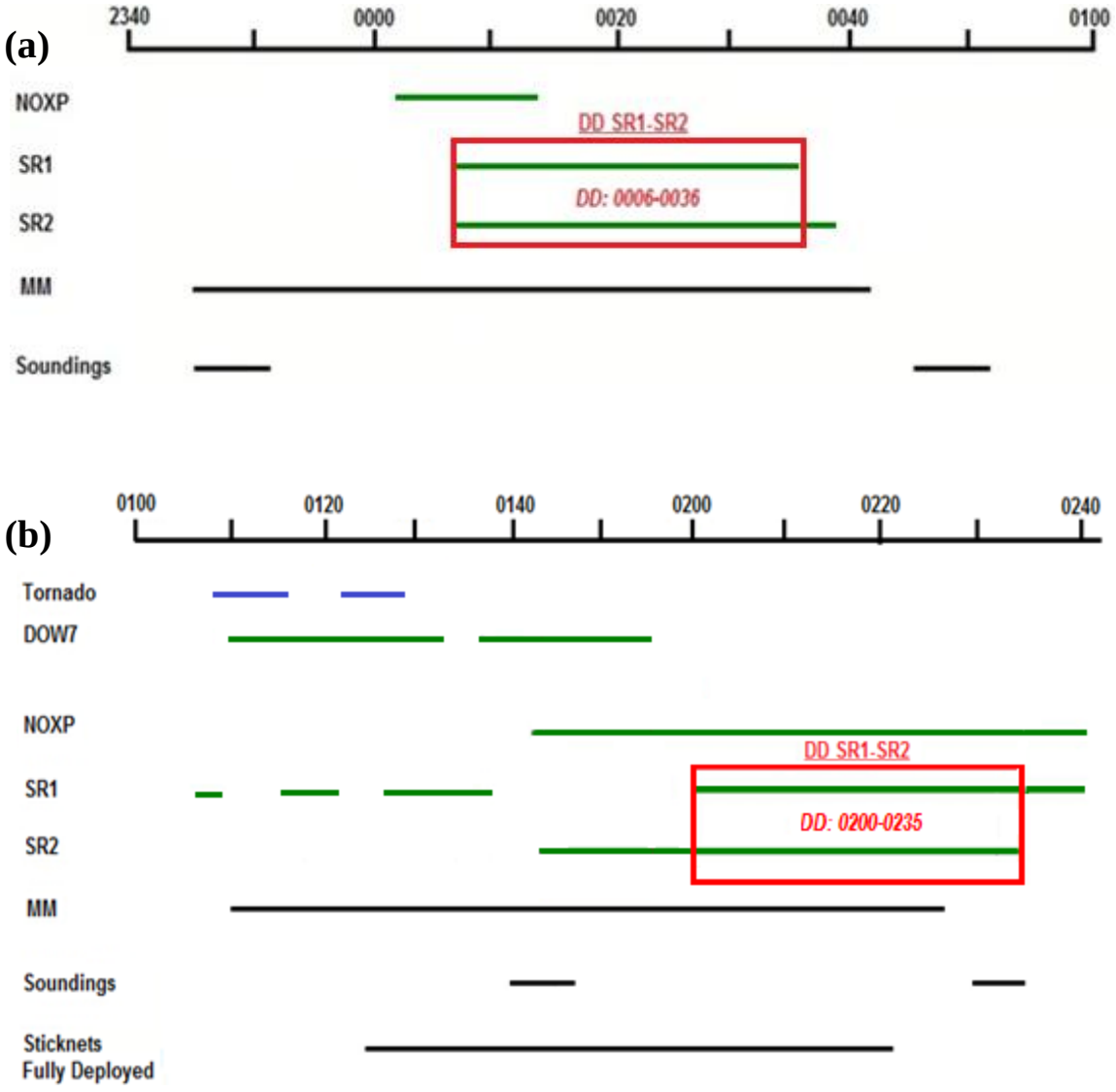

FIG. 3.1. Timeline of data used in this study collected on 10 June 2010 by the VORTEX2 armada on the (a) nontornadic supercell and (b) tornadic supercell.

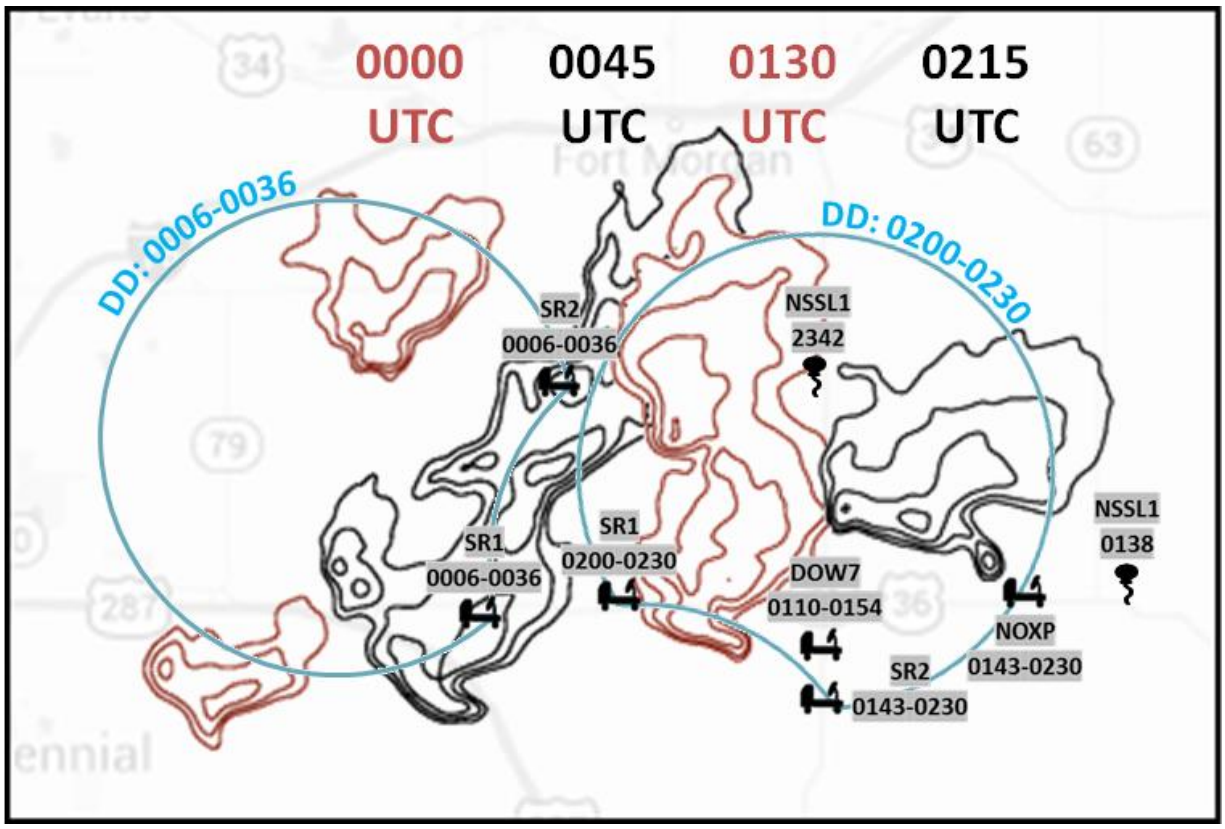

FIG. 3.2. Deployment map for 10 June 2010. Reflectivity contours are shown every 45 minutes for the nontornadic (northern) and tornadic (southern) supercells. Radar truck icons show the location of each mobile radar deployment, with time ranges (UTC) in grey boxes. Balloons denote the location of example mobile sounding launches, with launch time (UTC) in grey boxes. Blue lobes represent the dual-Doppler lobes, regions in which 3-D wind fields of the storms can be obtained, with dual-Doppler time periods in light blue text. VORTEX2 deployed on the nontornadic supercell first (0006–0036 UTC) and then the tornadic supercell (0110–0230 UTC).

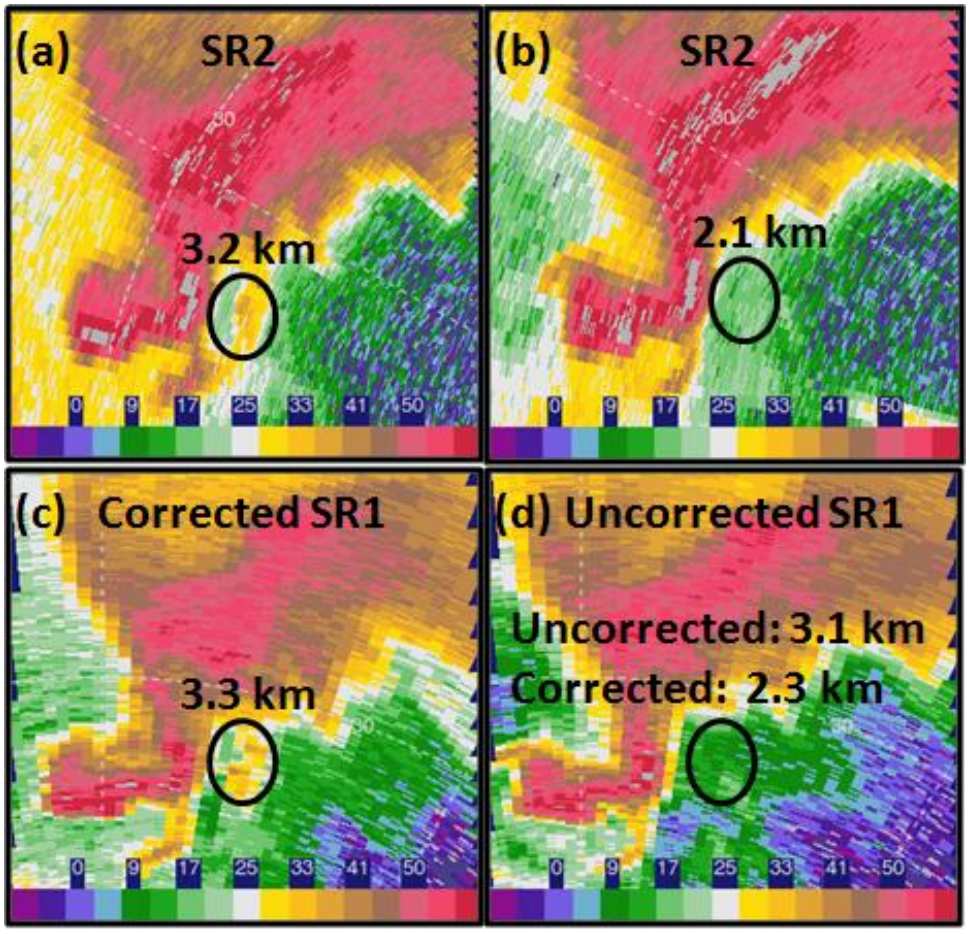

FIG. 3.3. Reflectivity feature (or lack thereof), circled, as captured by (a) SR2 at 3.2 km (b) SR2 at 2.1 km (c) corrected SR1 at 3.3 km (d) uncorrected SR1 at (uncorrected) 3.1 km

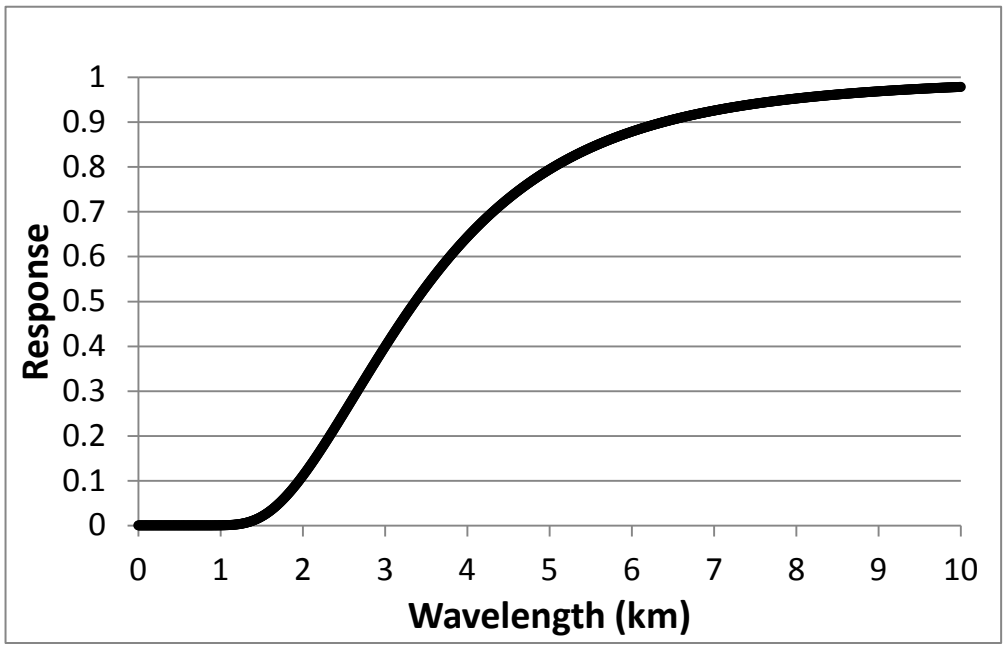

FIG. 3.4. Theoretical Barnes filter response function for a two-pass filter with $\kappa_o = 2.98$ km^2 (the smoothing parameter used for all dual and multi-Doppler syntheses) for the first pass. On the second pass, $\kappa = 0.3\ \kappa_o$.

Chapter 4

Results: Storm environment and outflow characteristics analyses

4.1 Storm Environments

Values of all thermodynamic and most dynamic environmental parameters were not significantly different when comparing the environments in which the two supercells evolved. For the parameters of Convective Available Potential Energy (CAPE) and 0–6 km vertical wind shear (6BWD), this is unsurprising, given that these two parameters typically do not discriminate well between nontornadic and tornadic supercell environments. Values of 6BWD (30–40 knots) were on the lower end of climatology for weakly tornadic supercells and a bit below climatology for significantly tornadic supercells (Fig. 4.1a). Values of CAPE (1300–2500 Jkg^{-1}) fell within climatologies for all supercell types (Fig. 4.1b).

The parameters of Lifting Condensation Level (LCL) and 0–1 km storm-relative helicity (SRH1), traditionally found to discriminate well between nontornadic and tornadic supercell environments, did not do so strongly on 10 June 2010. Values of LCLs were a bit lower in the environment of the nontornadic supercell (940–1280 m) than that of the tornadic supercell (1170–1440 m) (Fig. 4.2). LCLs in both environments were generally within climatology for all supercell types (Fig. 4.3a). Values of SRH1 were higher in the environment of the tornadic supercell (53–187 m^2s^{-2}) than that of the nontornadic supercell (7–138 m^2s^{-2}) (Fig. 4.4). As storm-relative helicity is a measure of the potential for low-level updraft rotation, the values suggest that the environment near the tornadic supercell was more favorable for tornado generation. SRH1 in both

environments fell within climatology for weakly tornadic supercells, but below that for significantly tornadic supercells (Fig. 4.3b).

Values of the Significant Tornado Parameter (STP) were higher in the environment of the tornadic supercell (0.4–1.6) than that of the nontornadic supercell (0.0–1.0), likely resulting from the higher values of SRH1 in the former environment (Fig. 4.5). STP in both environments fell within climatology for weakly tornadic supercells, but well below the climatology for significantly tornadic supercells (Fig. 4.6).

Caution must be exercised in interpreting physical implications of any differences seen in the STP, SRH1, or LCL parameters. The soundings from which these parameters were calculated and compared, while having the greatest spatial and temporal proximity to the given supercell relative to the other soundings, were up to 60 km away from the supercell in earlier stages of its evolution. Additionally, finer sounding data resolution, especially between the tracks of the two storms, may be necessary to capture any significant gradients in any of the parameters in the two environments.

Overall, there do not seem to be any obvious differences between the two storm environments that would help explain why one supercell produced no tornadoes and the other generated two tornadoes, aside from higher 0–1 km storm relative helicity in the tornadic supercell environment. Thermodynamic parameters were suggestive of an environment supportive of at least a weakly tornadic supercell. Dynamic parameters were more marginal, but still indicative of an environment that might be able to support a weakly tornadic supercell.

4.2 Outflow characteristics

Measurements collected by both the mobile mesonet fleet and StickNets suggest that neither storm on 10 June 2010 had a very cold outflow. Mobile mesonet and StickNet measurements should not be compared to each other owing to differences in their response times, so their results will be presented separately, beginning with mobile mesonet measurements. Maximum virtual potential temperature deficits ($|\theta_v'|$) across the outflows rarely exceeded 5–6°C at any time. For example, at 0018 UTC, $|\theta_v'|$ of 6°C was measured across the nontornadic supercell's RFD (Fig. 4.7), which falls within the typical range of deficits in nontornadic supercells—at least 4 to 7°C (Markowski et al. 2002). Measurements collected across the northern flank of the tornadic supercell's FFD at 0116 UTC, as the first tornado was dying, indicate $|\theta_v'|$ of 3°C (Fig. 4.8), quite comparable to the weak baroclinicity measured east-west across the FFD of the nontornadic supercell at 0018 UTC (3°C). Approximately thirty minutes later in the tornadic supercell, at 0148 UTC, right around the time at which a storm spotter reported a brief tornado (unconfirmed by VORTEX2 reports), $|\theta_v'|$ of 5°C was measured in the southern FFD region (Fig. 4.9).

Additionally, mobile mesonet measurements suggest that maximum equivalent potential temperature deficit magnitudes ($|\theta_e'|$) across the outflows rarely exceeded 7°C in either storm. For example, $|\theta_e'|$ at 0018 UTC in the nontornadic supercell was 6°C (Fig. 4.10), much lower than the typical $|\theta_e'|$ measured in nontornadic supercells, 10–12 °C (Markowski et al. 2002). During the tornadic supercell's tornadic phase at 0116 UTC, $|\theta_e'|$ was 6°C across the northern flank of the FFD (Fig. 4.11). At 0148 UTC, $|\theta_e'|$ was 8°C across the southern flank of the FFD (Fig. 4.12).

StickNet measurements indicated that $|\theta_v'|$ measurements (available for thirty minutes during the tornadic supercell's nontornadic phase) peaked at 6–7°C, and the higher deficits (i.e., colder outflows) were found deep in the RFD region on the western flank of the supercell. For example, $|\theta_v'|$ was 7°C at 0202 UTC far to the west in the RFD (Fig. 4.13). $|\theta_e'|$ of up to 12°C was found deep in the RFD at the same time (Fig. 4.14). The presence of such a θ_e trough is consistent with the low-level thermodynamic structure in this region noted in simulations (Beck and Weiss 2013).

At most times in both storms, the outflows weren't particularly cold and did not seem inhibitive to the production of *weak* tornadoes. Both outflows were, however, cold relative to outflows in significantly tornadic supercells.

Additionally, selected parcels deep in the cold pool that likely had trajectories into the mesocyclone (or hypothetical tornado) did not lack potential buoyancy. Inserting mobile mesonet measurements of such parcels into the particular's storm inflow sounding resulted in surface-based CIN and CAPE that were different compared to those of the inflow environment (sounding), but not unfavorable. For example, a parcel evaluated in the RFD at 0018 UTC in the nontornadic supercell had over 1300 Jkg^{-1} less CAPE than a surface parcel in the inflow environment and over 90 Jkg^{-1} greater CIN. However, if sufficient dynamical forcing were exerted to lift this parcel, it would still have plenty of energy to continue its vertical excursion.

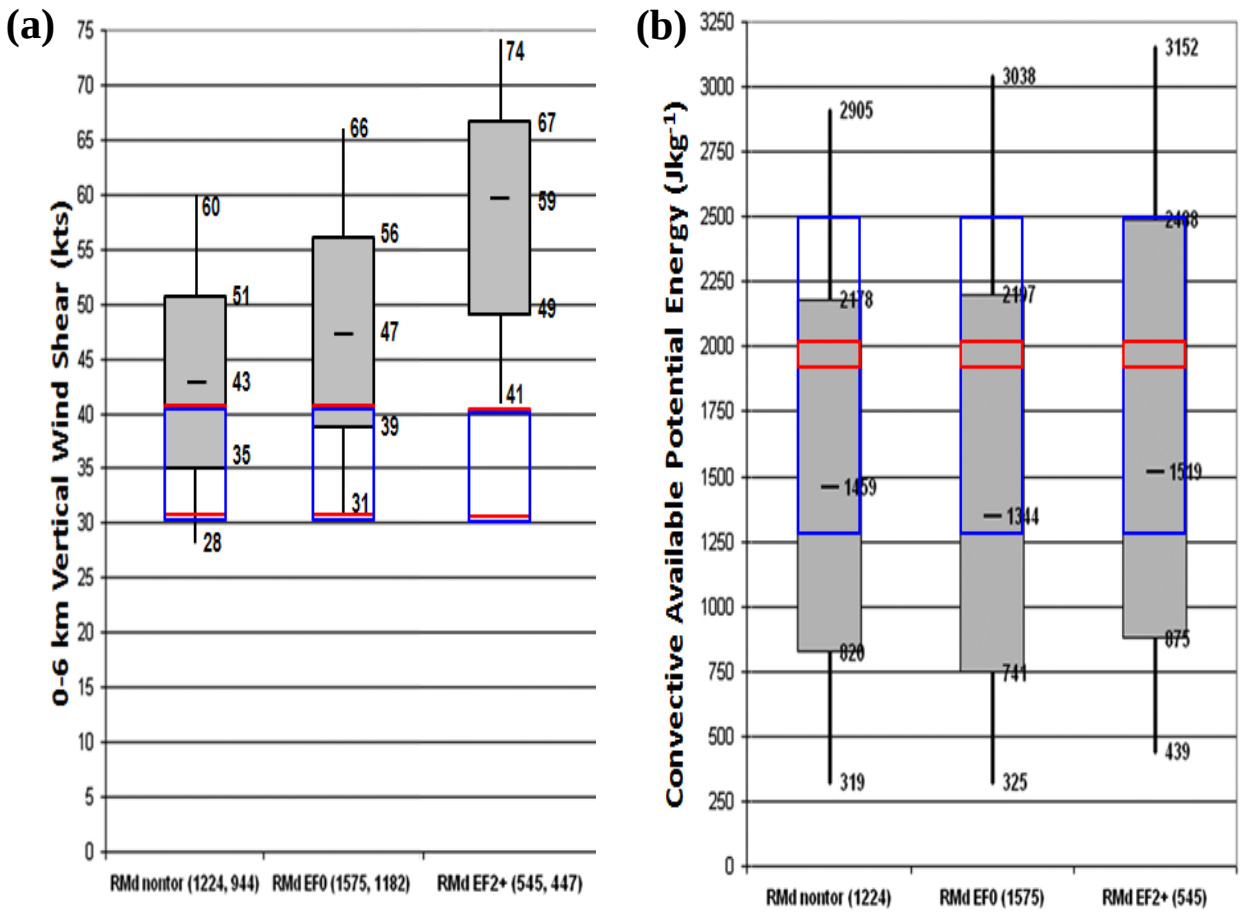

FIG. 4.1. Adapted from Thompson et al. 2012. Box and whisker plots of climatology of nontornadic ('RMd nontor'), weakly tornadic ('RMd EF0'), and significantly tornadic ('RMd EF2') storm environments represented by (a) 0–6 km vertical wind shear and (b) convective available potential energy. Numbers are of the various quartiles of the climatological parameter data. Blue boxes show the range of the given parameter in the environment of the nontornadic supercell on 10 June 2010 and red boxes, the range of the given parameter in the environment of the tornadic supercell. Note that for the sake of consistency, the parameter of convective available potential energy was only calculated up to 300 mb for all soundings, since some soundings were prematurely cut-off prior to reaching equilibrium level. Thus, values of convective available potential energy shown for 10 June 2010 are lower than the actual values on this day, and care must be taken in comparing 10 June 2010 values to climatology.

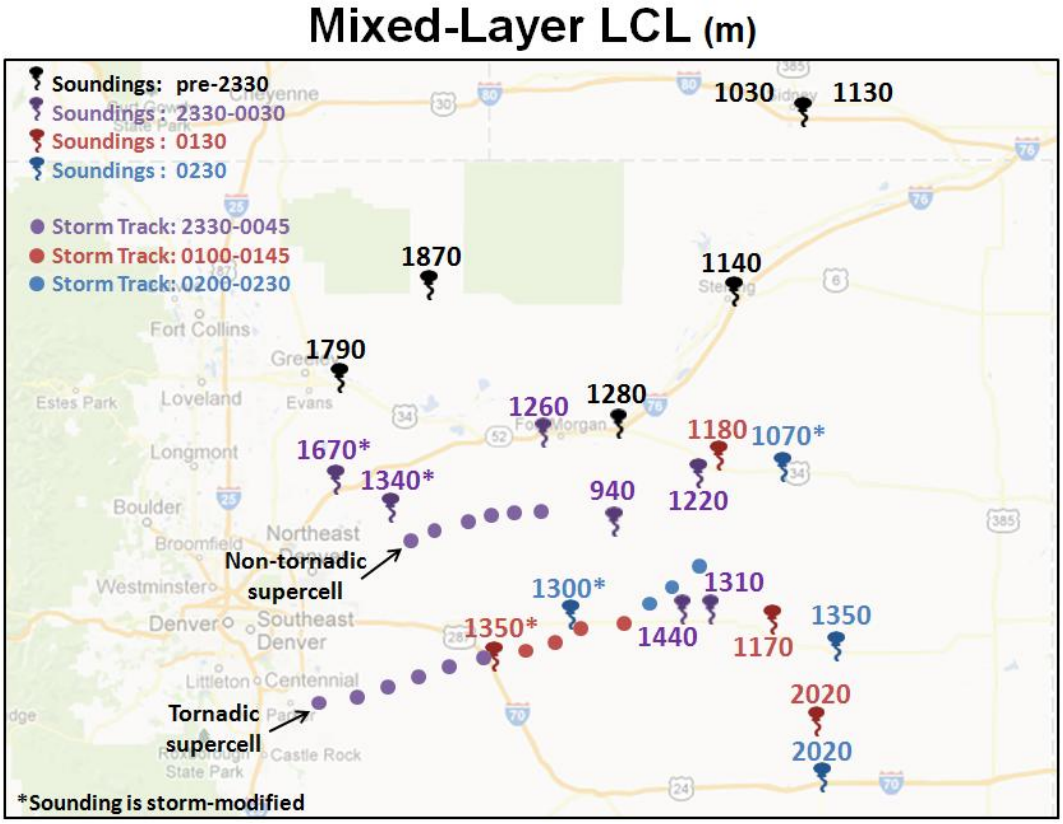

FIG. 4.2. 10 June 2010 storm environment as represented by lifting condensation level (m). Balloon icons denote the launch location of each sounding, color-coded with respect to launch time. Dots denote the storm tracks, based on the location of the midlevel mesocyclone and color-coded with respect to time.

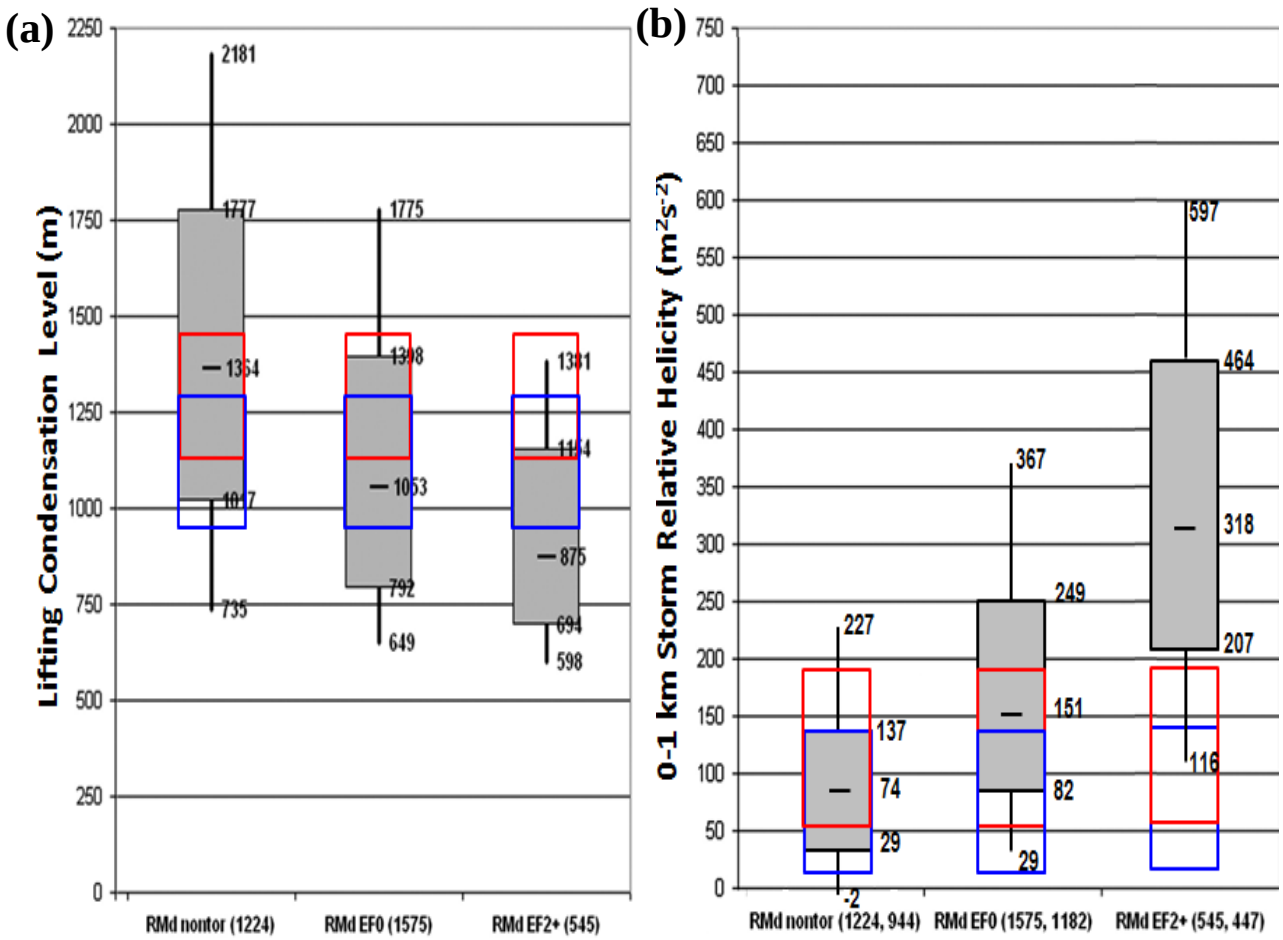

FIG. 4.3. Adapted from Thompson et al. 2012. Box and whisker plots of climatology of nontornadic ('RMd nontor'), weakly tornadic ('RMd EF0'), and significantly tornadic ('RMd EF2') storm environments represented by (a) lifting condensation level and (b) 0–1 km storm-relative helicity. Numbers are of the various quartiles of the climatological parameter data. Blue boxes show the range of the given parameter in the environment of the nontornadic supercell on 10 June 2010 and red boxes, the range of the given parameter in the environment of the tornadic supercell.

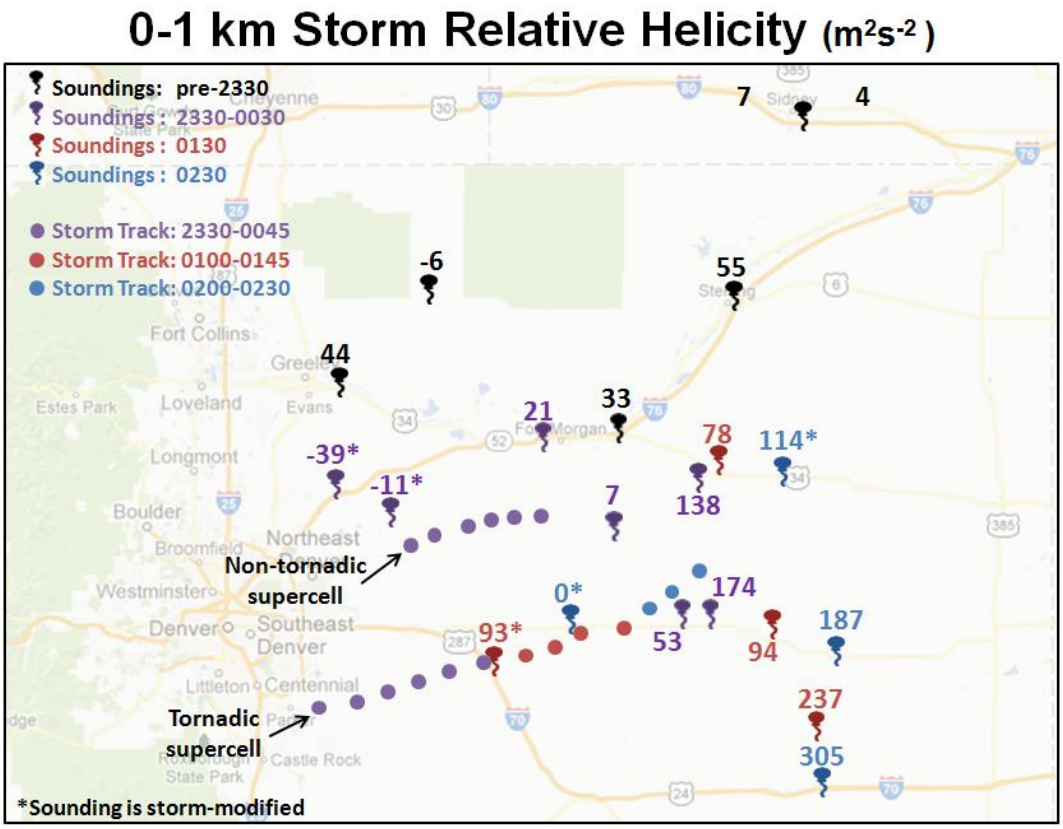

FIG. 4.4. 10 June 2010 storm environment as represented by 0–1 km storm-relative helicity ($m^2 s^{-2}$). Balloon icons denote the launch location of each sounding, color-coded with respect to launch time. Dots denote the storm tracks, based on the location of the midlevel mesocyclone and color-coded with respect to time.

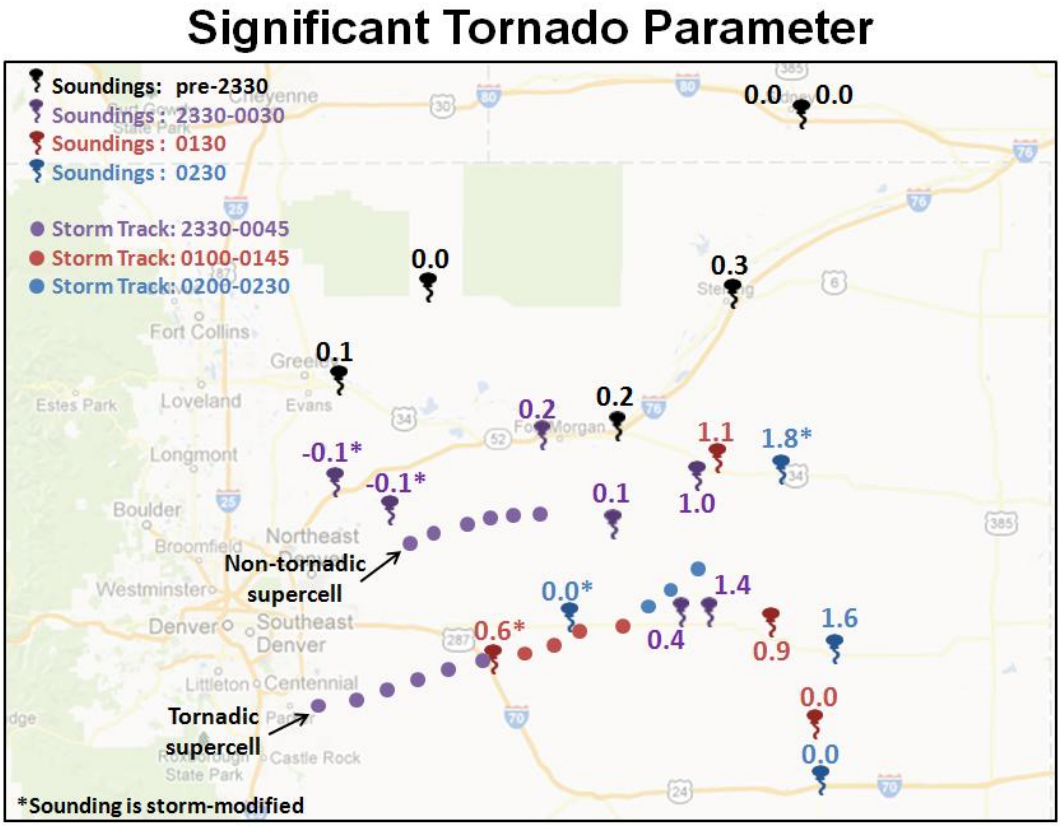

FIG. 4.5. 10 June 2010 storm environment as represented by significant tornado parameter (dimensionless). Balloon icons denote the launch location of each sounding, color-coded with respect to launch time. Dots denote the storm tracks, based on the location of the midlevel mesocyclone and color-coded with respect to time.

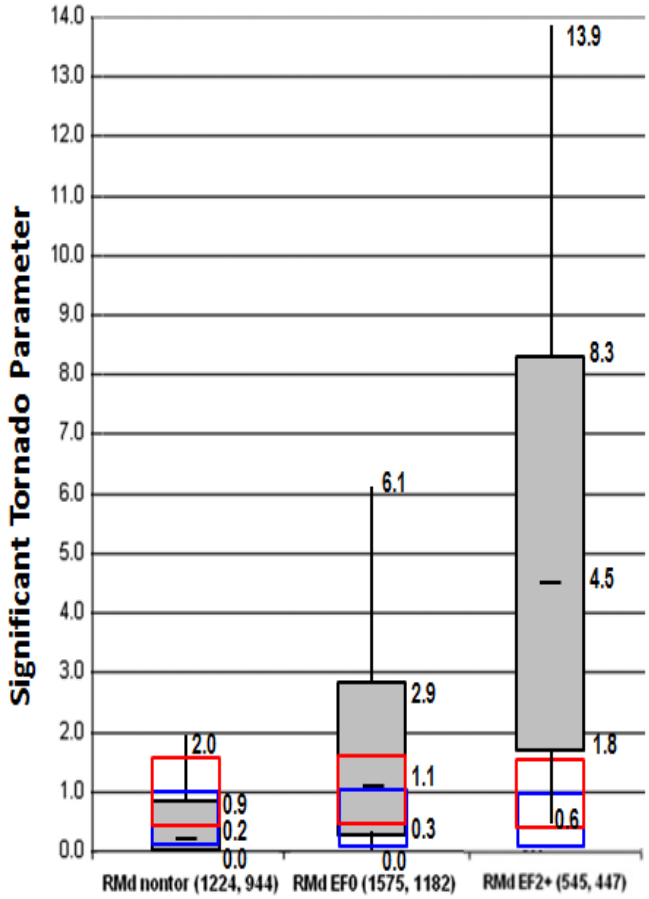

FIG. 4.6. Adapted from Thompson et al. 2012. Box and whisker plots of climatology of, from left to right, nontornadic ('RMd nontor'), weakly tornadic ('RMd EF0'), and significantly tornadic ('RMd EF2') storm environments represented by STP. Numbers are of the various quartiles of the climatological parameter data. Blue boxes show the range of the given parameter in the environment of the nontornadic supercell on 10 June 2010 and red boxes, the range of the given parameter in the environment of the tornadic supercell.

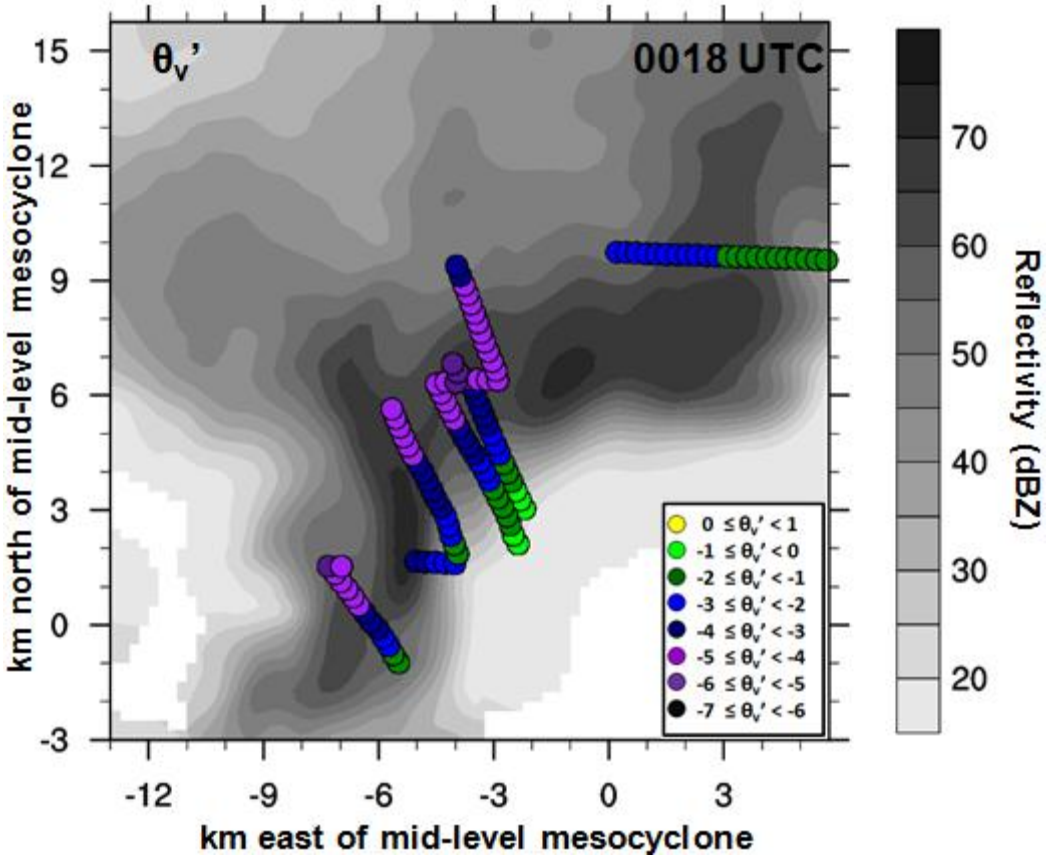

FIG. 4.7. Mobile mesonet-measured virtual potential temperature perturbations (color-coded circles, relative to base state of 315.9 K) in the outflow of the nontornadic supercell at 0018 UTC, overlayed on 750 m logarithmic equivalent reflectivity factor (dBZ, shaded contours) from SR2.

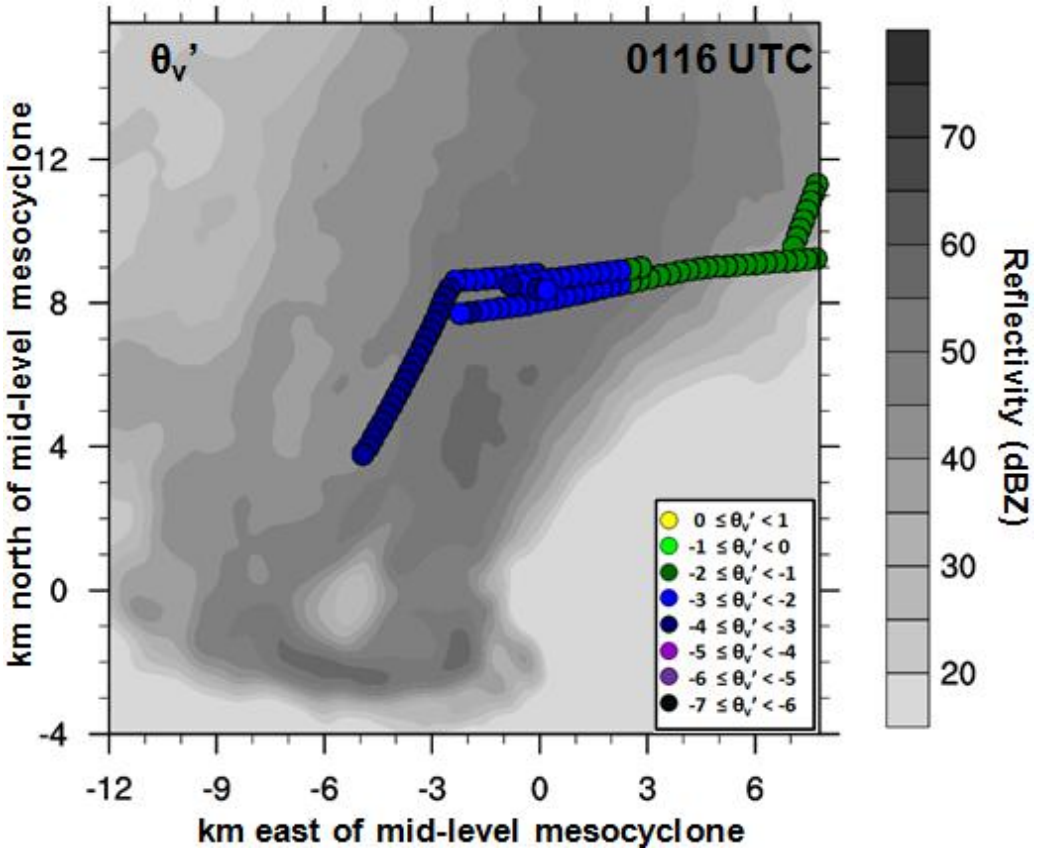

FIG. 4.8. Mobile mesonet-measured virtual potential temperature perturbations (color-coded circles, relative to base state of 314.7 K) in the outflow of the tornadic supercell at 0116 UTC, overlayed on 800 m logarithmic equivalent reflectivity factor (dBZ, shaded contours) from DOW7.

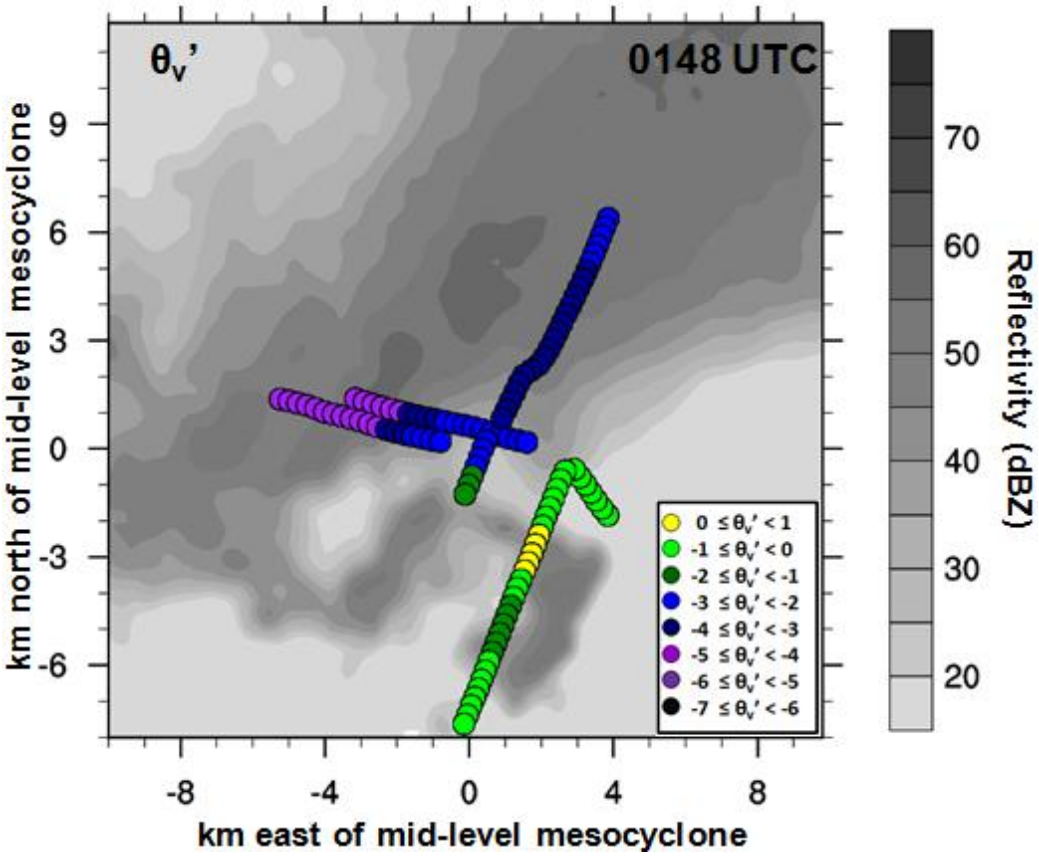

FIG. 4.9. Mobile-mesonet measured virtual potential temperature perturbations (color-coded circles, relative to base state of 314.7 K) in the outflow of the tornadic supercell at 0148 UTC, overlayed on 800 m logarithmic equivalent reflectivity factor (dBZ, shaded contours) from NOXP.

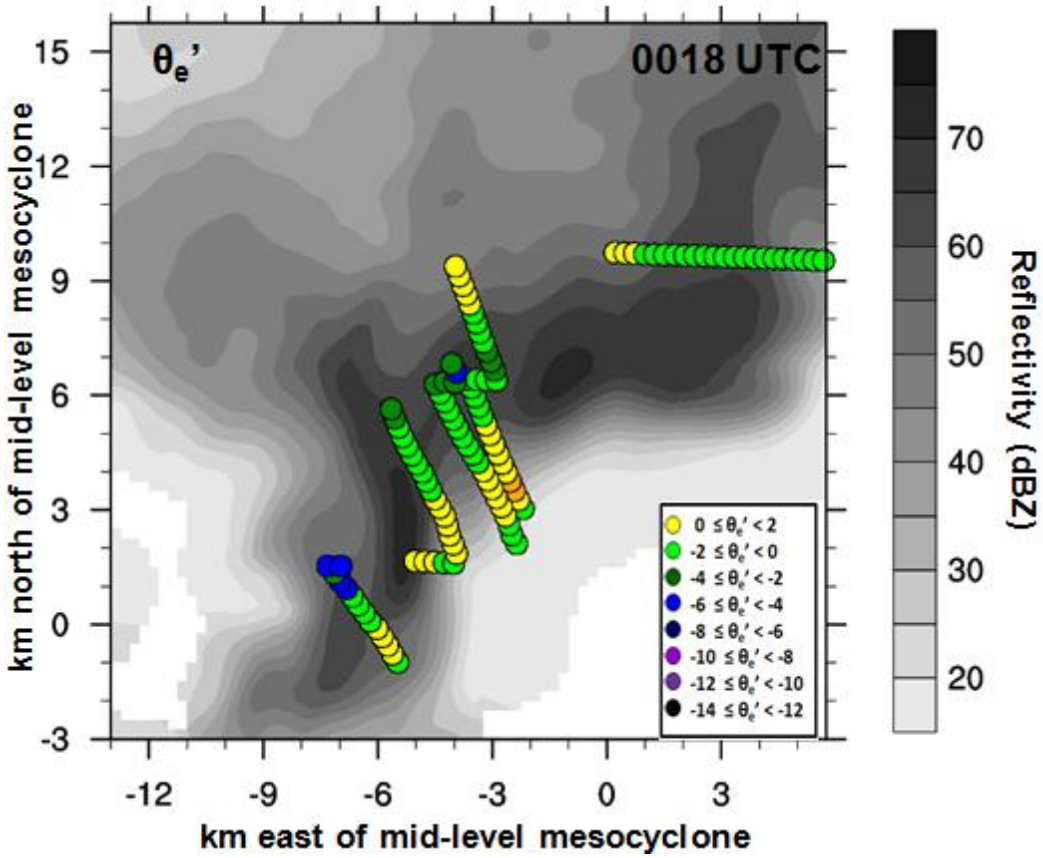

FIG. 4.10. Mobile mesonet-measured equivalent potential temperature perturbations (color-coded circles, relative to base state of 356.8 K) in the outflow of the nontornadic supercell at 0018 UTC, overlayed on 750 m logarithmic equivalent reflectivity factor (dBZ, shaded contours) from SR2.

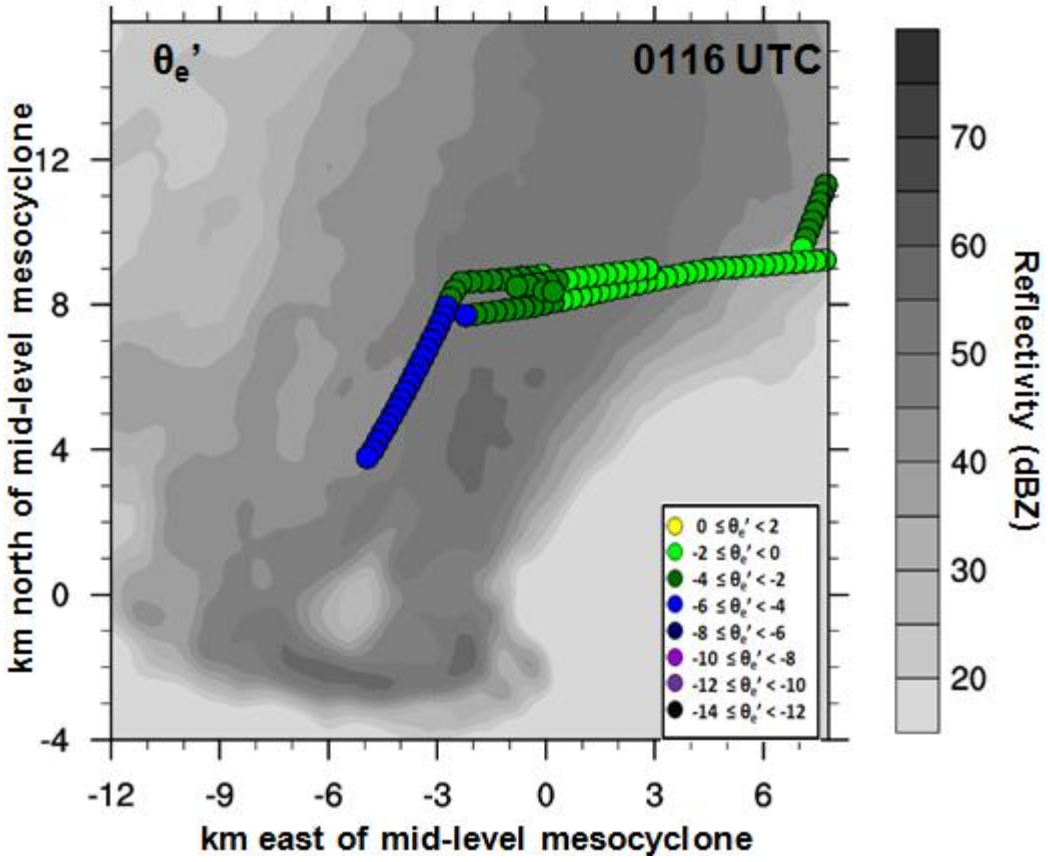

FIG. 4.11. Mobile mesonet-measured equivalent potential temperature perturbations (color-coded circles, relative to base state of 358.9 K) in the outflow of the tornadic supercell at 0116 UTC, overlayed on 800 m logarithmic equivalent reflectivity factor (dBZ, shaded contours) from DOW7.

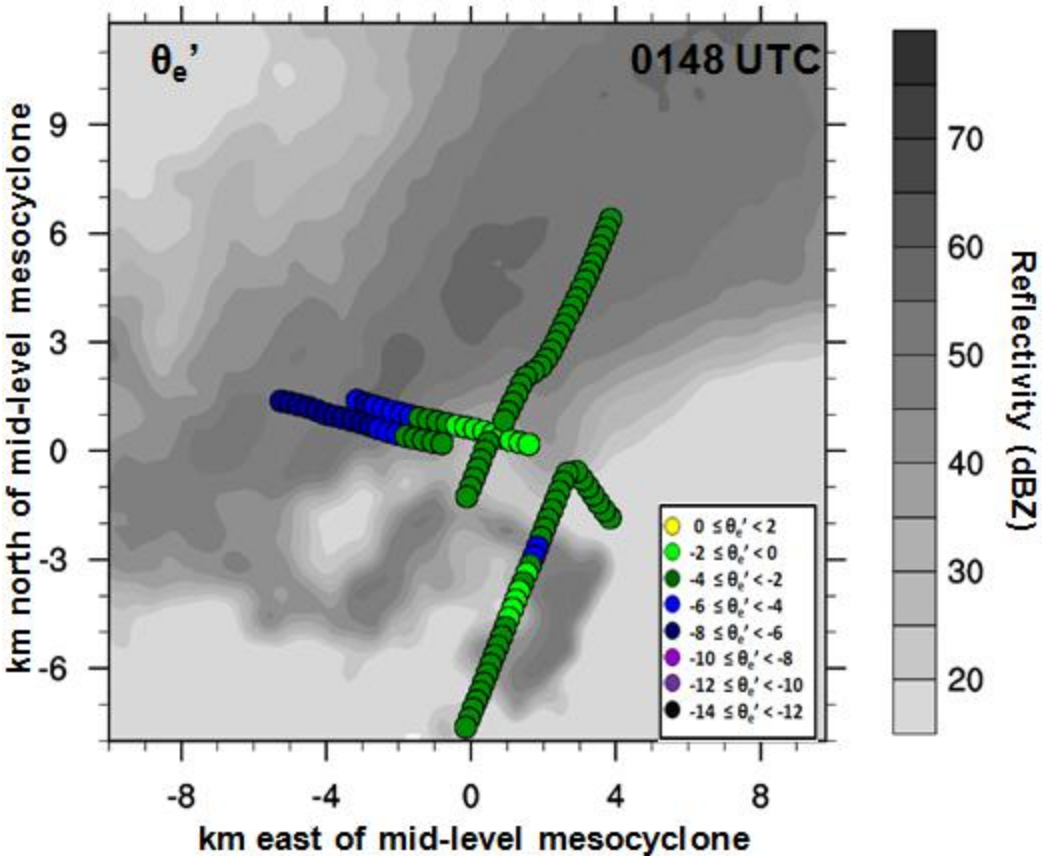

FIG. 4.12. Mobile-mesonet measured equivalent potential temperature perturbations (color-coded circles, relative to base state of 358.9 K) in the outflow of the tornadic supercell at 0148 UTC, overlayed on 800 m logarithmic equivalent reflectivity factor (dBZ, shaded contours) from NOXP.

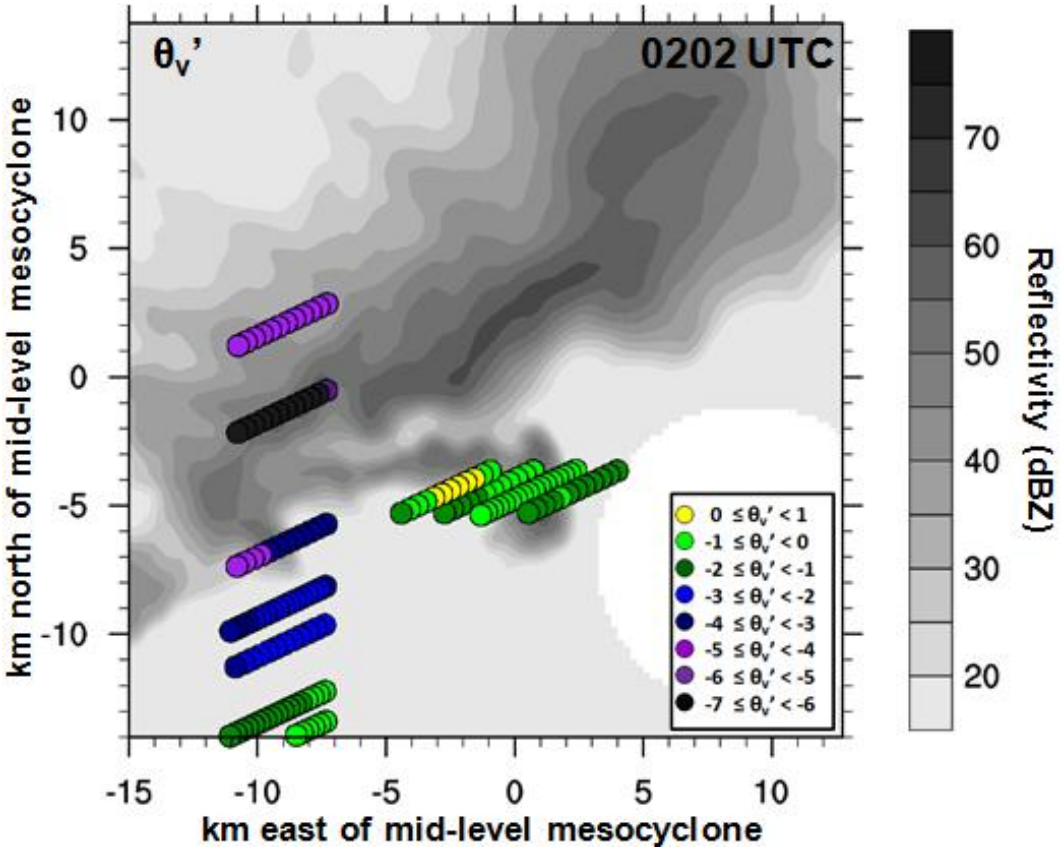

FIG. 4.13. StickNet-measured virtual potential temperature perturbations (color-coded circles, relative to base state of 314.7 K) in the outflow of the tornadic supercell at 0202 UTC, overlayed on 750 m logarithmic equivalent reflectivity factor (dBZ, shaded contours) from NOXP.

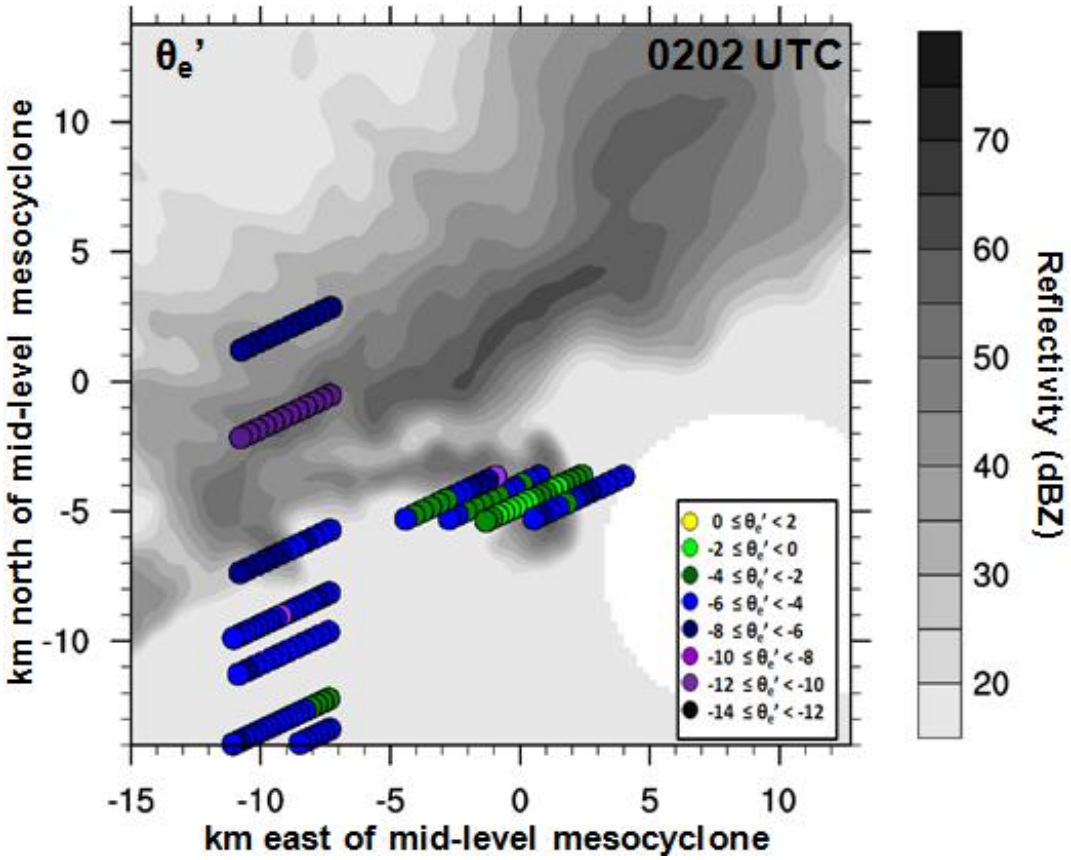

FIG. 4.14. StickNet-measured equivalent potential temperature perturbations (color-coded circles, relative to base state of 358.9 K) in the outflow of the tornadic supercell at 0202 UTC, overlayed on 750 m logarithmic equivalent reflectivity factor (dBZ, shaded contours) from NOXP.

Chapter 5

Results: Radar analyses

5.1 Nontornadic supercell

5.1.1 Overview

The nontornadic supercell initiated at approximately 2230 UTC just to the east of the foothills of the Rocky Mountains. It intensified into a supercell quickly, and the NWS issued a tornado warning at 2342 UTC. Around the same time, the VORTEX2 armada began deploying on this supercell. While possessing a visually impressive updraft and mesocyclone, especially earlier in its life (Fig. 5.1), this storm never produced a tornado.

Generally, this storm possessed many of the classic features of tornadic supercells (Lemon and Doswell 1979), but with a few differences. The supercell had a forward-flank downdraft (FFD) and rear-flank downdraft (RFD), but the RFD did not wrap around, indicating that the storm was not occluded; an occluded structure is favorable for tornadogenesis (Fig. 5.2). An additional departure from the traditional structure of a tornadic supercell was the lack of a well-developed low-level mesocyclone (Fig. 5.3a,b). A well-defined mesocyclone was not evident in the dual-Doppler data below altitudes of 2-2.5 km (Fig. 5.3c,d). An important caveat is that the SR radars had great difficulty collecting high-quality velocity data in low-reflectivity regions, such as those containing the mesocyclone at heights below 2 km. Thus, the mesocyclone *may* have been present at lower altitudes than suggested by the dual-Doppler data, with its presence obscured by noise. However, near-surface winds measured by the mobile mesonet fleet did not

indicate strong rotation (Fig. 5.4). Visual observations made by the NCAR/LSC photogrammetry team further support a lack of significant low-level rotation. The combination of various data leads to the assumption that there was not a prominent, persistent *low-level* mesocyclone in this storm.

Another feature in this storm was a region of anticyclonic vorticity to the west of the mesocyclone. Anticyclonic vorticity was present at the midlevels at all times and at lower-levels (1 km) after 0012 UTC. The low-level anticyclonic vorticity strengthened significantly from 0012–0021 UTC, leading to the development of anticyclonic curvature in the reflectivity field (Fig. 5.3d). By 0024 UTC, there were two anticyclonic vortices at 1.5 km and above, one to the northwest of the mesocyclone, and the other due west of the mesocyclone (Fig. 5.3d). By 0033 UTC, only the southern vortex remained.

5.1.2 Merger

Perhaps the most interesting process associated with this supercell was a merger with a convective cell that developed between the two original supercells. This merger ultimately led to the nontornadic supercell's demise and may also have had an impact on the structure of the tornadic supercell prior to tornado production. Thus, this merger plays a critical role in this study.

By 0014 UTC, a new cell, hereafter referred to as 'Cell A,' initiated between the nontornadic and tornadic supercells, near the intersection of their gust fronts (Fig. 5.5). Over time, Cell A intensified, increased in size, and continued approaching the nontornadic supercell. The merger began around 0037 UTC, marked by the joining of the two 35 dBZ reflectivity maxima (Rogers 2012) associated with Cell A and the nontornadic supercell. However, the nontornadic supercell seemed to experience

detrimental impacts from the merger event from 0024 UTC onward.

Dual-Doppler derived analyses suggest that the updraft and mesocyclone in the nontornadic supercell generally weakened beginning at 0024 UTC. The strength of the updraft is characterized here in terms of the mass flux at all points in the updraft at 2 km with $w > 10$ ms^{-1}, i.e., the core of the updraft (the dotted box in Fig. 5.3a shows the region considered to find these points). Mass flux was used instead of maximum updraft speed to provide a more robust measure of the updraft strength as a whole, rather than the values at a one grid-point maximum, which can be somewhat volatile. The mass flux increased from 0024–0027 UTC (likely due to increasing dual-Doppler coverage of the updraft, rather than an actual intensification of the updraft) and then decreased from 0027 UTC onward, suggesting a weakening of the updraft (Fig. 5.6). Similarly, analyses of dual-Doppler-derived mesocyclone strength, measured in terms of maximum vertical vorticity, show that the strength of the mesocyclone decreased quite significantly from 0024/0027–0033 UTC, dropping by at least $0.8 \cdot 10^{-2}$ s^{-1} over this time period at heights ranging from 1.5 km to 3 km (Fig. 5.7).

Evidence suggests that the merger weakened the updraft and the mesocyclone through a combination of (1) cooling the inflow and (2) raining into the updraft. First, virtual potential temperature deficits ($|\theta_v'|$) in the inflow region at 0051 UTC (during the peak of the merger) were up to 4°C greater than deficits measured in this region at 0012 UTC (well-prior to the merger) (Figs. 5.8, 5.9), and equivalent potential temperature deficits ($|\theta_e'|$), up to 2°C greater. These differences indicate that the inflow was a few degrees colder after the merger. When an updraft ingests relatively ‘cold’ air, it typically weakens, due to the reductions in buoyancy.

Second, as Cell A approached and then merged with the supercell, the updraft became increasingly ensconced in reflectivity, made especially clear when analyzing 3-D isosurfaces of reflectivity and vertical velocity fields prior to and during the merging (Fig. 5.10). Quantitatively, the percentage of points in the updraft (i.e., those points with $w > 10$ ms^{-1}) having reflectivity values exceeding 35 dBZ jumped from just above 10% to over 90% from 0024–0033 UTC (Fig. 5.11). Assuming that hydrometeor loading increases with increasing reflectivity (which is not always a good assumption), the increased reflectivity would imply that the updraft had less effective buoyancy.

As the mesocyclone and updraft weakened, the storm increasingly lost its original supercellular structure and was consumed by Cell A. By 0047 UTC, a little over 20 minutes prior to the production of the first tornado in the tornadic supercell, Cell A had developed an established outflow, as evidenced by the convergence zone along the eastern flank of this storm (Fig. 5.12a). By 0110 UTC, the time of tornadogenesis, this line of convergence (gust front) was quite strong, and seemed to extend deep into the tornadic supercell (Fig. 5.12b). It is difficult to evaluate, with confidence, the extent of the impact on the tornadic supercell, especially with regard to potential enhancement of favorable conditions for tornado production. However, it is safe to say that the outflow of Cell A influenced the structure of the tornadic supercell, possibly in a way that made tornadogenesis more favorable.

As time progressed, Cell A gradually weakened. By 0140 UTC, Cell A had separated itself from the tornadic supercell and moved to the north-northwest, dissipating by 0215 UTC (not shown).

5.2 Tornadic supercell

5.2.1 Overview

The tornadic supercell initiated at approximately the same time as the nontornadic supercell (2230 UTC) on the eastern edge of the foothills of the Rocky Mountains. At 0037 UTC, the first of three tornado warnings was issued on this supercell. Two tornadoes were generated by the storm from 0109–0115 UTC and 0122–0126 UTC, respectively. After the two tornado events, the storm entered a long nontornadic phase (Fig. 5.13) but was still quite active, with multiple cycles of mesocyclogenesis observed as well as, at and after dark, multiple funnels near cloud base.

Consistent with the classic supercell structure, this storm appeared to have a low-level mesocyclone during the majority of the VORTEX2 deployment on it. Half of a well-defined mesocyclone, with strongly wrapping winds evident, is seen in dual-Doppler syntheses at 0.5 km and 1.0 km. This suggests that there likely was a low-level mesocyclone, but noise obscured the half of it that was in a region of lower reflectivity. Observations made by the photogrammetry team also suggest the presence of a low-level mesocyclone. Near-surface wind data collected by the mobile mesonet fleet hints at the presence of near-surface rotation (Fig. 5.14). An analysis of the midlevel mesocyclone follows in 5.2.3.

5.2.2 Tornado evolution

The evolution of the two visible tornadoes[1] generated by the tornadic supercell (Fig. 5.15) is of particular interest, given that they occurred within a few minutes of each other, had different characteristics (the second was rain-wrapped but the first was not), and did not follow the classic model of cyclic mesocyclogenesis prior to the production

[1]In this study, a visible tornado is defined as a condensation funnel in contact with the ground.

of the second tornado.

To characterize the evolution of the two tornadoes in terms of the strength of the circulation, radial velocity differential, the best estimate of strength obtainable from single-Doppler data, was used (Fig. 5.16). This quantity was calculated using the most extreme inbound and outbound radial velocities separated by no greater than 500 m, i.e., velocities that were either gate-to-gate or were separated by no greater than one row of noise. If the radial velocity differential across the couplet was at least 40 m s^{-1} (Alexander and Wurman (2008)), the circulation was considered to meet the criteria for tornado strength. If a relative minimum in inbound velocity and relative maximum in outbound velocity were located within 500 m of each other, the circulation was considered to be 'compact.' The presence or lack of a tornado was determined by visual observations made by the photogrammetry team and others in the field.

The first tornado developed at approximately 0109 UTC and had a visually well-defined funnel, as it was located to the east of the bulk of the precipitation (Fig. 5.17). It tracked to the east and maintained a constant strength, at or above tornado strength, at all heights analyzed until 0114 UTC. Then, at almost all heights, the circulation weakened at least 5 m s^{-1}, even falling below tornado strength aloft. Correspondingly, visual ground observations suggest that the tornado began dissipating—e.g., the condensation funnel lost contact with the surface—a little after 0115 UTC (Fig. 5.18).

Then, the circulation aloft (1–2.5 km) generally intensified a bit and then maintained at least tornado strength until 0121 UTC (Fig. 5.16). Closer to the surface, around 0.5 km, the circulation had weakened by 0116 UTC, and still had a decreased strength past 0118 UTC; at these times at these heights, the strength of the circulation fell

below tornado strength. Throughout the transition time between the tornadoes (0115–0122 UTC), the circulation generally seemed to remain compact, with the exception of the circulation at 1.7 and 2.1 km at 0119 UTC (Fig. 5.16).

It is important to note that noise contamination at various times and heights was unfortunately an issue multiple times during this transition period; the noise made a reasonable estimation of circulation strength and size impossible. Thus, the circulation might have weakened more or expanded at some points in the transition period, but this could not be confirmed by the DOW7 data. Additionally, the lowest level at which circulation strength was consistently available was still a few hundred meters above the ground. The presence of a strong and compact circulation at this height does *not* necessarily imply that the circulation had these characteristics closer to the surface.

However, it is safe to say that, generally, during this transition period, even though a visible condensation funnel was not present, the circulation maintained or exceeded tornado strength at levels above 0.5 km. This begs the question of whether the two tornadoes analyzed were associated with two distinct tornadogenesis events, or, instead, were associated with the same event, with the beginning of the evolution of the second tornado heralded by the redevelopment of the visible condensation funnel. For the purpose of this study, they were considered to be two visible tornadoes from a continuous circulation.

The second tornado began at approximately 0122 UTC. The strength of the circulation weakened at all heights throughout the tornado's short life, especially from 0124–0126 UTC. During these last two minutes of the tornado's life, the radial velocity differential was typically below tornado strength, even dipping as low as 20–25 m s^{-1} by

0126 UTC (Fig. 5.16).

The second tornado was also rain-wrapped (Fig. 5.19). After developing, it moved westward relative to the rest of the storm, increasingly into the precipitation region. This relative westward movement was likely due in part to an amplification of a 'surge' in the rear-flank downdraft region, to the due east of the tornado. This surge was likely a rear-flank downdraft internal surge (RFDIS; see 2.3.3), manifest here as enhanced eastward movement of a region of strong inbound velocities (Fig. 5.20).

Also interesting to consider during the evolution of the two tornadoes was the tilt of the tornado with height, i.e., the displacement of the circulation close to the surface from the circulation farther aloft. Such displacement was calculated using the distance between the center of the circulation at a height of approximately 2 km (5°) and that at 400 m (1°) (the latter the lowest height for which there were quality data consistently), and typically suggested that the circulation at a height of 2 km was to the northeast of the circulation at 400 m. Near the beginning of the tornado, this displacement was at its maximum (Fig. 5.21). Then, it decreased for a few minutes, and began increasing again near the end of the first tornado's life. The displacement had a relative peak early in the transition period between the two tornadoes, then decreased until the beginning of the second tornado, and increased until the second tornado dissipated.

The trends evident in the circulation displacement were somewhat consistent with one proposed hypothesis for tornado maintenance, that the near-surface circulation and the main updraft need to be collocated, given the crucial stretching and tilting of vorticity that occurs beneath the main updraft; displacement of the near-surface circulation from the updraft would occur coincident with the weakening of the tornado (Dowell and

Bluestein 2002; Wicker and Wilhelmson 1995). While dual-Doppler data were not available for the time period of the tornadoes on 10 June 2010, and thus the precise location of the updraft is unknown, evaluating the separation of the 2 km and 400 m circulations gives a sense of the tilt of the tornado with height and the displacement of the low-level circulation from upward dynamic perturbation pressure-gradient forces associated with rotation aloft.

The relative peak in the displacement during the transition period of the tornadoes on 10 June 2010 was consistent with the aforementioned hypothesis of the importance of vertically stacked circulations for tornado maintenance, as were the increases in displacement at the end of each tornado's life, and the decrease in displacement at the beginning of the second tornado. The overall maximum in displacement at around 2 minutes into the first tornado was somewhat inconsistent, as such a displacement—in this case, 1.6 km—implies that the circulation was well-separated from that aloft, potentially an unhealthy structure for continued tornado maintenance.

The evolution of the 10 June 2010 tornadoes did not follow the classic model of cyclic mesocyclogenesis prior to the production of a new tornado (Burgess et al. 1982). Rather, the same mesocyclone that produced the first tornado generated the second tornado minutes later. The process causing the spin-up of the second tornado cannot be evaluated with the single-Doppler data.

5.2.3 The evolution of the mesocyclone/cyclic mesocyclogenesis

After the two tornadoes, the supercell entered a long nontornadic phase. During this time, cycles of mesocyclogenesis, the generation of a new low-level and midlevel mesocyclone, were observed. Mainly single-Doppler data were used to analyze the

cyclic mesocyclogenesis, due to severe side-lobe issues (see 3.2.1) encountered by the radars collecting dual-Doppler data in low-reflectivity regions of the storm. As single-Doppler data can be ambiguous, 'circulations,' rather than 'mesocyclones,' were identified and analyzed. A circulation is defined herein to be a cyclonically-rotating azimuthal velocity couplet with a diameter of 1–10 km and radial velocity couplet strength of at least 20 m s^{-1} (French et al. 2008).

The cycle of mesocyclogenesis seemed to begin with the demise of the second tornado around 0126 UTC. By 0129 UTC, the occluded circulation originally, but no longer, associated with a tornado, 'C1,' was tucked back in the RFD (Fig. 5.22a). With height, C1 increased in strength, as well as in northeast displacement relative to its circulation at lower levels. At 0141 UTC (the next available time due to a generator failure in the DOW7 radar), C1 was only a well-defined vortex above 1 km. At about this same height, the beginnings of the development of a new cyclonic circulation to the east, 'C2,' was evident (Fig. 5.22b). C2 formed in the reflectivity hook and by 0147 UTC, was associated with a reflectivity 'hole' (Fig. 5.22c). Interestingly, at around this time, a storm spotter reported a tornado to the National Weather Service office. Careful analysis of low-level data from the DOW7, NOXP, and SR2 radars from this time does not support the presence of a tornado, however.

C2 continued to travel rearward in the storm. By 0153 UTC, a transient, smaller cyclonic vortex developed due east of C2, but had dissipated by 0158 UTC (Fig. 5.22d,e). During this time period, the anticyclonic vortex, 'A1,' associated with the 'anticyclonic reflectivity flare' (Brandes 1981; Fujita 1981) at the end of the now-lengthening reflectivity hook, began significantly strengthening. A1 had been present, albeit weaker,

from prior to 0129 UTC. It is noteworthy that for much of the subsequent time analyzed, A1 was of comparable or greater strength than the cyclonic circulations present, albeit with looser rotation.

By 0204 UTC, rapid development was evident of a new circulation, 'C3,' well to the east-northeast of C2 and northwest of the anticyclonic vortex, along the hook/rear-flank gust front and associated with a northward bulge of the hook (Fig. 5.22f). Additionally, a small velocity couplet to the west-southwest of C3 was developing, but it was not formally considered to be a 'circulation,' given that its strength did not meet the threshold. This couplet, like C2, moved rearward relative to the rest of the storm over time, until it dissipated around 0215 UTC. A cycling of the hook was evident from 0204 UTC through 0215 UTC as C3, and the aforementioned velocity couplet to its west-southwest, continued moving rearward and southward in the storm (Fig. 5.22f–h).

By 0221 UTC, an interesting reflectivity structure in the storm had evolved, as C3 caused the reflectivity to bulge to the south; this structure was even more well-defined at 0227 UTC (Fig. 5.22i,j). As previously discussed, the SR1 and SR2 radars did not properly capture circulation in the low reflectivity region for the lowest few kilometers due to noise issues. In NOXP data (which had fewer noise issues), however, by 0217 UTC, a circulation, 'C4,' began developing in the low reflectivity region north of the hook (to the northeast of C3) (Fig. 5.23a). C4 continued evolving (Fig. 5.23b) through the end of the NOXP data available and, by 0240 UTC, was in the hook, and associated with a reflectivity hole.

Over the hour analyzed (0129–0230 UTC), three new cyclonic circulations (C2, C3, and C4) developed in the rear-flank region of the storm. Generally, at the midlevels,

the circulations traveled rearward relative to the rest of the storm, consistent with the behavior of circulations that developed along the rear-flank gust front in supercells analyzed by French et al. (2008) and Dowell and Bluestein (2002a). In contrast, the anticyclonic circulation remained firmly anchored in place during this time period.

The significant difference in motion of the cyclonic circulations versus the anticyclonic circulation was due to the direction and strength of the storm-relative flow in which the circulations were embedded. For example, as evidenced by the horizontal streamlines analyzed from 0209–0218 UTC, C3 was embedded in strong rearward storm-relative flow, whereas A1 encountered very little storm-relative flow (the streamlines simply show anticyclonic rotation in the region of A1) (Fig 5.24). At lower levels during this time, the region of maximum cyclonic vorticity did not experience rearward motion as significant as it did at midlevels, consistent with the low-level streamlines lacking a strong rearward component.

FIG. 5.1. Photograph of the nontornadic supercell at 2354 UTC, courtesy of the LSC/NCAR Photogrammetry team (CAMA). View is looking to the west.

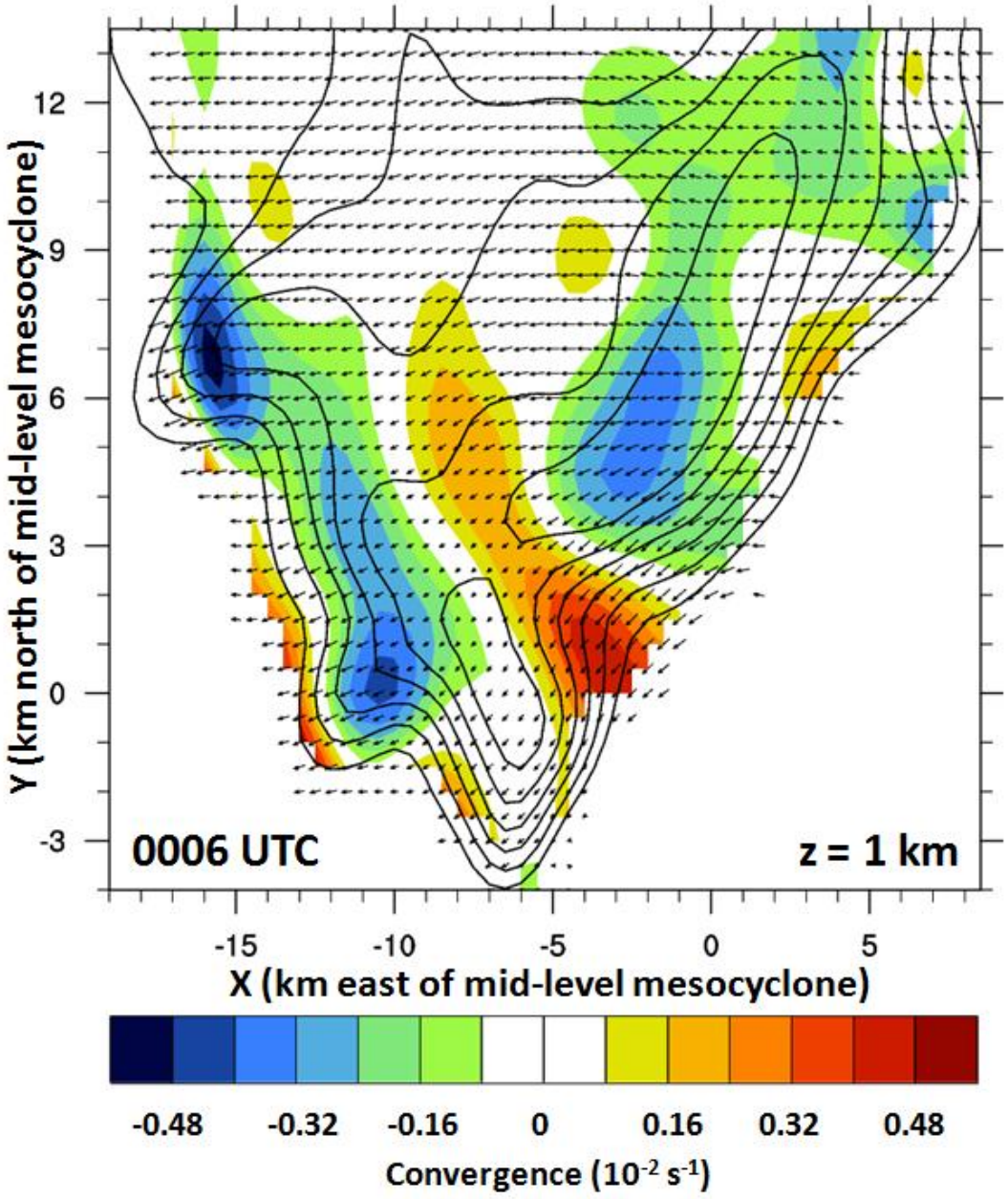

FIG. 5.2. Horizontal convergence (shaded, 10^{-2} s^{-1}) and SR1 logarithmic equivalent reflectivity factor (contoured, every 7 dBZ beginning at 21 dBZ) at 1 km for the nontornadic supercell at 0006 UTC.

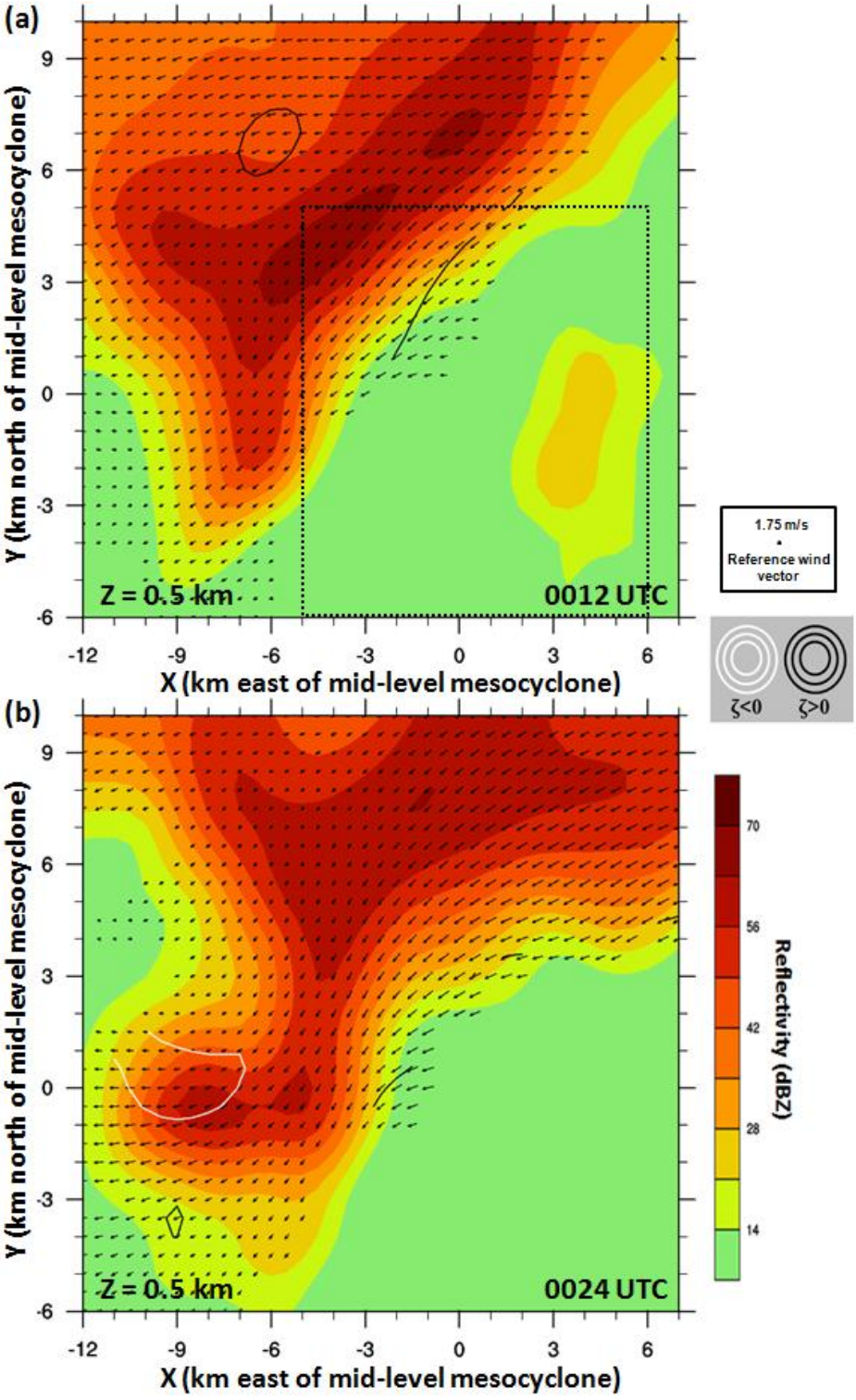

FIG. 5.3. Dual-Doppler derived horizontal winds (vectors) and vertical vorticity (contoured every 0.4, positive in black, negative in white, beginning at +/- 0.4; 10^{-2} s^{-1}) overlayed on SR1 logarithmic equivalent reflectivity factor (shaded, dBZ) of the nontornadic supercell for 0.5 km at (a) 0012 UTC and (b) 0024 UTC and for 2.5 km at (c) 0012 UTC and (d) 0024 UTC. Dashed box in (a) shows the region used for later analyses of characteristics of the updraft.

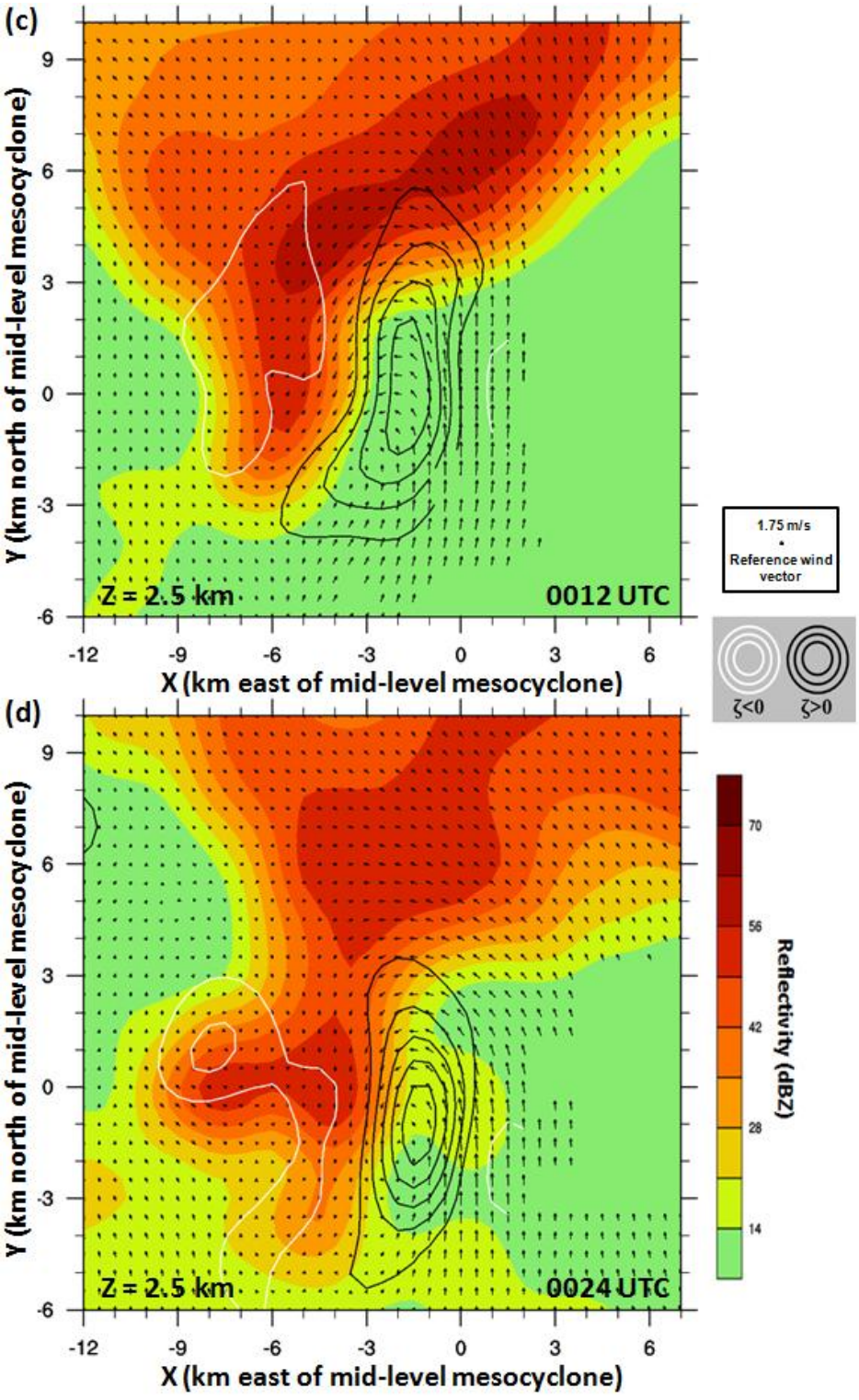

FIG. 5.3, continued.

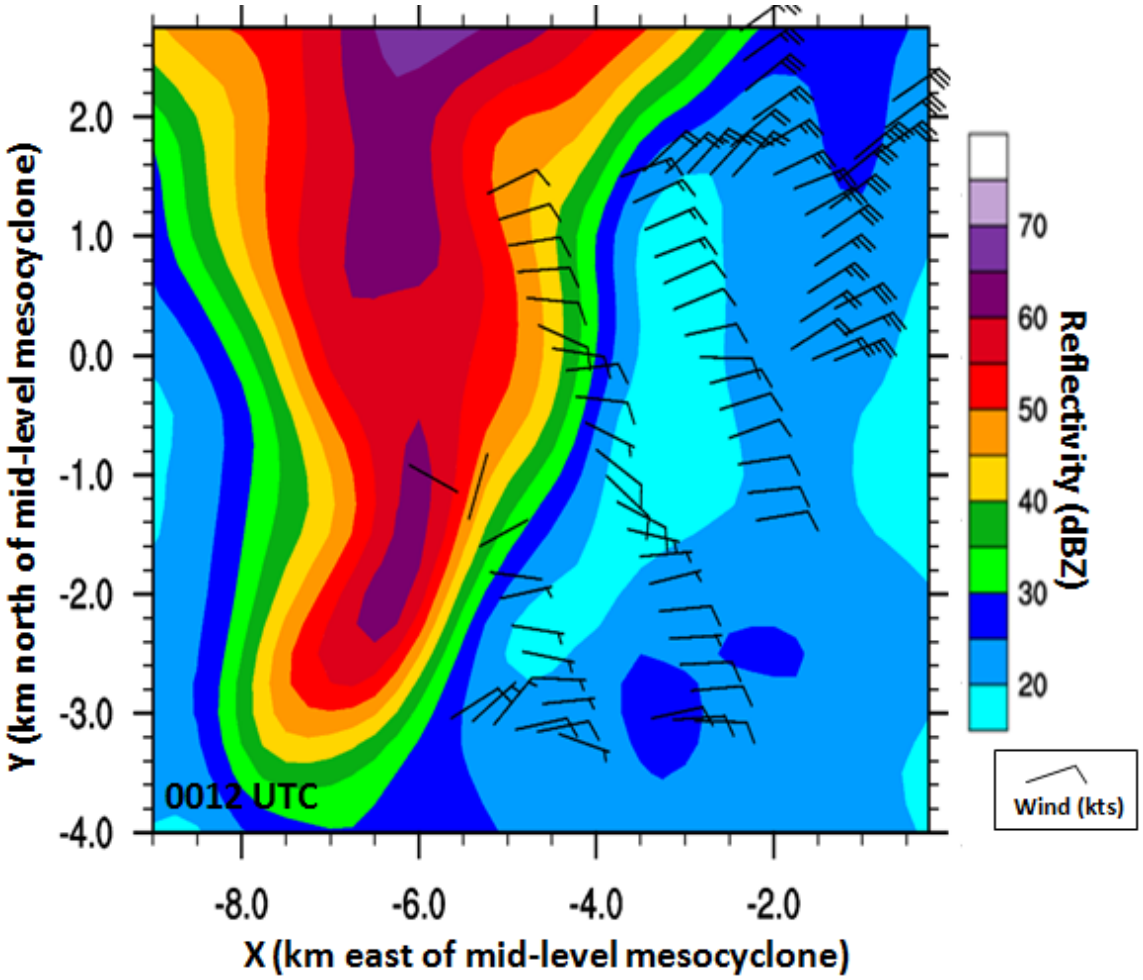

FIG. 5.4. Mobile-mesonet measured near-surface storm-relative winds (kts) in the nontornadic supercell at 0012 UTC, overlayed on 750 m SR1 logarithmic equivalent reflectivity factor (dBZ, shaded contours).

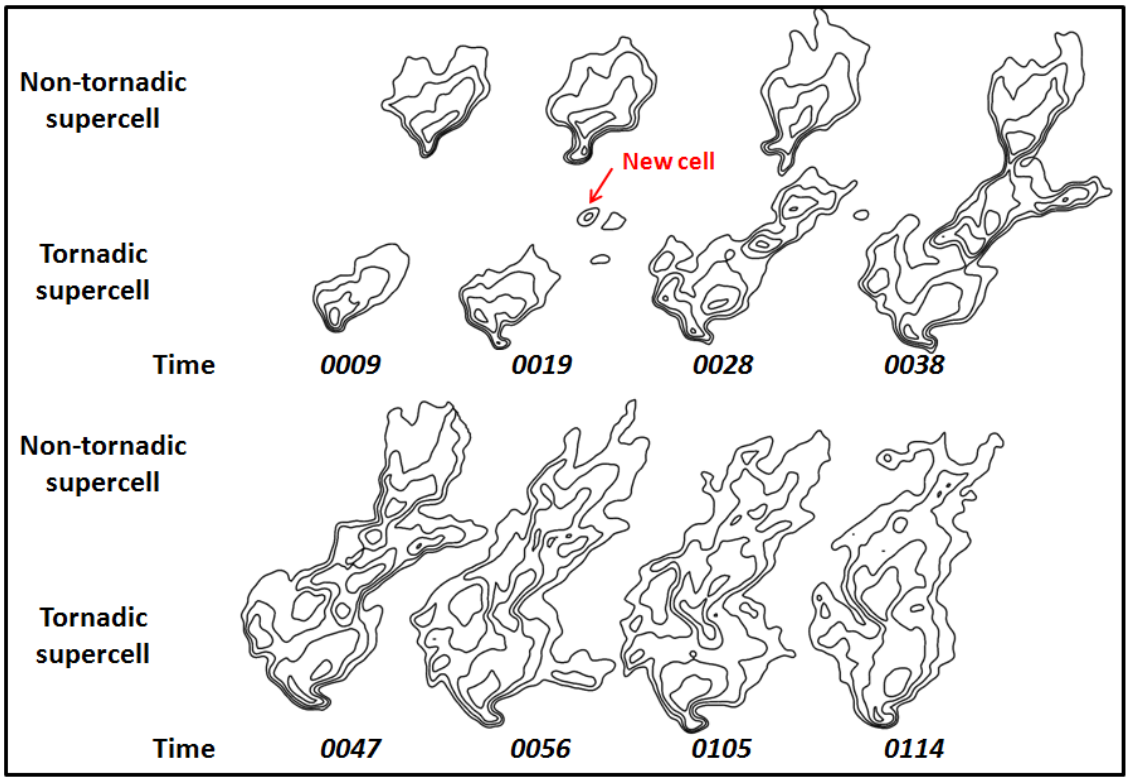

FIG. 5.5. Progression of merger of nontornadic supercell with new cell to its south (pointed out in red). Contours are of KFTG-88D logarithmic equivalent reflectivity factor, every 10 dBZ beginning at 25 dBZ, at heights 1.5 km (0009 – 0047 UTC) or 2.0 km (0056 – 0114 UTC).

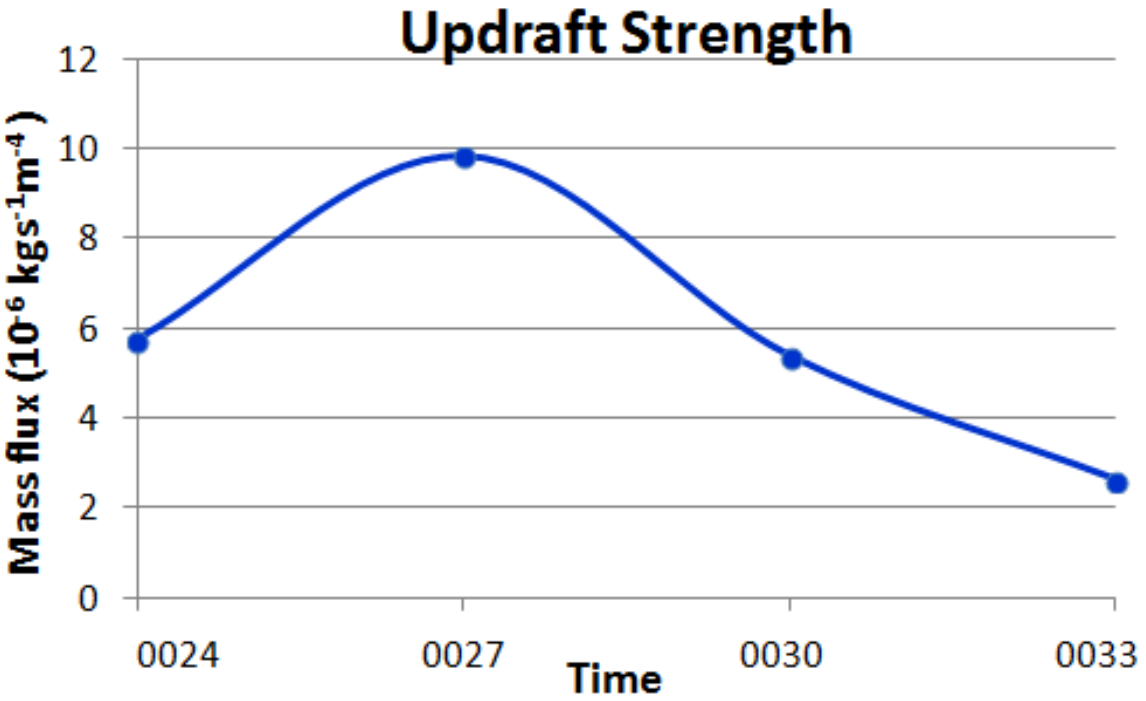

FIG. 5.6. Time evolution of updraft strength (mass flux; 10^{-6} kgs^{-1}m^{-4}) calculated using points in the updraft with w > 10 m s^{-1}.

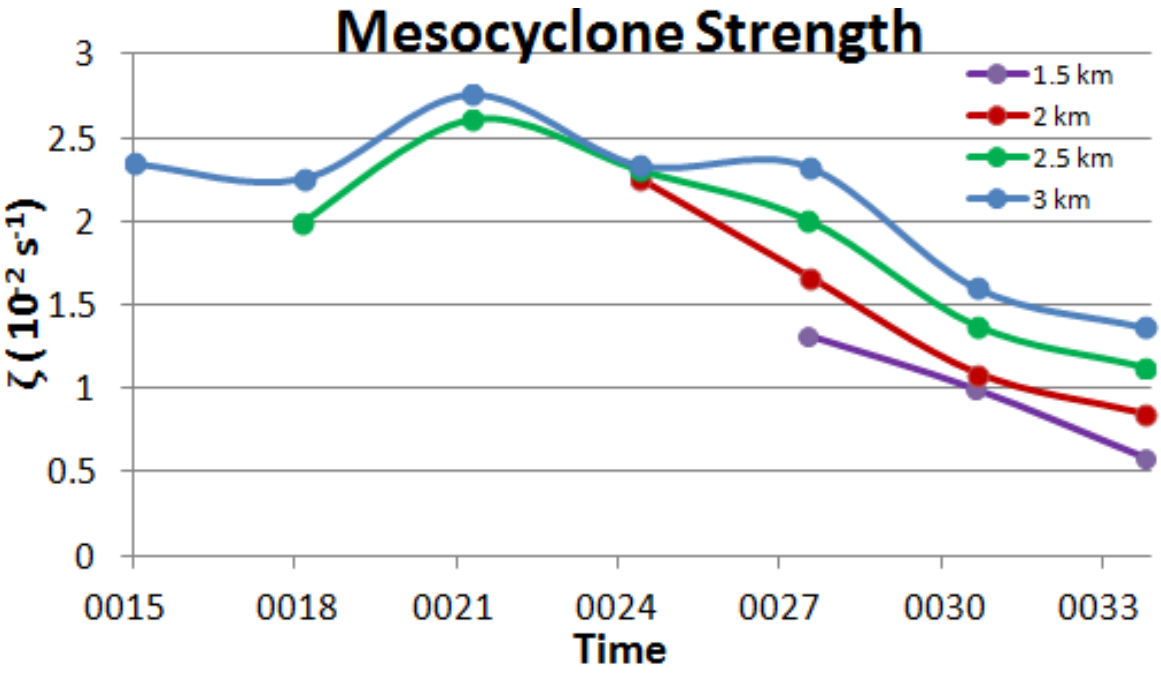

FIG. 5.7. Time evolution of dual-Doppler derived mesocyclone strength (maximum vertical vorticity; 10^{-2} s^{-1}) at various heights (color-coded).

.

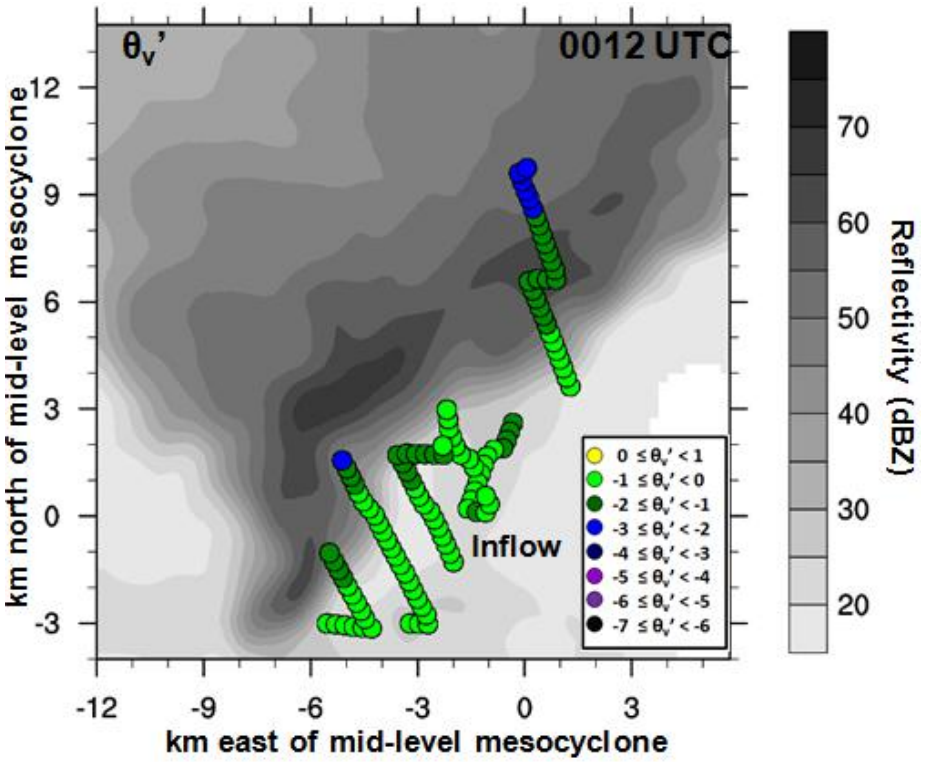

FIG. 5.8. Mobile-mesonet measured virtual potential temperature deficits (color-coded circles, relative to base state of 315.9 K) in the inflow region of the nontornadic supercell at 0012 UTC, overlayed on 750 m SR2 logarithmic equivalent reflectivity factor (dBZ, shaded contours).

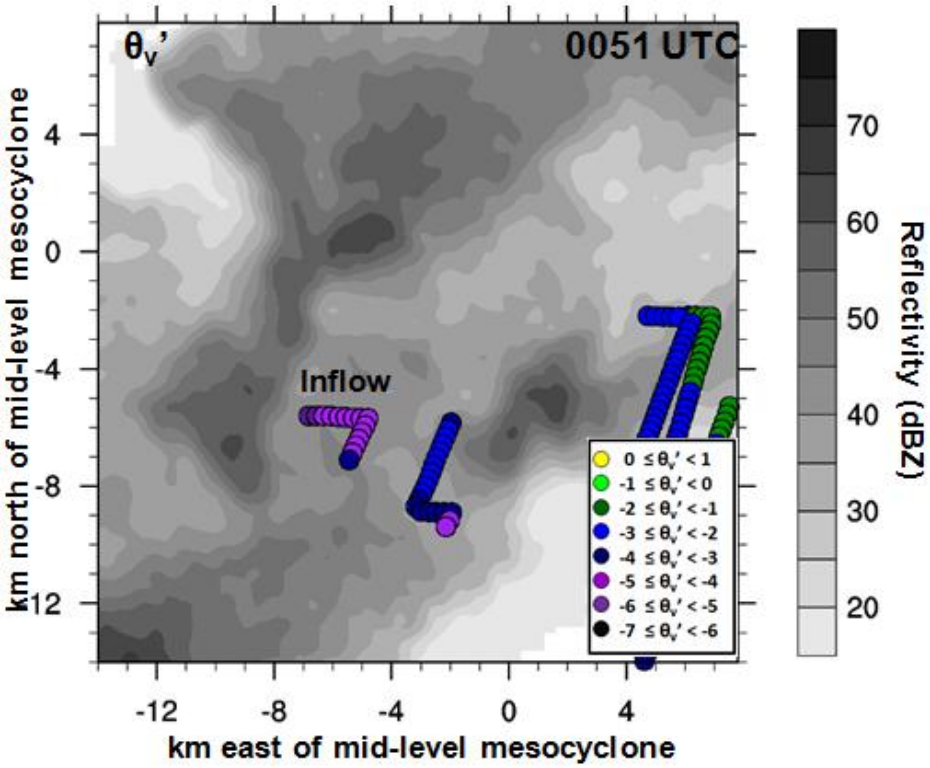

FIG. 5.9. Mobile-mesonet measured virtual potential temperature deficits (color-coded circles, relative to base state of 315.9 K) in the inflow region of the nontornadic supercell at 0051 UTC, overlayed on 1.2 km KFTG logarithmic equivalent reflectivity factor (dBZ, shaded contours).

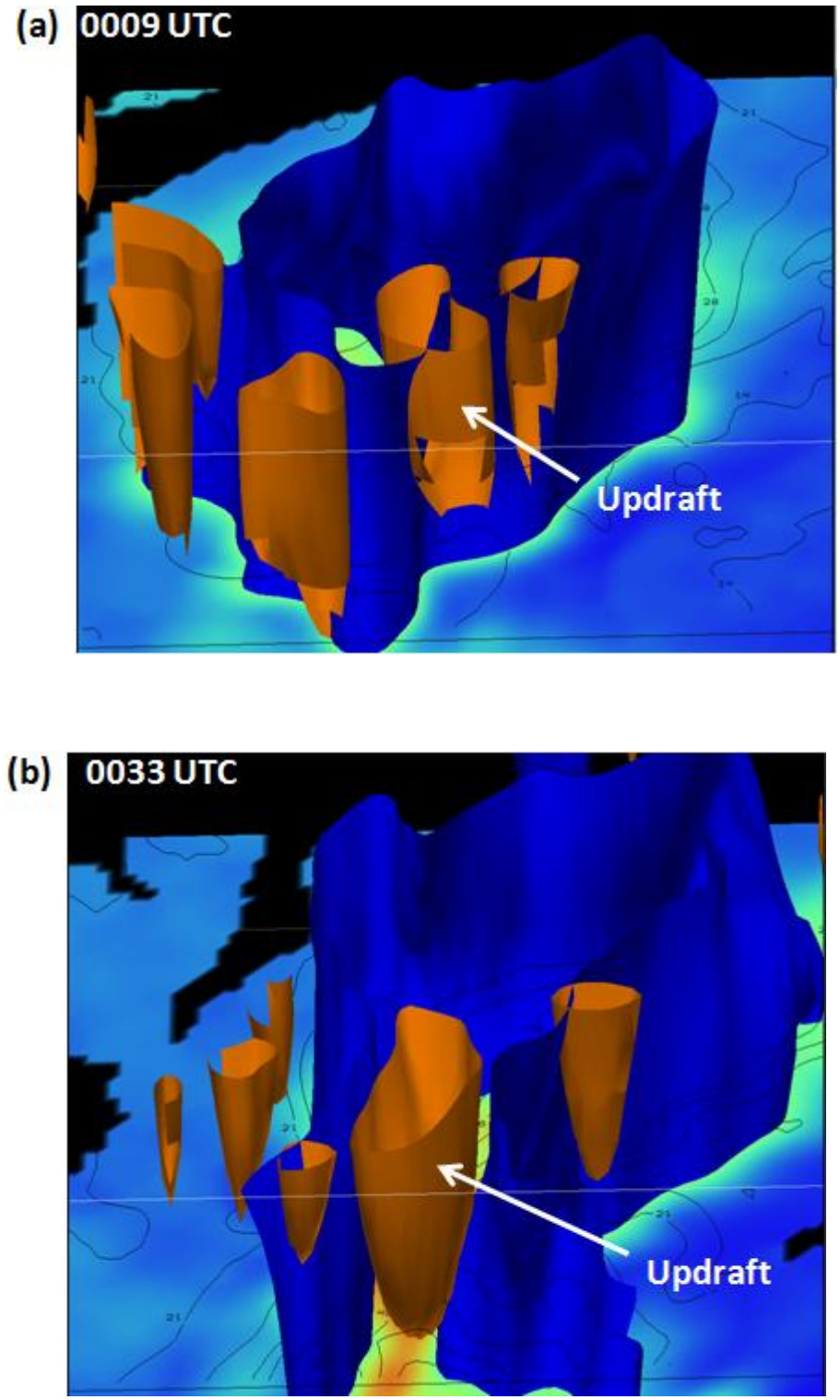

FIG. 5.10. Reflectivity isosurfaces (35 dBZ, blue) and vertical velocity isosurfaces (10 m s^{-1}, orange) overlaying 1 km SR2 logarithmic equivalent reflectivity factor (dBZ, contours and shaded) at (a) 0009 UTC (prior to any impacts of the merger) and (b) 0033 UTC (during the merger)

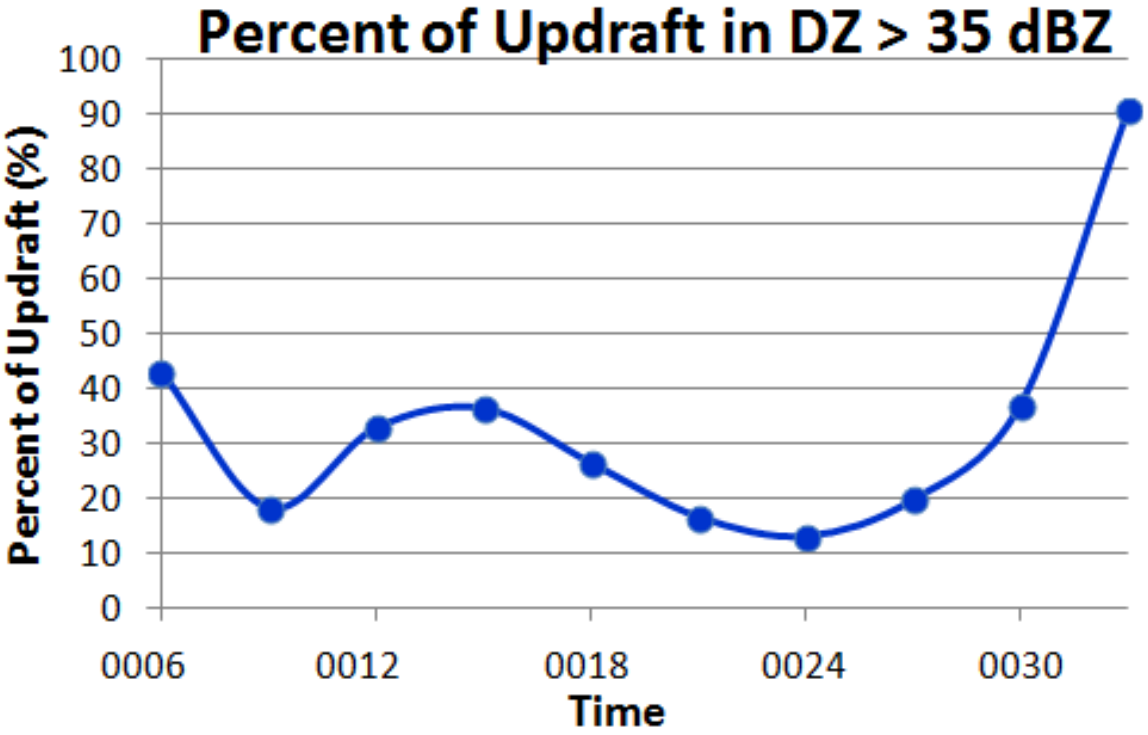

FIG. 5.11. Percent of the updraft in reflectivity of at least 35 dBZ.

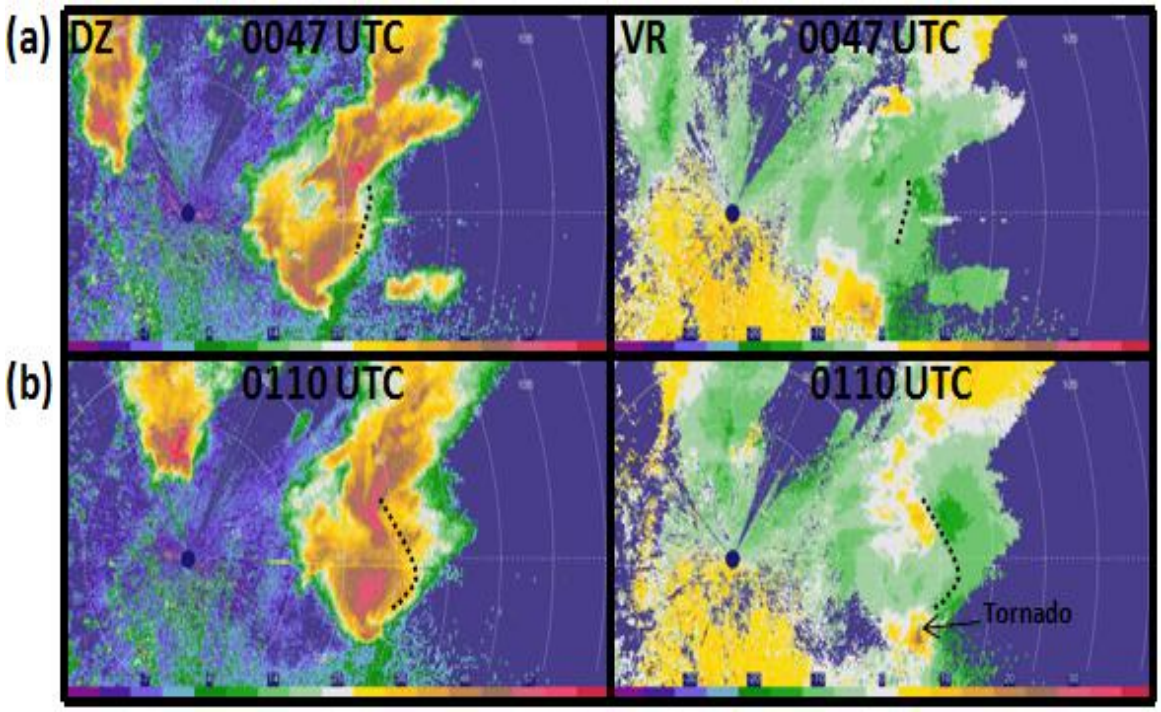

FIG. 5.12. KFTG-88D logarithmic equivalent reflectivity factor (dBZ) and radial velocity (m s^{-1}) at (a) 0047 UTC and (b) 0110 UTC. Dotted line denotes the gust front associated with the outflow of Cell A. Tornado is denoted in (b).

FIG. 5.13. Photograph of the tornadic supercell at 0154 UTC, courtesy of the LSC/NCAR Photogrammetry team (CAMB). View is looking to the north.

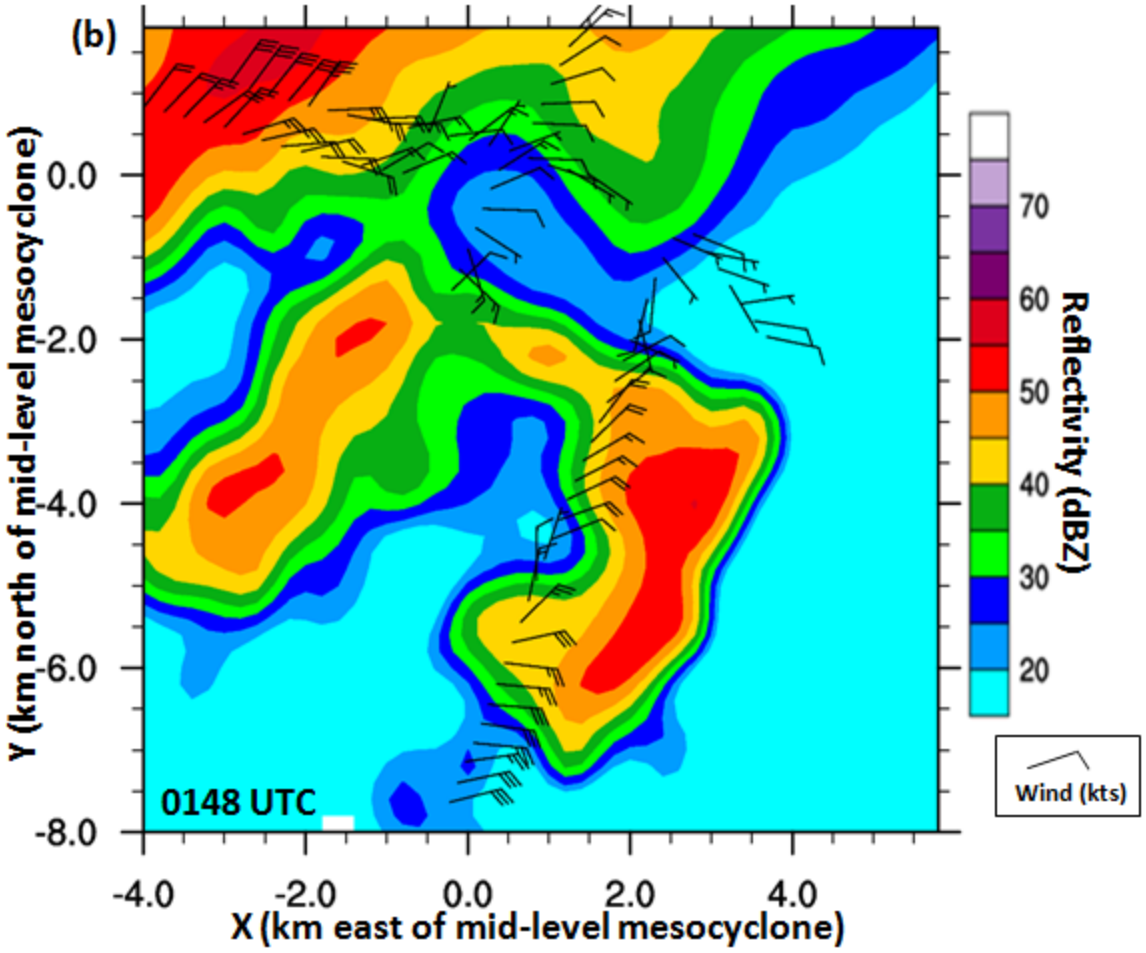

FIG. 5.14. Mobile-mesonet measured near-surface storm-relative winds (kts) in the tornadic supercell at 0148 UTC, overlayed on 800 m logarithmic equivalent reflectivity factor (dBZ, shaded contours) from NOXP.

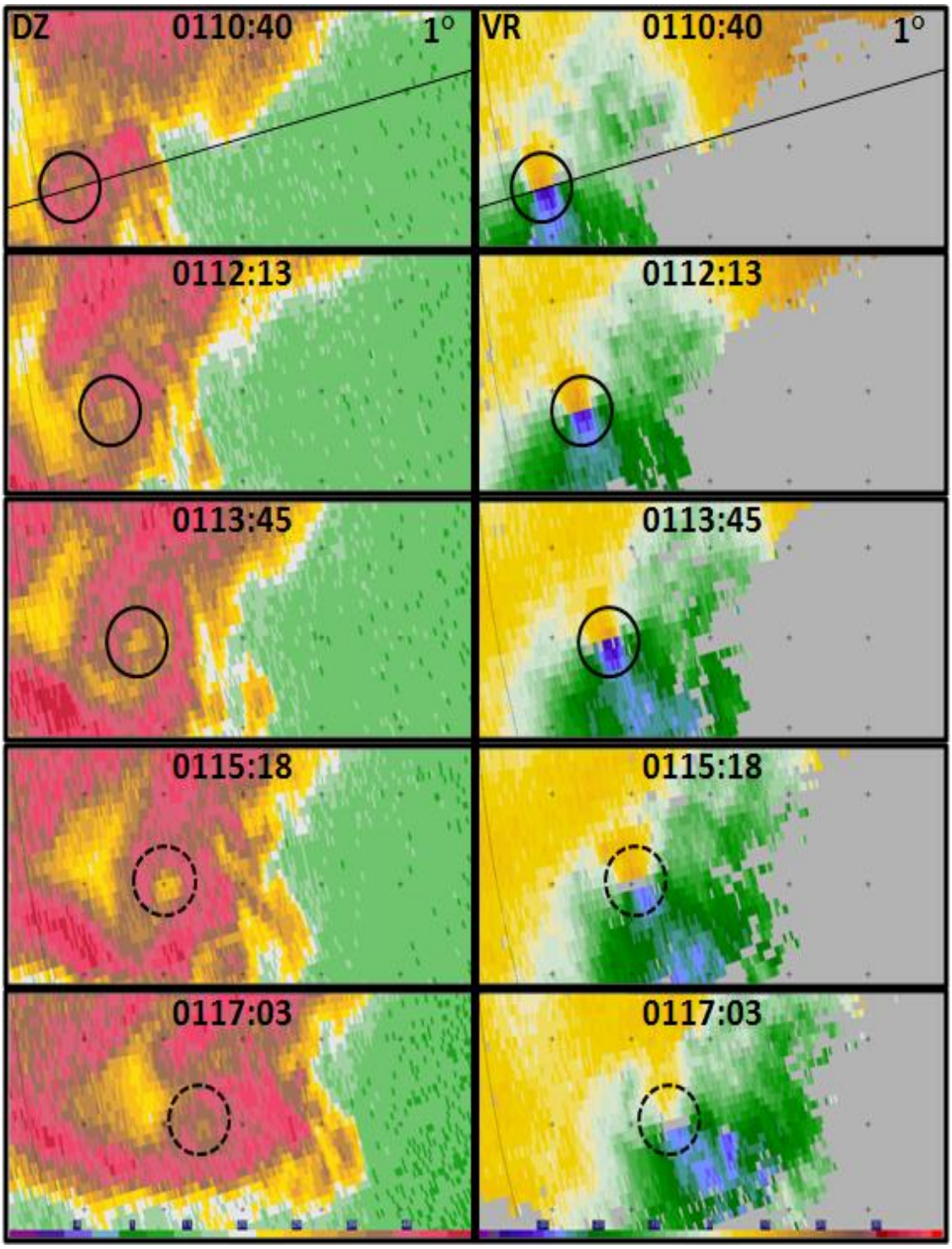

FIG. 5.15. Evolution of both tornadoes (and transition period in-between), shown by logarithmic equivalent reflectivity factor (left; dBZ) and velocity (right; m s^{-1}) data from 1° (~ 400-500 m AGL) DOW7 sweeps. Circles indicate the location of the radial velocity couplet at each time. Solid (dashed) circles are used if a tornado is present (is not present). Tick marks are spaced every 2 km. DOW7 is 30 km from the first tornado at 0110:40, and only 15 km from the second tornado at 0126:09.

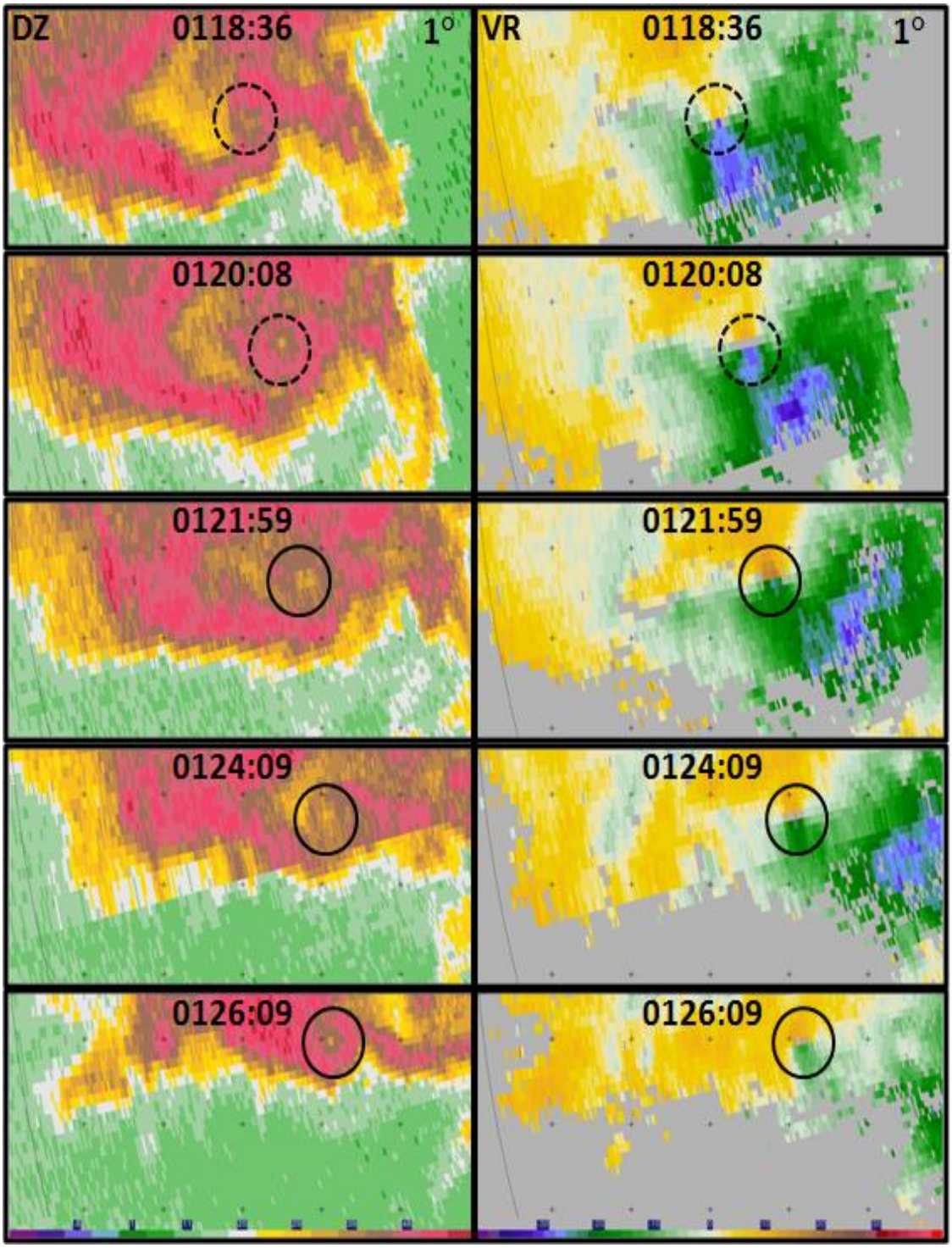

FIG. 5.15, continued.

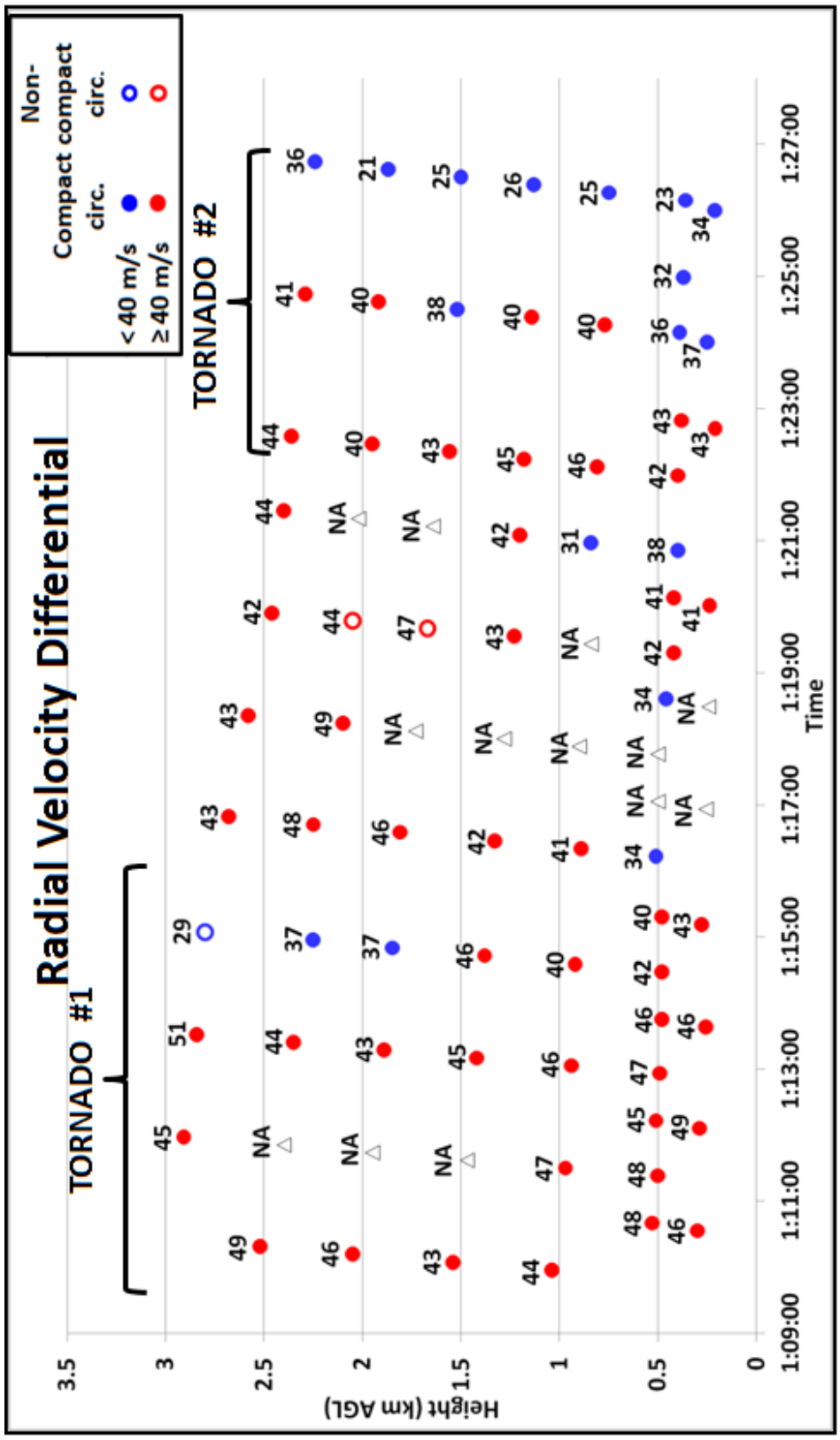

FIG. 5.16. Radial velocity differential (m s^{-1}) calculated using gate-to-gate (or one gate separation due to noise in the data) radial velocity data from the raw 0.5°, 1°, 2°, 3°, 4°, 5°, and 6° DOW7 sweeps during the first tornado (0109–0115 UTC), transition period in-between (0115–0122 UTC), and the second tornado (0122–0126 UTC). Red (blue) outlined dots indicate radial velocity differential above (below) 40 m s^{-1}. Shaded-in dots denote a circulation that is 'compact.' A triangle with NA in place of the radial velocity differential value represents noisy data that could not be analyzed.

FIG. 5.17. Photograph of the first tornado at 0114 UTC, courtesy of the LSC/NCAR Photogrammetry team (CAMA). View is looking to the southwest.

FIG. 5.18. Photograph of the dissipating first tornado at 0115 UTC, courtesy of the LSC/NCAR Photogrammetry team (CAMA). View is looking to the southwest.

FIG. 5.19. Photograph of the second tornado at 0124 UTC, courtesy of the LSC/NCAR Photogrammetry team (CAMB). View is looking to the southwest.

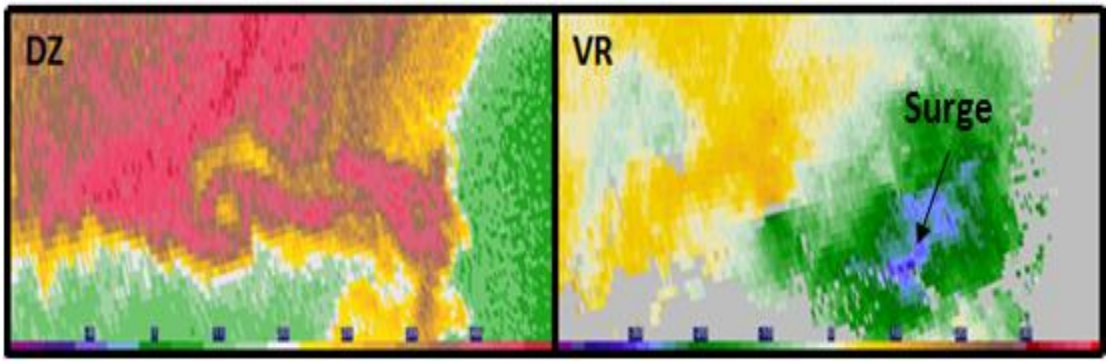

FIG. 5.20. Radar logarithmic equivalent reflectivity factor (left; dBZ) and radial velocity (right; m s^{-1}) data at 0124:59 UTC (near the end of the second tornado) from raw 1° (~ 400 m AGL) DOW7 data. The surge is labeled.

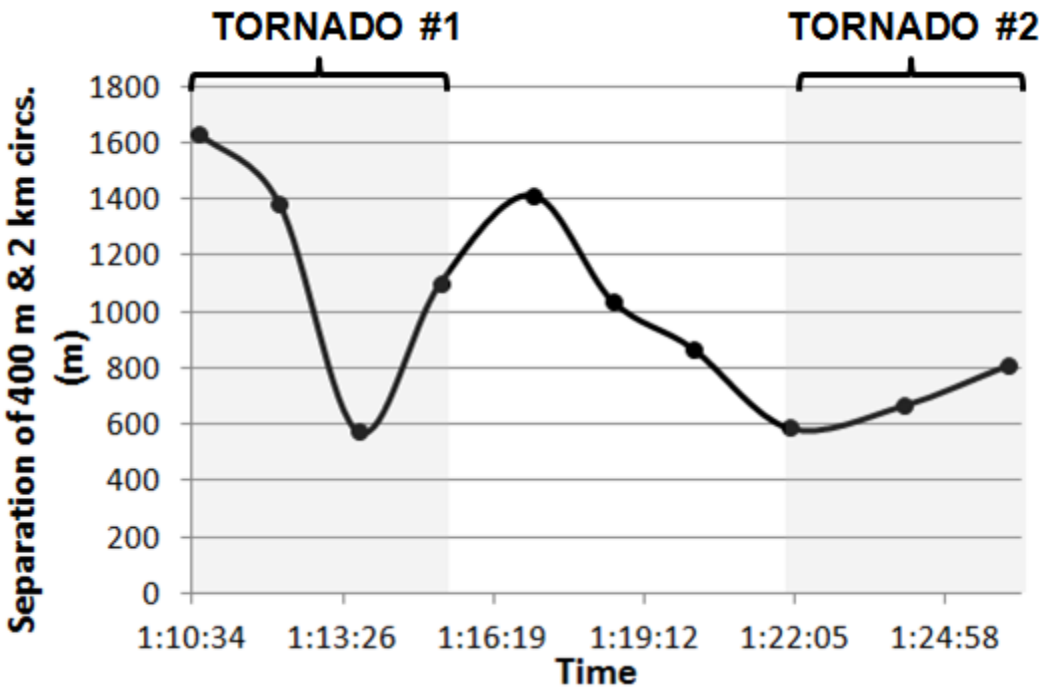

FIG. 5.21. Displacement of the 400 m circulation from the 2 km circulation (m). Displacement is calculated using the center of the 2 km circulation less the center of the 400 m circulation. All displacements imply that the 2 km circulation was to the ENE or NE of the 400 m circulation. Grey shading indicates the times a tornado was present.

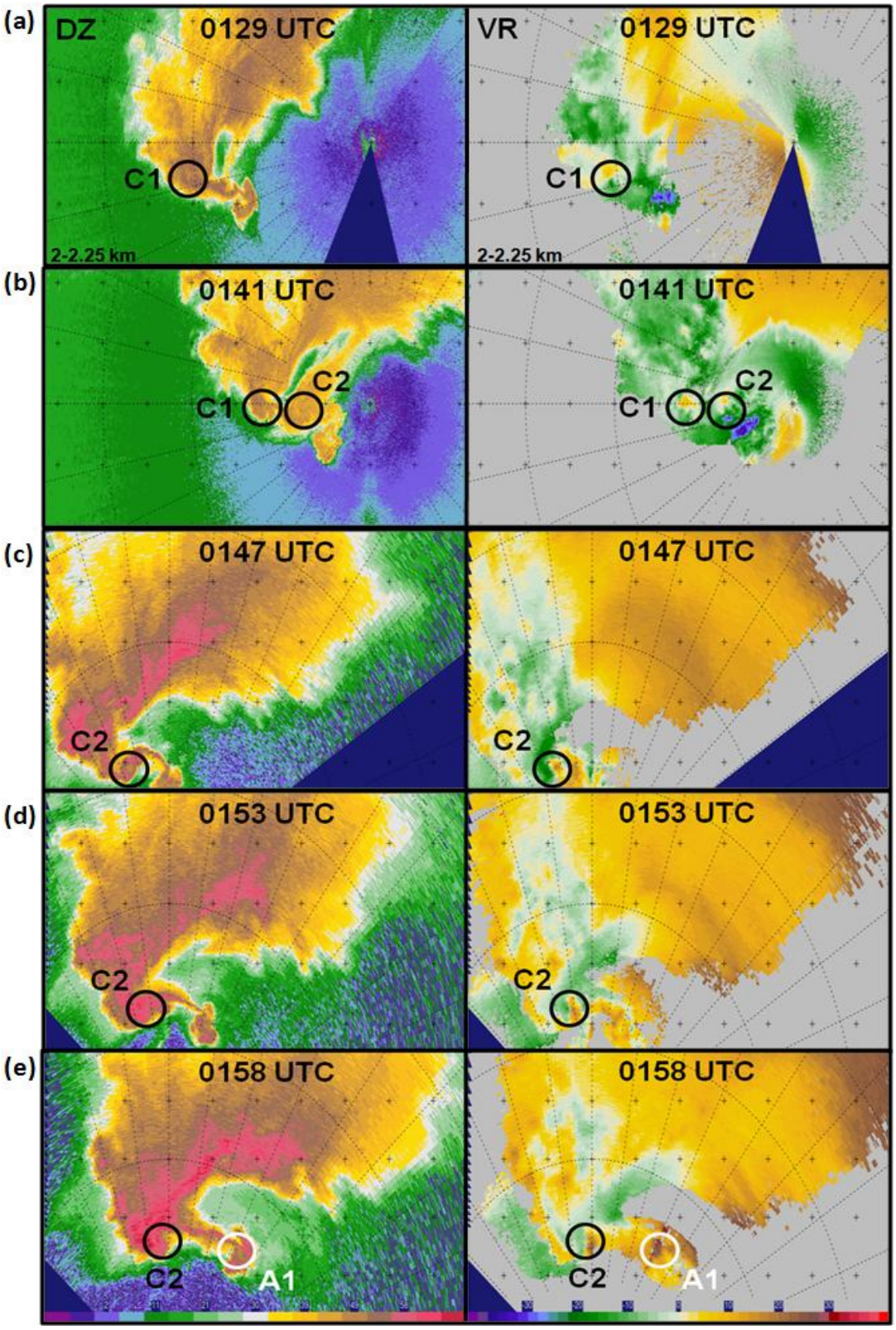

FIG. 5.22. Radar logarithmic equivalent reflectivity factor (left, dBZ) and radial velocity (right, m s^{-1}) at approximately 2-2.25 km (depending on location of particular circulation) from DOW7 [(a) and (b)] and SR2 [(c)-(j)] at the times noted (approximately every 6 minutes). Labeled black (white) circles show cyclonic (anticyclonic) circulations. The spacing of the tickmarks is 5 km. Note that DOW7 reflectivity [(a) and (b)] is uncorrected.

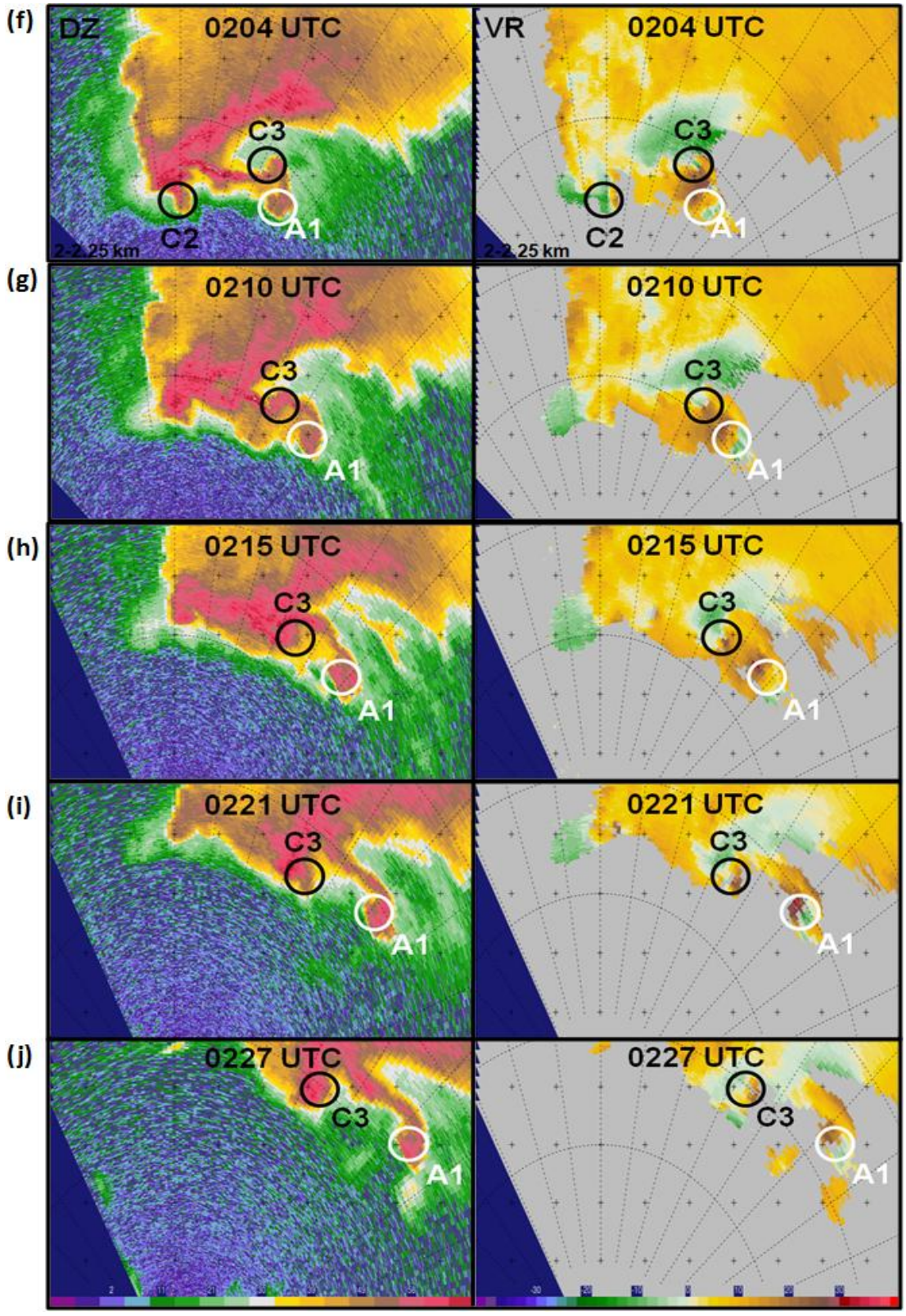

FIG. 5.22, continued.

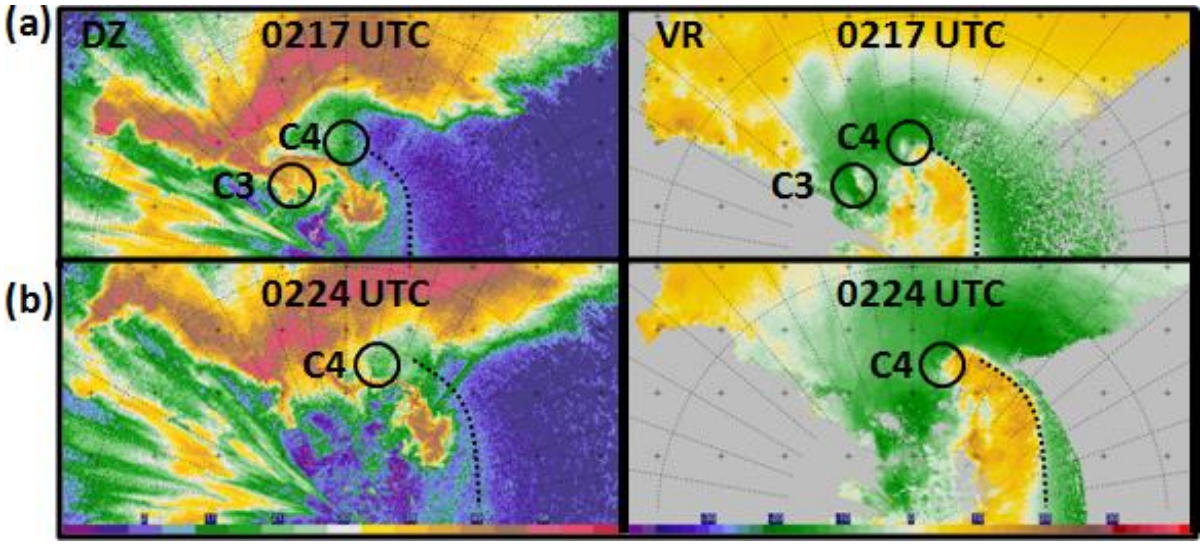

FIG. 5.23. Radar logarithmic equivalent reflectivity factor (left; dBZ) and radial velocity (right; m s^{-1}) at 1 km from NOXP at (a) 0217 UTC and (b) 0224 UTC. Labeled black circles show cyclonic circulations. Tickmarks are every 5 km. Analyzed rear-flank gust front is denoted by dashed lines.

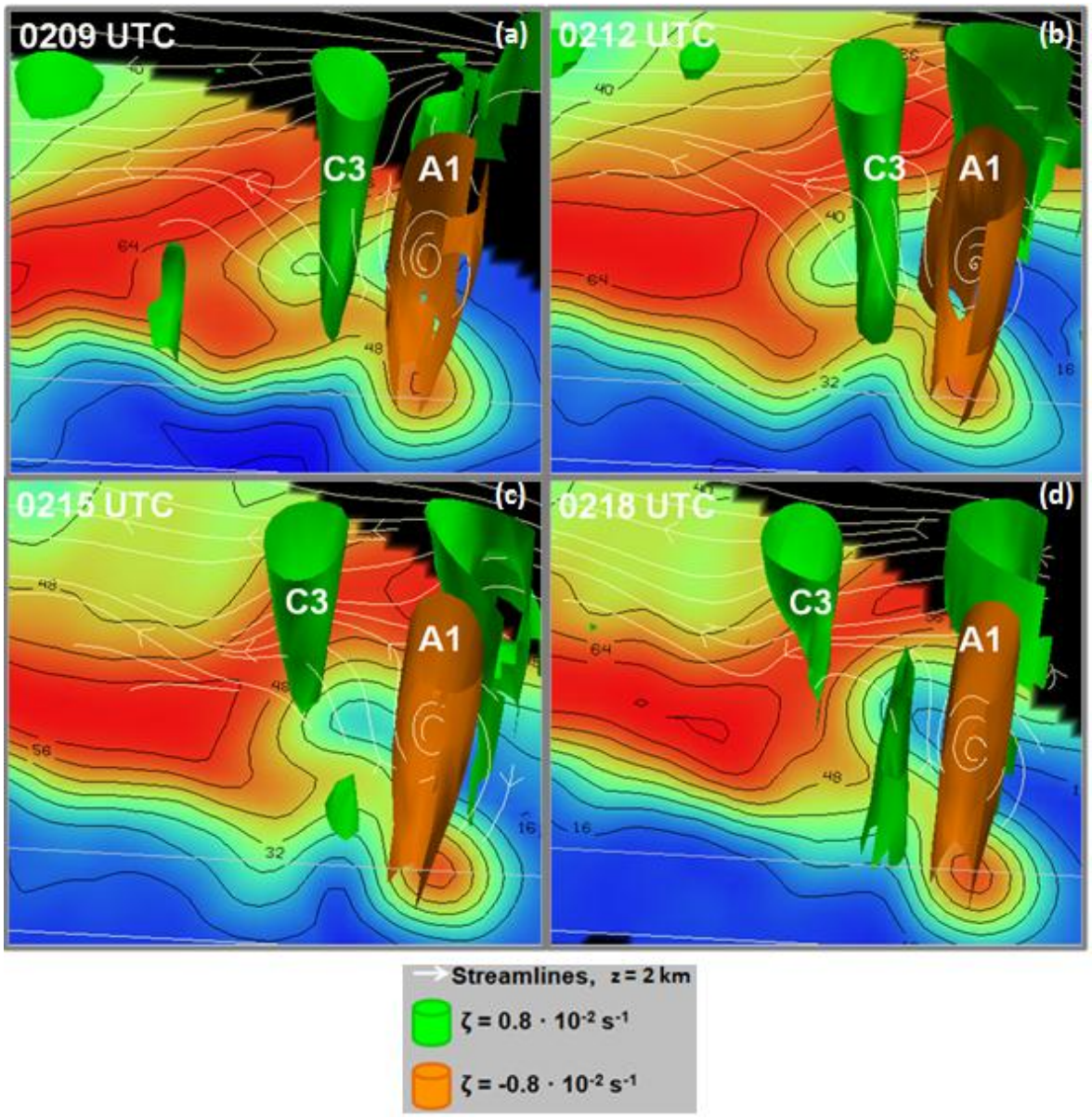

FIG. 5.24. Cyclonic vertical vorticity isosurfaces ($0.8 \cdot 10^{-2}$ s^{-1}, green) and anticyclonic vertical vorticity isosurfaces ($-0.8 \cdot 10^{-2}$ s^{-1}, orange) plotted on 500 m logarithmic equivalent reflectivity factor (dBZ, shaded and contoured) with streamlines at 2 km (white arrows) at (a) 0209 UTC, (b) 0212 UTC, (c) 0215 UTC and (d) 0218 UTC. Circulations are identified by name. View is looking approximately to the north.

Chapter 6

Discussion and conclusions

In this study, we analyzed a nontornadic and a tornadic supercell intercepted by VORTEX2 on 10 June 2010. Characteristics/processes of the storms were compared: the storm environment, outflow strength, interactions with other convective features, and storm kinematics. The goal was to identify and analyze differences in the above and use these to hypothesize why one supercell never produced a tornado and the other produced at least two. Additionally, for the tornadic supercell, the evolution of its two tornadoes and its cyclic mesocyclogenesis were examined.

Both storms developed in environments that were fairly similar and, for the most part, marginal for the development of tornadoes (especially 'significant' tornadoes), particularly in terms of shear. If low-level shear is strong, it leads to a strengthening of the low-level rotating updraft, allowing for easier stretching of near-surface vertical vorticity to tornado strength; weaker shear, on the other hand, does not promote this stretching. However, impacts of a deficiency in shear were likely not what inhibited tornadogenesis in the nontornadic supercell, given that two tornadoes were still able to develop in such an environment in the tornadic supercell. That being said, the low-level shear (measured in terms of 0–1 km storm-relative helicity) did have somewhat lower values in the environment of the nontornadic supercell; given that the environments were marginal to begin with, perhaps even a 'small' difference in shear could have had significant impacts on tornado development (or lack thereof).

Additionally, the storms had outflows with similar thermodynamic characteristics.

Both outflows, while not particularly 'cold' in terms of the typical outflows of nontornadic supercells, were cold relative to the typical outflows of (significantly) tornadic supercells. Warmer outflows are more favorable for tornadogenesis, as they allow vorticity stretching to more easily occur; colder outflows may suppress this crucial process. However, the tornadic supercell still successfully produced two tornadoes, even given the marginal (for tornadoes) thermodynamic characteristics of the outflow. This implies that the strength of the outflow likely was not what inhibited the production of weak tornadoes in the nontornadic supercell.

The supercells had differing interactions with other convective features in the region. The nontornadic supercell merged with a cell that had developed between the two supercells, near the intersection of their gust fronts. This merger led to the demise of the nontornadic supercell by weakening the updraft and mesocyclone through a combination of raining into the updraft and cooling the inflow of the supercell. Had this merger not happened, would this supercell have been able to produce a tornado? It took the tornadic supercell nearly three hours after initiation to begin producing tornadoes; the nontornadic supercell began weakening about two hours into its life. Perhaps the nontornadic supercell merely did not have the opportunity to move into a slightly more favorable environment, and/or properly develop near-surface rotation, like the tornadic supercell did.

On the other hand, this merger may have made tornadogenesis more favorable in the tornadic supercell. By twenty minutes prior to tornadogenesis, outflow from the merging cell began modifying the structure of the tornadic supercell, enhancing convergence further south into the supercell. It is difficult to surmise, however, how

significant of a role (if any) this may have played in tornadogenesis.

Aside from the aforementioned merger, the storms had different evolutions. The nontornadic supercell seemed unable to sustain strong low-level rotation, whereas the tornadic supercell had persistent low-level rotation during much of the VORTEX2 deployment. In general, the tornadic supercell was more active, with multiple observations of funnels (aside from the tornadoes) during its life and multiple cycles of mesocyclogenesis recorded. One similarity, though, is that both supercells, especially the tornadic supercell, had a persistent and strong anticyclonic vortex.

The evolution of the two tornadoes and the mesocyclogenesis later in the tornadic supercell were also analyzed. The evolution of the two tornadoes did not follow the classical model of a cycling of the mesocyclone prior to the production of a subsequent tornado; instead, the same mesocyclone produced both tornadoes. The circulation generally maintained or exceeded tornado strength at most heights during the time period between the two tornadoes and remained compact. Given the lack of a visual condensation funnel during this time period, closer to the surface the circulation must have weakened and/or become less compact.

Finally, cyclic mesocyclogenesis, the beginning of which was heralded by the demise of the second tornado, was analyzed. The circulation originally associated with the tornado continued moving rearward in the storm. Over the next hour, three new midlevel cyclonic circulations each developed in the rear-flank region and moved rearward relatively quickly aloft, due to the strong storm-relative flow in this region of the storm. The anticyclonic vortex, on the other hand, remained anchored in the hook, as it was embedded in very weak storm-relative flow.

To conclude, the storms *generally* both had outflows and environments that were marginal with respect to tornado development. However, slightly more low-level shear in the environment of the tornadic supercell may have resulted in more vorticity stretching, favoring tornadogenesis. Additionally, had the merger not occurred, the nontornadic supercell might have had the opportunity to produce a tornado, given the similarities in environment and outflow characteristics to the tornadic supercell. The merger may have made tornadogenesis more likely in the tornadic supercell than it otherwise would have been.

Future work includes doing model simulations of this case, using EnKF data assimilation techniques. Such simulations may provide insight as to what could have happened in the nontornadic supercell, had it not experienced the detrimental merger, as well as if and how the merger may have helped the tornadic supercell produce a tornado.

References

Adlerman, E.J., K.K. Droegemeier, and R. Davies-Jones, 1999: A numerical simulation of cyclic mesocyclogenesis. *J. Atmos. Sci.* **56**, 2045–2069.

Alexander, C.R. and J.M. Wurman, 2008: Updated mobile radar climatology of supercell tornado structure s and dynamics. Preprints, *24th Conf. on Severe Local Storms*, Savannah, Georgia, Amer. Meteor. Soc.

Barnes, S. L, 1964: A technique for maximizing details in numerical weather-map analysis. *J. Appl. Meteor.*, 3, 396–409.

Beck, J. and C. Weiss, 2013: An assessment of low-level baroclinity and vorticity within a simulated supercell. *Mon. Wea. Rev.*, **141**, 649–669.

Bolton, D., 1980: The computation of equivalent potential temperature. *Mon. Wea. Rev.*,**108,** 1046–1053.

Brandes, E.A., 1977: Flow in severe thunderstorms observed by dual-Doppler radar. *Mon. Wea. Rev.*, **105**, 113–120.

Brandes, E. A., 1978: Mesocyclone evolution and tornadogenesis: Some observations. *Mon. Wea. Rev.*, **106**, 995–1011.

Burgess, D. W., V. T. Wood, and R. A. Brown, 1982: Mesocyclone evolution statistics. Preprints, *12th Conf. on Severe Local Storms*, San Antonio, TX, Amer. Meteor. Soc., 422–424.

Craven, J. P., and H. E. Brooks, 2004: Baseline climatology of sounding derived parameters associated with deep, moist convection. *Nat. Wea. Digest*, **28**,13-24

Davies-Jones, R. P., D. W. Burgess, and M. Foster, 1990: Test of helicity as a tornado forecast parameter. Preprints, *16th Conf. on Severe Local Storms*, Kananaskis Park, AB, Canada, Amer.

Davies-Jones, R. P., 1984: Streamwise vorticity: The origin of updraft rotation in supercell
storms. *J. Atmos. Sci*, **41,** 2991-3006.

Davies-Jones, R.P., 2008: Can a descending rain curtain in a supercell instigate tornadogenesis barotropically?. *J. Atmos. Sci.*, **65**, 2469–2497.

Davies-Jones, R. P., and H. E. Brooks, 1993: Mesocyclogenesis from a theoretical perspective. *The Tornado: Its Structure, Dynamics, Prediction, and Hazards, Geophys. Monogr.*, Vol. 79, Amer. Geophys. Union, 105–114.

Doswell, C. A. and Burgess, D. W., 1993: Tornadoes and tornadic storms: a review of conceptual models, in the tornado: its structure, dynamics, prediction, and hazards (eds C. Church, D. Burgess, C. Doswell and R. Davies-Jones), American Geophysical Union, Washington, D. C..

Dowell, D. C., H. B. Bluestein, 2002a: The 8 June 1995 McLean, Texas, storm. Part I: Observations of cyclic tornadogenesis. *Mon. Wea. Rev.*, **130**, 2626–2648.

Dowell, D.C., H. B. Bluestein, 2002b: The 8 June 1995 McLean, Texas, Storm. Part II: Cyclic Tornado Formation, Maintenance, and Dissipation. *Mon. Wea. Rev.*, **130**, 2649–2670.

Dowell, D.C. and A. Shapiro, 2003: Stability of an iterative dual-Doppler wind synthesis in Cartesian coordinates. *J. Atmos. Oceanic Technol.*,**20**, 1552–1559.

French, M.M. et al., 2008: High-resolution, mobile Doppler radar observations of cyclic mesocyclogenesis in a supercell. *Mon. Wea. Rev.*, **136**, 4997–5016.

Hastings, R. and Y. Richardson, 2014: Long-term morphological changes in simulated supercells following mergers with nascent supercells in directionally-varying shear. Submitted to _____.

Klemp, J. B., and R. Rotunno, 1983: A study of the tornadic region within a supercell thunderstorm. *J. Atmos. Sci.*, **40**, 359–377.

Koch, S. E., M. DesJardins, and P. J. Kocin, 1983: An interactive Barnes objective map analysis scheme for use with satellite and conventional data. *J. Climate Appl. Meteor.*, **22**, 1487–1503.

Lee, B. D., C. A. Finley, and C. D. Karstens, 2012: The Bowdle, South Dakota, cyclic tornadic supercell of 22 May 2010: Surface analysis of rear-flank downdraft evolution and multiple internal surges. *Mon. Wea. Rev.*, **140**, 3419–3441.

Lee, B. D., B. F. Jewett and R. B.Wilhelmson, 2006: The 19 April 1996 Illinois tornado outbreak, part II: cell mergers and associated tornado incidence. *Weather & Forecasting*, **21**, 449-464.

Lemon, L. R. and C. A. Doswell, 1979: Severe thunderstorm evolution and mesocyclone structure as related to tornadogenesis. *Mon. Wea. Rev.*, **107**, 1184–1197.

Majcen, M., P. Markowski, Y. Richardson, D. Dowell, and J. Wurman, 2008: Multipass objective analyses of Doppler radar data. J. Atmos. Oceanic Technol., 25, 1845–1858.

Markowski, Paul M., 2002: Hook echoes and rear-flank downdrafts: a review. *Mon. Wea. Rev.*, **130**, 852–876.

Markowski, P.M. et al., 1998: Variability of storm-relative helicity during VORTEX. *Mon. Wea. Rev.*, **126**, 2959–2971.

Markowski, P.M., J.M. Straka and E.N. Rasmussen, 2003: Tornadogenesis resulting from the transport of circulation by a downdraft: idealized numerical simulations. *J. Atmos. Sci.*, **60**, 795–823.

Markowski, P.M. et al., 2008: Vortex Lines within low-level mesocyclones obtained from pseudo-dual-Doppler radar observations. *Mon. Wea. Rev.*, **136**, 3513–3535.

Markowski, P.M. et al., 2011: Characteristics of the wind field in three nontornadic low-level mesocyclones observed by the Doppler on Wheels radars. *Electron. J. Severe Storms Meteor.*, **6,** 1–48.

Markowski, P.M. et al., 2012: The pretornadic phase of the Goshen County, Wyoming, supercell of 5 June 2009 intercepted by VORTEX2. Part I: Evolution of kinematic and surface thermodynamic fields. *Mon. Wea. Rev.*, **140**, 2887–2915.

Markowski, P.M. and Y.P. Richardson, 2009: Tornadogenesis: our current understanding, forecasting considerations, and questions to guide future research. *J. Atmos. Res.*, **93**, 3-10.

Markowski, P.M. and Y.P. Richardson, 2010: *Mesoscale meteorology in midlatitudes*. Wiley-Blackwell, 407 pp.

Markowski, P.M. and Y.P. Richardson, 2014: The influence of environmental low-level shear and cold pools on tornadogenesis: insights from idealized simulations. J. Atmos. Sci., **71**, 243-275.

Markowski, P. M., J. M. Straka, and E. N. Rasmussen, 2002: Direct surface thermodynamic observations within the rear-flank downdrafts of nontornadic and tornadic supercells. *Mon. Wea. Rev.*, **130**, 1692–1721.

Marquis, J., Y. Richardson, P. Markowski, D. Dowell, and J. Wurman, 2012: Tornado maintenance investigated with high-resolution Dual-Doppler and EnKF analysis. *Mon. Wea. Rev.*, **140**, 3-27.

National Center for Atmospheric Research, 2010: Documentation: Second Verification of the Origins of Rotation in Tornadoes Experiment (VORTEX2) 2009 quality controlled radiosonde data set**.** http://data.eol.ucar.edu/codiac/dss/id=114.111

National Oceanic and Atmospheric Administration, 2011: http://www.noaanews.noaa.gov/2011_tornado_information.html

Oye, R., C. Mueller, and S. Smith, 1995: Software for radar translation, visualization, editing, and interpolation. 27th Conf. on Radar Meteorology, Vail, CO, American Meteorological Society, 359 -361.

Pauley, P. M., and X. Wu, 1990: The theoretical, discrete, and actual response of the Barnes objective analysis scheme for one- and two- dimensional fields. *Mon. Wea. Rev.*, **118**, 1145-1164.

Rasmussen, E.N., and D.O. Blanchard, 1998: A baseline climatology of sounding-derived supercell and tornado forecast parameters. *Wea. Forecasting*, **13**, 1148-1164.

Rasmussen, E. N., 2003: Refined supercell and tornado forecast parameters. *Wea. Forecasting,* **18**, 530–535.

Rogers, J.W., 2012: Significant tornado events with cell mergers. Preprints, *26th Conf. on Severe Local Storms*, Nashville, TN, Amer. Meteor. Soc.

Rotunno, R., 1981: On the evolution of thunderstorm rotation. *Mon. Wea. Rev*., **109**, 577–586

Rotunno, R., and J. B. Klemp, 1985: On the rotation and propagation of simulated supercell thunderstorms. *J. Atmos. Sci*., **42**, 291–292.

Shabbott, C. J., and P. M. Markowski, 2006: Surface in situ observations within the outflow of forward-flank downdrafts of supercell thunderstorms. *Mon. Wea. Rev.*, **134**, 1422–1441

Straka, J. M., E. N. Rasmussen, R. P. Davies-Jones, and P. M. Markowski, 2007: An observational and idealized numerical examination of low-level counter-rotating vortices toward the rear flank of supercells. *Electron. J. Severe Storms Meteor.*, **2,** 1–22.

Straka, J. M., E. N. Rasmussen, and S. E. Fredrickson, 1996: A mobile mesonet for fine-scale meteorological observations. *J. Atmos. Oceanic Technol.*, **13**, 921–936.

Thompson, R. L. et al., 2012: Convective modes for significant severe thunderstorms in the contiguous United States. Part II: Supercell and QLCS tornado environments. Wea. Forecasting, **27**, 1136-1154.

Thompson, R., R. Edwards, and J.A. Hart, 2002: Evaluation and interpretation of the supercell composite and significant tornado parameters at the Storm Prediction Center. Preprints, *21st Conf. on Severe Local Storms,* San Antonio, TX, Amer. Meteor. Soc., J11–J14.

Thompson, R. L., R. Edwards, J. A. Hart, K. L. Elmore, and P. Markowski, 2003: Close proximity soundings within supercell environments obtained from the Rapid Update Cycle. *Wea. Forecasting*, **18**, 1243-1261.

Trapp, R.J. and C.A. Doswell, 2000: Radar data objective analysis. *J. Atmos. Oceanic Technol.*, **17**, 105–120.

Trapp, R. J., G. J. Stumpf, and K. L. Manross, 2005: A reassessment of the percentage of tornadic mesocyclones. *Wea. Forecasting*, **20**, 680–687.

Waugh, S., and S. E. Fredrickson, 2010: An improved aspirated temperature system for mobile meteorological observations, especially in severe weather. Preprints, 25th Conf. on Severe Local Storms, Denver, CO, Amer. Meteor. Soc., P5.2. [Available online at http://ams.confex.com/ams/25SLS/techprogram/paper_176205.htm.]

Weiss, C. C., and J. L. Schroeder, 2008: StickNet: A new portable, rapidly deployable surface observation system. *Bull. Amer. Meteor. Soc.*, **89**, 1502–1503.

Wicker, L. J., R.B. Wilhelmson, 1995: Simulation and analysis of tornado development and decay within a three-dimensional supercell thunderstorm. *J. Atmos. Sci*., **52**, 2675–2703.

Wurman, J., D. et al., 2012: The Second Verification of the Origins of Rotation in Tornadoes Experiment: VORTEX2. *Bull. Amer. Meteor. Soc.*, **93**, 1147–1170.

Wurman, J., Y. Richardson, C. Alexander, S. Weygandt, and P. F. Zhang, 2007: Dual-Doppler and single-Doppler analysis of a tornadic storm undergoing mergers and repeated tornadogenesis. *Mon. Wea. Rev.,* **133,** 97-119.

Xue, M., 2004. Tornadogenesis within a simulated supercell storm. Preprints, *22nd Conf. on Severe Local Storms*. Amer. Meteor. Soc., Hyannis, MA